Mayer, L., Pisias, N., Janecek, T., et al., 1992
Proceedings of the Ocean Drilling Program, Initial Reports, Vol. 138

12. SITE 847[1]

Shipboard Scientific Party[2]

HOLE 847A

Date occupied: 27 May 1991

Date departed: 28 May 1991

Time on hole: 8 hr, 29 min

Position: 0° 11.593′N, 95° 19.227′W

Bottom felt (rig floor; m, drill-pipe measurement): 3346.0

Distance between rig floor and sea level (m): 11.7

Water depth (drill-pipe measurement from sea level, m): 3334.3

Total depth (rig floor; m): 3355.5

Penetration (m): 9.5

Number of cores (including cores with no recovery): 1

Total length of cored section (m): 9.5

Total core recovered (m): 9.52

Core recovery (%): 100.2

Oldest sediment cored:
Depth (mbsf): 9.5
Nature: nannofossil ooze with foraminifers
Earliest age: Pleistocene

HOLE 847B

Date occupied: 28 May 1991

Date departed: 29 May 1991

Time on hole: 1 day, 17 hr, 40 min

Position: 0° 11.593′N, 95° 19.227′W

Bottom felt (rig floor; m, drill-pipe measurement): 3346.0

Distance between rig floor and sea level (m): 11.7

Water depth (drill-pipe measurement from sea level, m): 3334.3

Total depth (rig floor; m): 3593.0

Penetration (m): 247.0

Number of cores (including cores with no recovery): 27

Total length of cored section (m): 247.0

Total core recovered (m): 242.19

Core recovery (%): 98.1

Oldest sediment cored:
Depth (mbsf): 231.9
Nature: diatom nannofossil ooze
Earliest age: late Miocene

Hard rock:
Depth (mbsf): 247.0
Nature: chert

[1] Mayer, L., Pisias, N., Janecek, T., et al., 1992. *Proc. ODP, Init. Repts.,* 138: College Station, TX (Ocean Drilling Program).

[2] Shipboard Scientific Party is as given in list of participants preceding the contents.

HOLE 847C

Date occupied: 29 May 1991

Date departed: 30 May 1991

Time on hole: 21 hr, 10 min

Position: 0° 11.585′N, 95° 19.189′W

Bottom felt (rig floor; m, drill-pipe measurement): 3346.0

Distance between rig floor and sea level (m): 11.7

Water depth (drill-pipe measurement from sea level, m): 3334.3

Total depth (rig floor; m): 3578.3

Penetration (m): 232.3

Number of cores (including cores with no recovery): 25

Total length of cored section (m): 230.3

Total core recovered (m): 225.71

Core recovery (%): 98.0

Oldest sediment cored:
Depth (mbsf): 231.19
Nature: diatom nannofossil ooze
Earliest age: late Miocene

Hard rock:
Depth (mbsf): 232.0
Nature: chert

HOLE 847D

Date occupied: 30 May 1991

Date departed: 31 May 1991

Time on hole: 18 hr, 40 min

Position: 0° 11.577′N, 95° 19.195′W

Bottom felt (rig floor; m, drill-pipe measurement): 3346.9

Distance between rig floor and sea level (m): 11.7

Water depth (drill-pipe measurement from sea level, m): 3335.2

Total depth (rig floor; m): 3477.0

Penetration (m): 130.1

Number of core (including cores with no recovery): 14

Total length of cored section (m): 130.1

Total core recovered (m): 133.57

Core recovery (%): 102.7

Oldest sediment cored:
Depth (mbsf): 130.1
Nature: nannofossil ooze
Earliest age: early Pliocene

Principal results: Site 847 (proposed Site EEQ-3) is the equatorial divergence site of the Leg 138 eastern transect. The site, located 20 km from the equator and approximately 380 km west of the Galapagos Islands, was selected to provide a detailed record of equatorial divergence near the eastern boundary of the Pacific in a region where the equatorial undercur-

rent surfaces and interacts with surface waters. The backtrack path for this site indicates that this site has remained within the equatorial divergence zone for its entire history.

Four holes were drilled at the site. Hole 847A was a single APC mud-line core dedicated to whole-round geochemical and physical property measurements. Hole 847B was APC-cored to 139 mbsf, where excessive overpull made necessary the switch to the XCB-coring system. Hole 947B was continued with the XCB to 251 mbsf, where penetration of the XCB was stopped and small amounts of chert recovered. The silica yields on geochemical logs suggest that a layer containing significant chert was at least 4 m thick. Hole 847B was terminated at this layer, and Hole 847C was drilled with the APC to 124 mbsf and then continued with the XCB to 232 m. The overlapping XCB section demonstrates the high quality of recovery by the XCB in the pelagic sediments of this region; the cored section will allow for continued study of high-resolution paleoceanographic and paleoclimatic processes well into the Miocene. A fourth hole was drilled to 130 mbsf with the APC system to ensure further that a continuous APC section was recovered and to provide the volume of material necessary for high-resolution paleoceanographic studies.

The sedimentary sequence can be described by one lithologic unit dominated by nannofossil ooze and diatom nannofossil ooze and representing continuous sediment accumulation during the last 6.8 million years. There are two intervals (1.5–1.9 Ma and 4.3–4.6 Ma) when the section is dominated by diatom ooze. Sedimentation rates average about 30 m/m.y. with a maximum rate of over 50 m/m.y during the early Pliocene.

The paleomagnetic signal at Site 847 was very weak, and it was impossible to reliably determine direction. However, biostratigraphic age control was provided by all four of the chief planktonic microfossil groups, though their abundances and state of preservation were quite variable throughout. Radiolarians and diatoms are abundant from the upper Miocene to the Pleistocene. Calcareous nannofossils are generally abundant and well-preserved in the Pliocene and Pleistocene while planktonic foraminifers are common in the Pleistocene, but their abundance and preservation deteriorates downsection.

The high-resolution GRAPE and sediment color reflectance records obtained from the overlapping APC section, combined with initial biostratigraphy, show that Milankovitch orbital frequencies are contained in these sedimentary properties. Initial analysis suggests that it may be possible to orbitally tune these records to at least 5 Ma and thus provide a very high-resolution chronostratigraphic framework for paleoceanographic studies.

Early Miocene nannofossils (approximately 22 Ma) were found in the lower part of the section as well as associated with the recovered chert. The age of this material presents a fundamental dilemma regarding the tectonics of this region. Reconstructions of the region suggest crustal ages of less than 9 Ma and thus would preclude a source for 22-m.y.-old sediments.

Interstitial-water chemistry shows the influence of diagenetic processes and possibly upward fluid advection. Profiles of alkalinity, ammonia, and sulfate indicate modification by advection as do the convex-upward profiles of sodium and chloride. This evidence for fluid advection as well as the relatively high temperature gradients recorded at this site (approximately 0.07° C/m) provide an explanation for the presence of chert at relatively shallow depth.

While the "Leadville" slump continued for paleomagnetics, the complete recovery, well-defined biostratigraphy, multiple, continuous high-resolution laboratory records (GRAPE, *P*-wave velocity, susceptibility, and color) and an excellent suite of logs show that the platinum vein of high-resolution paleoclimate and paleoceanographic studies first discovered at Site 846 continues to Site 847. With the completion of Site 847 Leg 138 completed 8.6 log(m^2kt).

BACKGROUND AND SCIENTIFIC OBJECTIVES

Site 847 is located west of the Galapagos Islands in the region of interaction between the shoaling, eastward-flowing, Equatorial Undercurrent and the westward-flowing surface South Equatorial Current (Fig. 1). This site is the fourth site in the eastern transect of Leg 138 and provides a late Neogene record of paleoceanographic change within the equatorial divergence zone.

The crust at Site 847 lies near an area thought to be the transition between crust generated at the east-trending Galapagos Spreading Center and crust generated at the north-trending East Pacific Rise (Fig. 2). Seismic and Seabeam bathymetric data collected on the site survey cruise (see "Site Surveys" chapter, this volume) reveal that the topography at the site trends northeast (Fig. 3). Both the northwest and southeast quadrants of the survey area are characterized by relatively rough basement overlain by undulating surface topography and a complex seismic reflector pattern. In the center of the survey area is a northeast-southwest trending trough-like feature that is underlain by relatively smooth basement and is filled with flat-lying sediments. The seafloor in the areas of rough basement is 20–50 m shallower than that above the smooth basement. The sediment thickness over smooth basement is, however, slightly greater than that over the areas of rough basement (0.45 s over smooth basement, 0.43–0.44 s over rough basement). The site is located within a region of flat-lying seismic (Fig. 4) basement.

Basement age at Site 847 was originally estimated to be about 8 m.y. old based on tectonic reconstructions of Hey (1977) and Hey et al. (1977). However, the significant age differences between expected and observed basement ages found at previous Leg 138 sites suggested that further testing of tectonic reconstructions of the eastern equatorial Pacific would be of interest. Thus, in addition to the paleoceanographic objectives of Site 847, a tectonic objective was to provide improved estimates of basement ages in this complex tectonic regime.

OPERATIONS

Transit to Site 847

The transit from Site 846 to Site 847 (proposed Site EEQ-3) covered 322 nmi in 32.3 hr (local time, L; all times in operations text is L, or Universal Time Coordinated, UTC minus 6 hr. All times in Table 1 are in UTC.) at an average speed of 10.0 kt. At 1400L 27 May, the vessel reached the first survey way point, and the seismic gear was deployed as the ship slowed to 6 kt to begin the survey. After a 21-nmi survey, a beacon was deployed at 1630L 27 May, at the proposed site location. The seismic gear was then retrieved as the ship returned to the site and, once on site, the hydrophones and thrusters were deployed. The depth to the seafloor, based upon the precision depth recorder (PDR), was 3354.4 mbrf.

Hole 847A

This hole consisted of a single mud-line core dedicated to whole-round geochemical and physical property measurements. The drill string was lowered to 3348 mbrf, where the first piston core (138-847A-1H) was retrieved at 0100L 28 May (Table 1). A full core barrel was retrieved (9.52 m) and thus could not be used to establish the mud-line depth.

Hole 847B

The second mud-line core (138-847B-1H) was taken at 3343 mbrf and from it we recovered 6.59 m of sediment, establishing the mud-line depth at 3346 m. Cores 138-847-1H through -14H (0–130.0 mbsf) were retrieved in rapid succession, with orientation beginning on Core 138-847-4H. The core barrel became stuck after Core 138-847B-15H was on deck and could not be retrieved, even with an overpull of 80,000 lb. The core barrel was then drilled over approximately 3 m, at which point the core barrel came free without any overpull. The APC-coring program in this hole was terminated after Core 138-847C-15H. The average recovery for the APC-cored interval was 104.3%.

Coring resumed with the XCB-coring system and Cores 138-847B-16X through -25X were taken over the interval from 139.5 to

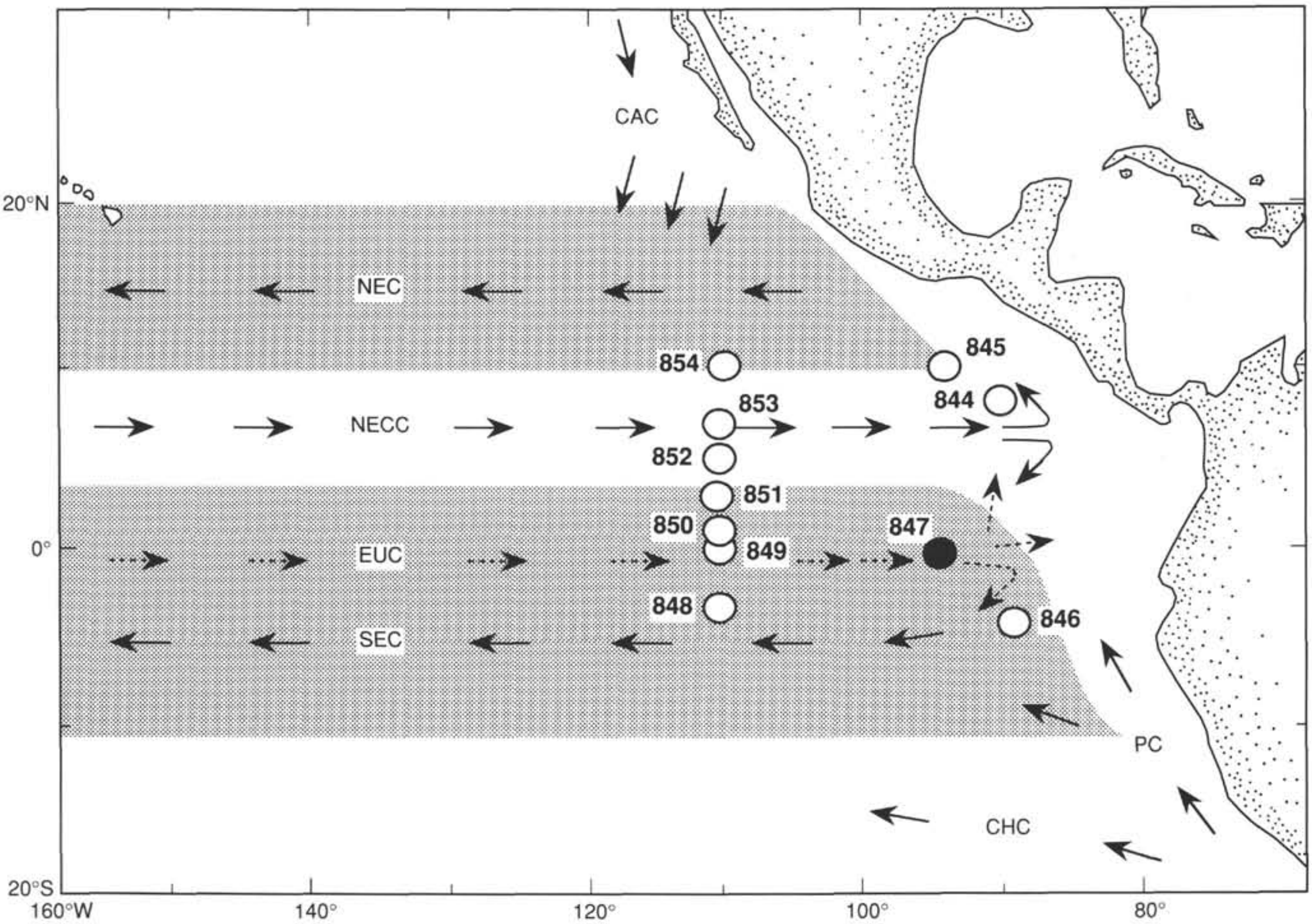

Figure 1. Location of Site 847 and other Leg 138 sites and generalized circulation system of the eastern equatorial Pacific. Surface current shown as solid arrows, subsurface current as dashed arrows: CAC = California Current; NEC = North Equatorial Current; NECC = North Equatorial Countercurrent; EUC = Equatorial Undercurrent; SEC = South Equatorial Current; PC = Peru Current; and CHC = Chile Current. Shaded area illustrates general latitudinal extent of the SEC and NEC.

231.9 mbsf. While cutting Core 138-847B-26X (231.9–241.5 mbsf), the rate of penetration decreased sharply and the core barrel was retrieved with only 0.14 m of chert fragments. The soft formation cutting shoe was completely destroyed and was replaced with the tungsten-enhanced cutting shoe that was used with success to cut basalt at the previous three sites. After 60 min of coring and only 5.5 m of penetration, the next core (847B-27X, 241.5–247.0 mbsf) recovered only 0.04 m of chert fragments. The cutting shoe was missing three inserts and the cutting structure was completely worn down.

A review of the seismic records indicated that the chert layer could be over 40 m thick. The time required for pulling the pipe, switching to the RCB coring system and drilling to basement was not warranted, so drilling was stopped and preparations for logging begun. Recovery in the XCB portion of the hole was 89.9%.

Logging—Hole 847B

After sweeping the hole with mud, the pipe was pulled back to the logging depth of 65.7 mbsf and the three standard ODP tool strings (geophysical, geochemical, and FMS) were run. A summary of the operations can be found in Table 2. All logging runs, except the downward pass of the geophysical tool string were done with the heave compensator on.

The downward pass with the geophysical string logged the section to total depth (246.3 mbsf). On the first upward logging pass, the resistivity log was recalibrated while the tool was in motion. Thus, good data were collected only from 201.2 mbsf (the depth at which the calibrations were completed) to 128.3 mbsf. The second geophysical logging run collected data over the interval from 246.0 to 73.8 mbsf, at which point the run was stopped, the heave compensator turned off, and the tool string brought into the drill pipe.

The geochemical string was lowered to total depth (247.2 mbsf), the heave compensator turned on and the GST calibrated while the tool was pulled up the hole (to avoid activating the section). Once the GST was calibrated, the tool was lowered to total depth (248.4 mbsf), and the hole was logged up to 67.7 mbsf, at which point the heave compensator was turned off and the tool string pulled into the pipe. Once in the pipe, geochemical logging continued up to the mud line. The logging run was stopped for a short interval at about 155 mbsf when the winch was switched to the backup motor. Thus, there may be activated sections of borehole near this depth interval and unreliable recordings on the ACT or natural gamma-ray logs.

Some difficulties were encountered during the FMS logging, but one good pass was recorded from total depth (247.2 mbsf) to the base of pipe. During the first upward pass the circuit used to close the calipers developed an intermittent short. The calipers did close upon reaching the pipe but the process took much longer than normal. The second FMS run was cancelled instead of risking a second pass in which the calipers might not close.

At the conclusion of the logging program, the drill string was pulled out of the hole, and the bit cleared the mud line at 1840 hr, 29 May, ending Hole 847B.

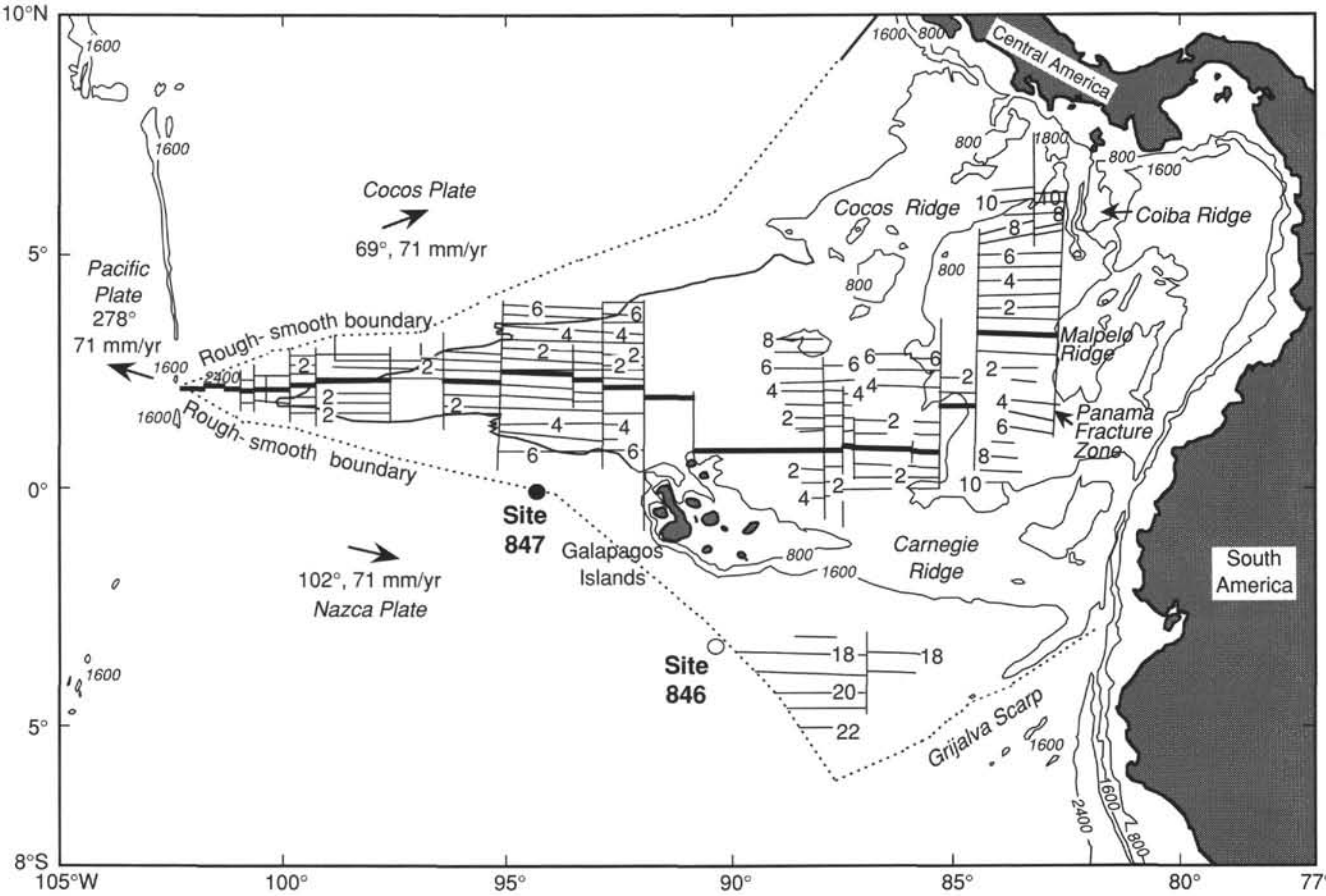

Figure 2. Tectonic setting and basement ages for the eastern equatorial Pacific Ocean (from Hey, 1977). Location of Sites 846 and 847 shown for reference.

Hole 847C

The vessel was then offset 20 m south and the bit was washed down to 2 mbsf where APC coring was initiated. Cores 847C-1H through -13H were taken over the interval from 2.0 to 125.5 mbsf, with orientation beginning on Core 847C-4H. The sub-bottom depth of 125.5 mbsf was approximately 5 m short of the overpull zone in Hole 847B, and the APC coring program at this hole was ended at this depth to avoid getting the core barrel stuck. The recovery in the APC section of Hole 847C was 104.3%.

Coring resumed with the XCB coring system, and Cores 847C-14X through -24X recovered sediment from 125.5 to 230.9 mbsf. During the cutting of Core 847B-25X (230.9–232.3 mbsf) a hard chert layer was encountered. Although care was taken to detect the change in rate of penetration corresponding to contact with the chert layer, the soft formation cutting shoe had severely worn cutting structures after only 5 min of rotation. The XCB coring was terminated at this point. Average recovery in the XCB section of Hole 847C was 90.7%.

After coring operations ceased, the pipe was pulled out of the hole and the mud line was cleared at 1550, 30 May, ending Hole 847C.

Hole 847D

The vessel was offset 20 m west and the bit lowered to 3344.2 m (approximately 2 m above the seafloor). The first piston core for this hole was taken at 1815, 30 May, and recovered 6.61 m of sediment, establishing mud line at 3346.9 mbrf for Hole 847D.

Piston coring continued to 130.1 mbsf (Core 847D-14H) with orientation beginning on Core 847D-4H. The depth objective for the hole was reached at Core 847D-14H, and the coring program for Site 847 was concluded. While the pipe was being pulled, the beacon was retrieved after a 34 min ascent to the surface. The bit reached the drill floor at 1014 hr, 31 May. At this point, the rig floor was secured, the hydrophones and thrusters raised, and by 1030 hr, 31 May, the vessel was underway to proposed site WEQ-5.

LITHOSTRATIGRAPHY

Introduction

At Site 847 there was continuous recovery of Pleistocene to upper Miocene (0.0–6.5 Ma) sediments down to chert at approximately 231 mbsf. The sedimentary sequence consists of nannofossil ooze with minor intervals of diatom ooze (Fig. 5).

Division of the sedimentary sequence into lithologic units was based on evaluation of several lithologic parameters including continuously measured GRAPE density, magnetic susceptibility, and percentage of color reflectance (Fig. 6), as well as percentages of components from smear slides, color, and sedimentary structures. Logging measurements (density, calcium, and silica) (see "Downhole Measurements" section, this chapter), %$CaCO_3$ measurements (see "Inorganic Geochemistry" section, this chapter), and laboratory measurements of density and water content (see "Physical Properties" section, this chapter) were also used to characterize lithologic changes. These physical lithologic parameters were helpful in evaluating the amount of calcite vs. biogenic silica and were consistent with laboratory measurements of %$CaCO_3$. With observations from smear slides, we were able to identify most components that constitute the calcareous and siliceous microfossil lithologic fractions.

Hole-to-hole correlations were made using GRAPE, susceptibility, color reflectance data, and visual descriptions of lithologic changes.

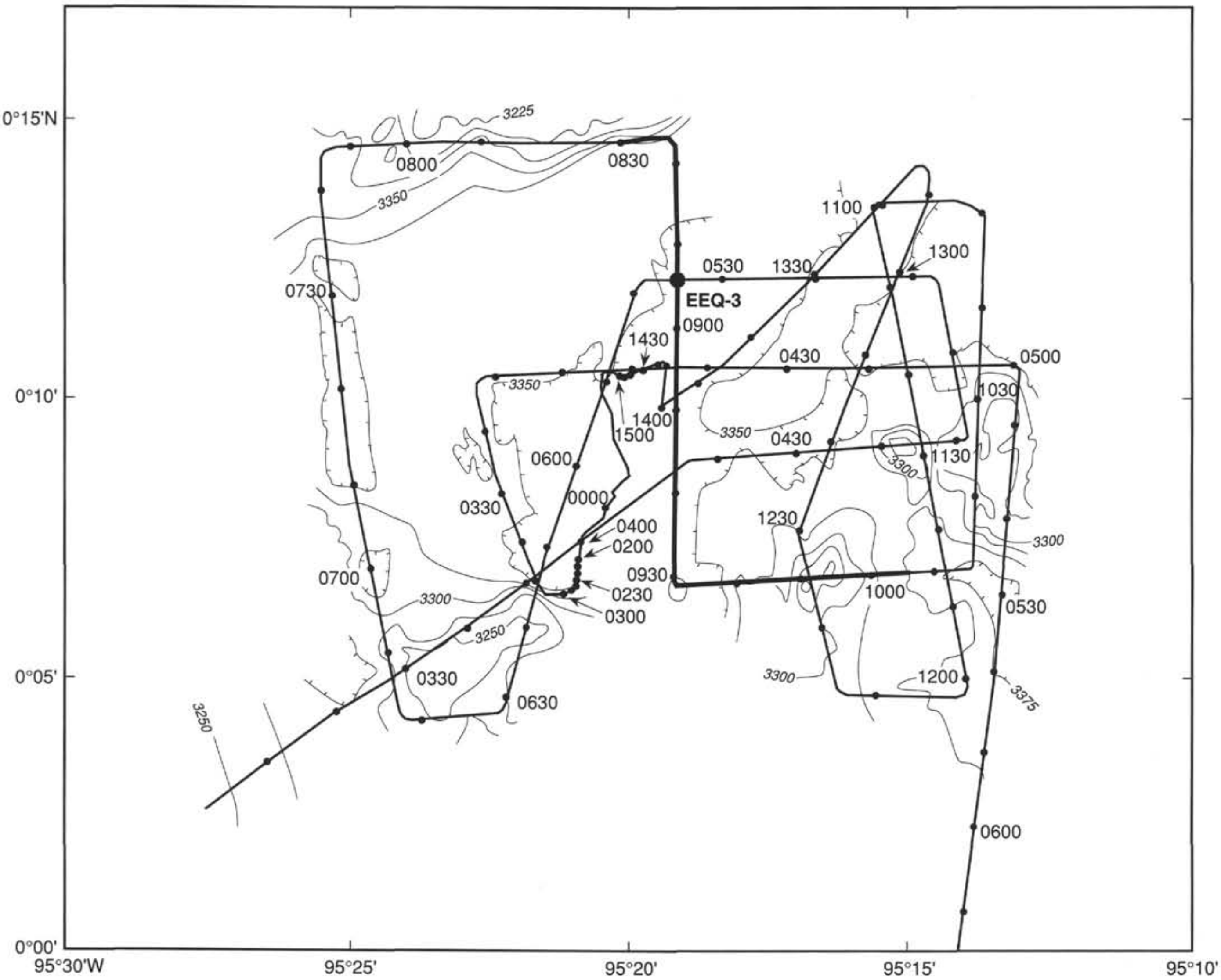

Figure 3. Hand-contoured SeaBeam map from navigation-adjusted SeaBeam contour maps collected on board the *Thomas Washington* during the Venture 1 cruise, September 1989. Proposed Site EEQ-3 is shown.

The complete sedimentary sequence was restored by patching together cores from all four holes (see "Sedimentation Rates" section, this chapter).

The entire sedimentary sequence comprises one lithologic unit of diatom nannofossil ooze and nannofossil ooze with thin (10–50 cm) interbeds of nannofossil diatom ooze and clayey diatom ooze. Diatom ooze also dominates two intervals (approximately 10 m thick) with ages of 1.45–2.0 Ma (47–63 mbsf) and 4.3–4.6 Ma (127–140 mbsf) (Fig. 5).

Unit I

Intervals:
- Cores 138-847A-1H
- Cores 138-847B-1H through -27X
- Cores 138-847C-1H through -25X
- Cores 138-847D-1H through -14H

Age: Pleistocene to late Miocene

Depth: 0–9.52 mbsf, Hole 847A; 0–241.54 mbsf, Hole 847B; 0–231.24 mbsf, Hole 847C; 0–130.10 mbsf, Hole 847D

Sediment Composition

The dominant lithologies of lithologic Unit I are diatom nannofossil ooze and nannofossil ooze with minor amounts of radiolarians (0%–13%), foraminifers (0%–18%), and clay (0%–15%) (Fig. 7). The interbedded minor lithologies (comprising <30% of the sedimentary sequence) are nannofossil diatom ooze and clayey diatom ooze. As a result of interbedding between the diatom-rich minor lithology and the nannofossil-rich dominant lithology, Unit I has carbonate values that range from 18.6% to 87.9%. Physical properties measurements also have a wide range of values due to variations in interbedded lithologies. Reflectance varies from 15% to 87% (Fig. 8). First-order variations in the physical property, %$CaCO_3$, and percentage of color reflectance data can be attributed to changes in the proportion of the nannofossil component relative to the diatom component. Clay is abundant in two intervals.

The color of the dominant diatom nannofossil oozes and nannofossil oozes is generally light greenish gray (5GY 6/1) to light gray

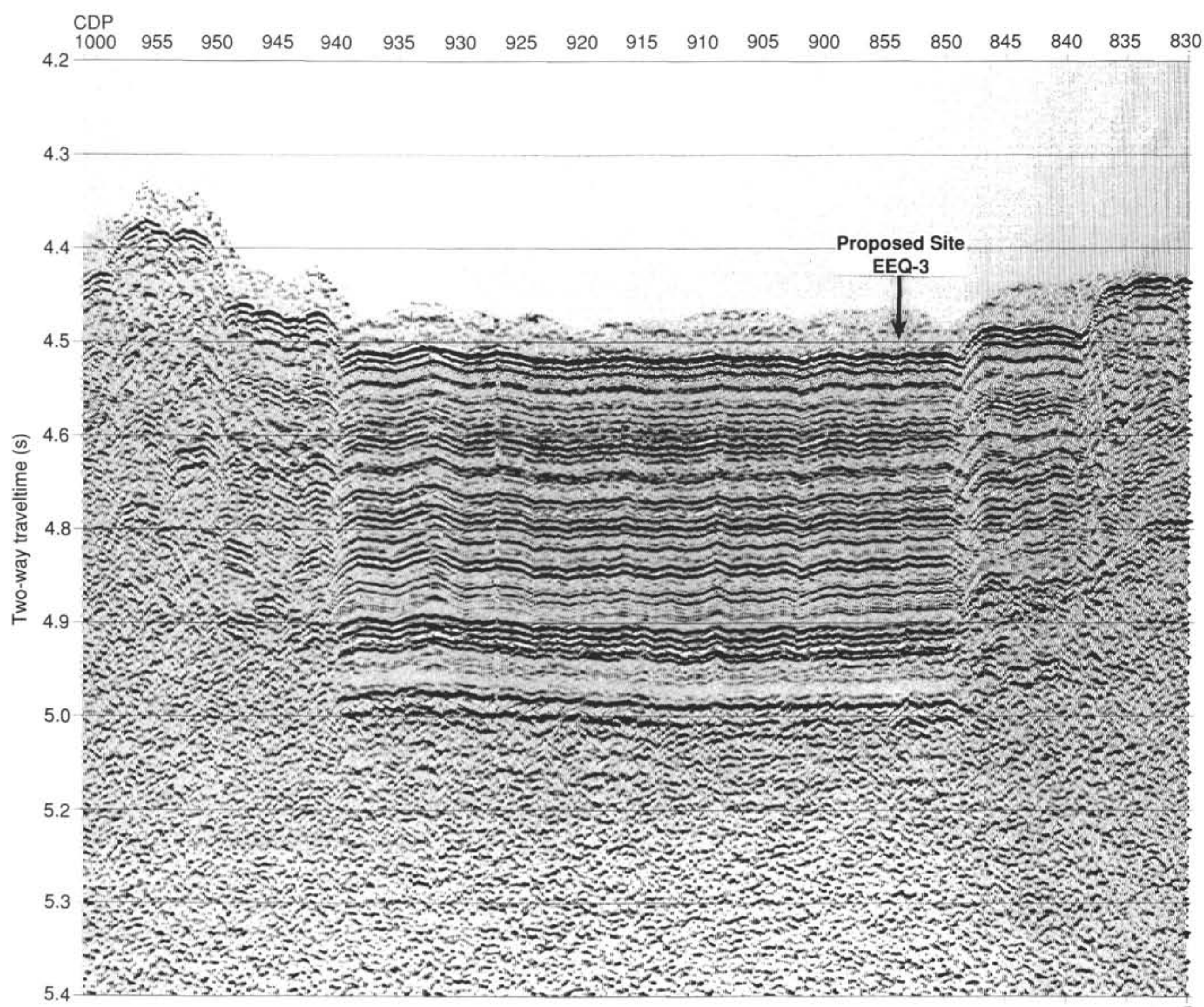

Figure 4. Seismic Line E. 80-in.[3] water-gun record collected on board the *Thomas Washington* Venture 1 cruise. Proposed Site EEQ-3 is shown.

(N7), although some darker intervals are gray (5Y 6/1) and greenish gray (5G 6/1). Color banding associated with compositional bedding is common (e.g., Fig. 9). Most of the compositional color banding is due to variations in the relative proportion of diatoms to nannofossils on the scale of decimeters. The interbedded diatom-rich intervals are olive (5Y 4/3) and light greenish-gray (5GY 7/1) in the top 50 mbsf, and light olive gray (5Y 6/2) below 50 mbsf. Post-depositional gray (N5) color banding and laminations (Fig. 10), due to sulfate-reduction organic matter diagenesis, are common down to 140 mbsf. These color bands and laminations, which are usually parallel to the bedding plane, often crosscut burrows indicating that diagenesis occurred after the sediments were buried below the bioturbated layer of the upper sediment column. In interval 138-847B-1H-1, 46–49 cm, a sharp color change occurs from olive brown (2.5Y 4/4) to greenish-gray (5GY 6/1 to 5GY 7/1) (Fig. 11) marking a change from oxidizing conditions above the brown/green transition to reducing conditions below (Lyle, 1983).

Although visual color observations serve to identify lithologic contacts and diagenetic features, automated color spectroscopy provided a more continuous and quantitative record of color changes. Examples of color reflectance spectra (Fig. 8) illustrate how the lithologies can be characterized by color. The ability of color spectroscopy to separate post-depositional color changes due to diagenesis, alteration, or recrystallization from changes due to lithological composition has not been completely tested. For example, it is not clear whether the spectral patterns of the two diatom oozes (Fig. 8) are different because of, for example, differences in the lithology or differences in the degree of reduction diagenesis. However, it appears that there is a correlation between lithology and reflectance patterns because carbonate-rich sediments have higher reflectance than siliceous sediments and a different reflectance spectrum (Fig. 8). The average and standard deviation of digitally recorded color reflectance percentages increase slightly downcore. In Hole B the average reflectance of the blue, red and IR bands is $40 \pm 7.8\%$ reflectance in the upper nannofossil ooze interval (0.0 – 47 mbsf), and is $50 \pm 9.1\%$ reflectance in the lower nannofossil ooze interval (180–231 mbsf). Increasing average reflectance with depth (Fig. 8) reflects a general decrease in the frequency of diatom ooze intervals, or in the relative percentages of diatoms within the nannofossil ooze intervals.

Bioturbation of the diatom nannofossil ooze and nannofossil ooze varies from slight to extensive. There appears to be slightly less bioturbation between approximately 60 and 140 mbsf. This interval is coincident

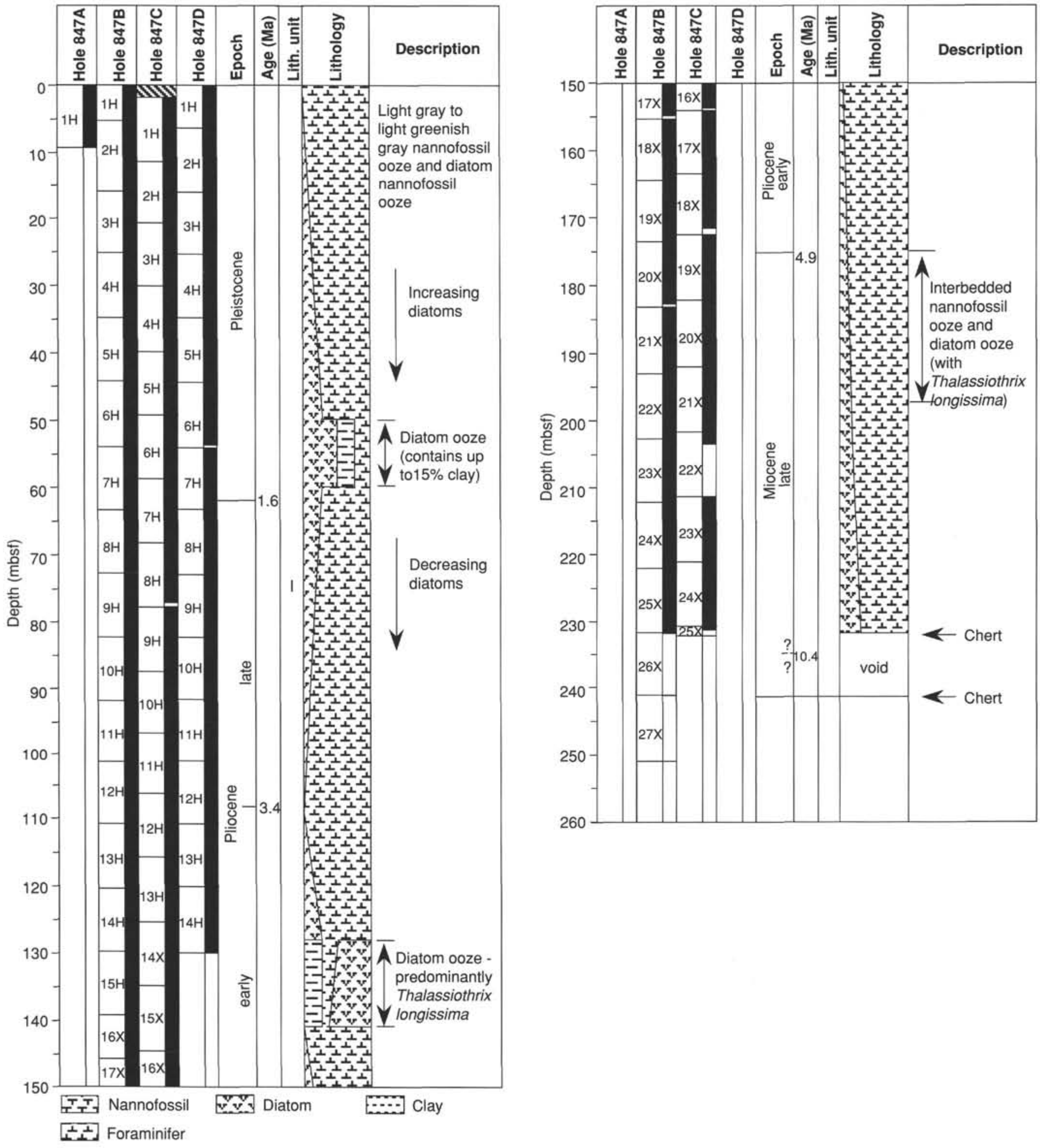

Figure 5. Lithostratigraphic summary of Site 847.

with the depth of the most extensive inferred diagenetic mottling, which may obscure trace fossils (see "Trace Fossils" section below).

Two intervals are dominated by 50-cm- to 100-cm-thick beds of diatom ooze and clayey diatom ooze interbedded with 10- to 50-cm-thick beds of diatom nannofossil ooze. The younger (1.45–2.0 Ma) of these intervals, is at 46.7–63.2 mbsf in Hole 847B, 47.3–62.1 mbsf in Hole 847C, and 45.6–62.7 mbsf in Hole 847D. The older (4.3–4.6 Ma) diatom-rich interval is at 127.4–139.8 mbsf in Hole 847B, and 129.0–140.0 mbsf in Hole 847C. The diatom-rich oozes in these intervals contain an average of 55% diatoms, 20% nannofossils, 5% radiolarians, 5% foraminifers, and 15% clay. Physical property and logging data are consistent with the observation that these two inter-

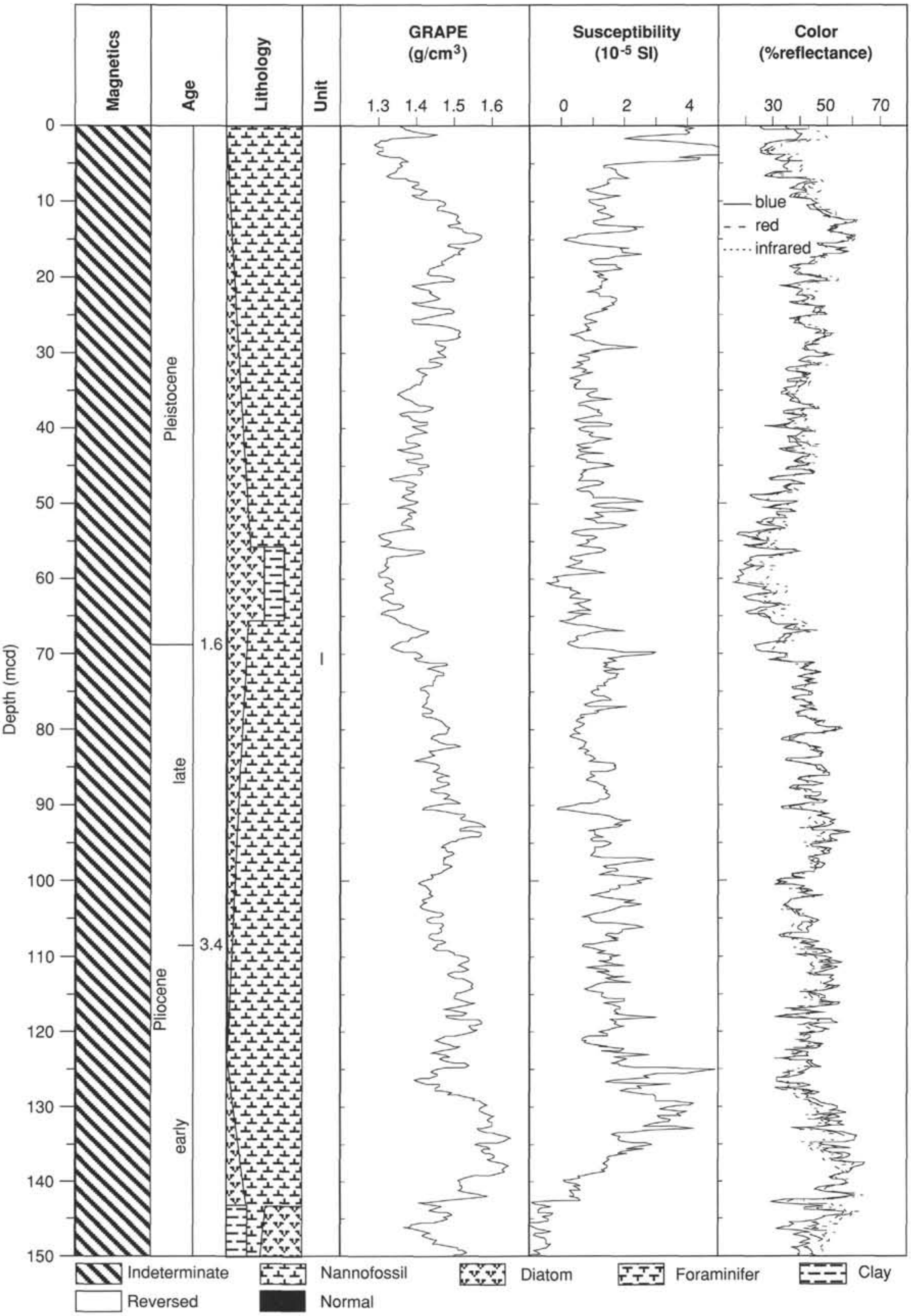

Figure 6. Composite summary of magnetics, age, graphic lithology, GRAPE, magnetic susceptibility, and color reflectance data for Site 847. The composite data consist of sections spliced together from the multiple holes drilled at the site. The data are shown plotted against meters composite depth (mcd), the new depth scale used when composite sections are constructed. The GRAPE, susceptibility, and color data are smoothed using a 20-point Gaussian filter.

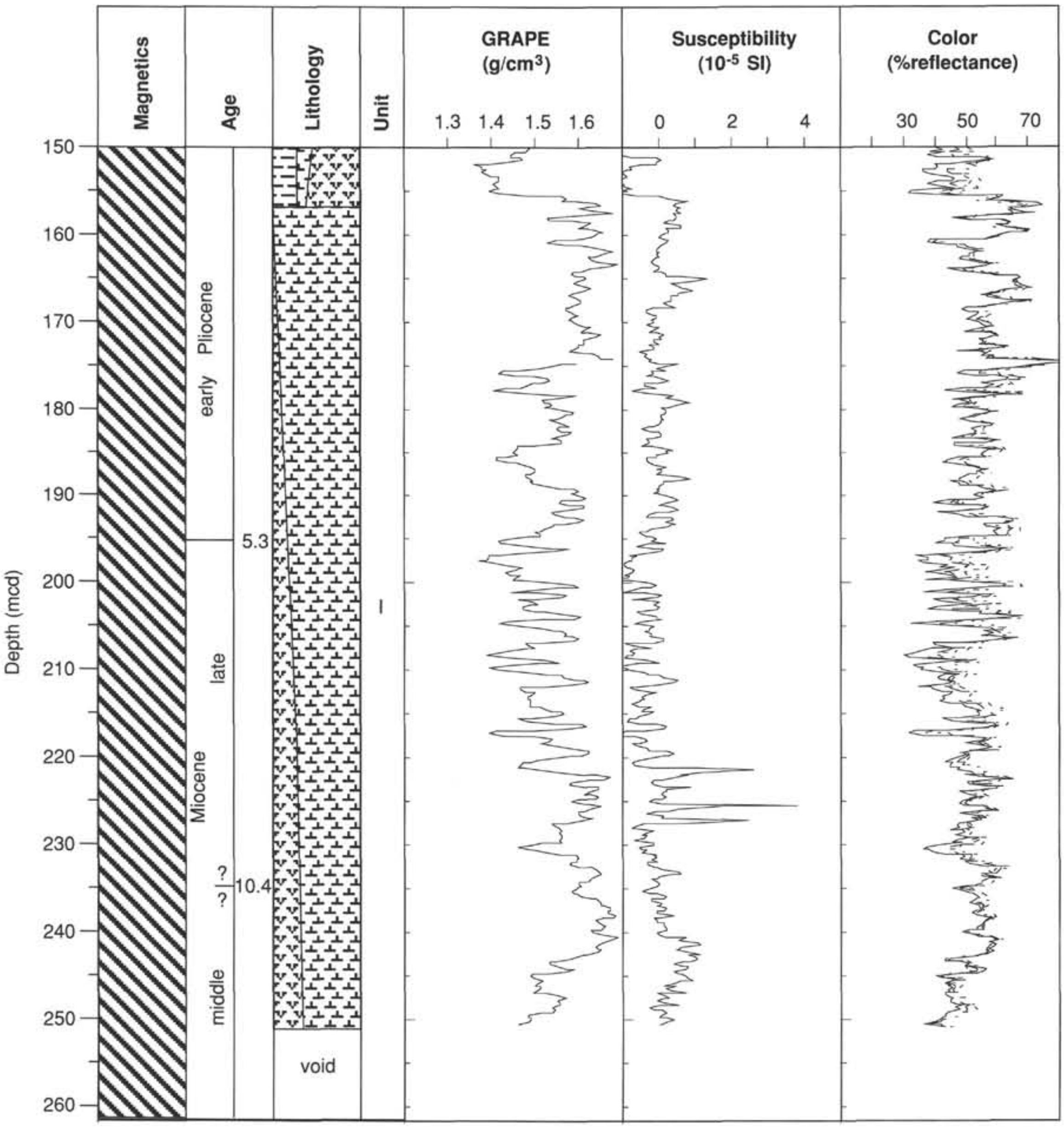

Figure 6 (continued).

vals are more siliceous. For example, in both these intervals, GRAPE and logging density values are low, water content values are high (see "Physical Properties" section, this chapter), and calcium (see "Downhole Measurements" section, this chapter) values are low relative to the average for the entire sedimentary sequence. Although these two diatom-rich intervals cannot be distinguished from each other by the smear slide component percentages, they are different in several respects. The younger interval is olive gray and has a more diverse assemblage of diatoms, while the older interval is light gray, is dominated by the diatom *Thalassiothrix longissima*, and contains submillimeter scale laminations. Several lithologic parameters are sensitive to the differences in the character of the younger diatom-rich interval relative to the older diatom-rich interval. Reflectance in the blue, red and infrared bands is lower than average in the younger diatom-rich interval, but not in the older interval. Magnetic susceptibility (see "Paleomagnetism" section, this chapter) is lower than average in the older diatom-rich interval, but not in the younger interval. Smear slide data and visual core descriptions indicate that thin (10–50 cm) interbedded diatom oozes below 150 mbsf (see Fig. 12) are compositionally more similar to the older thick diatom-rich interval of laminated *Thalassiothrix longissima* (particularly between 175 and 200 mbsf). This observation is in agreement with the higher reflectance values below 150 mbsf, and by the lower susceptibility values below 150 mbsf.

The color of the younger diatom-rich interval is olive gray (5Y 4/2), olive (5Y 4/3) and dark gray olive (5Y 3/2), while the older diatom-rich interval is light olive gray (5Y 6/2). The color spectroscopy data indicates that these two diatom-rich intervals differ not only in average reflectance values (as discussed above), but also in the reflectance of high (IR) wavelengths relative to low (blue) wavelengths. (The use of ratios of reflectance in different color bands to differentiate lithologic changes is discussed by Mix et al., this volume.)

Bioturbation varies widely in these diatom-rich intervals. In the younger interval, intense burrowing is present in the nannofossil

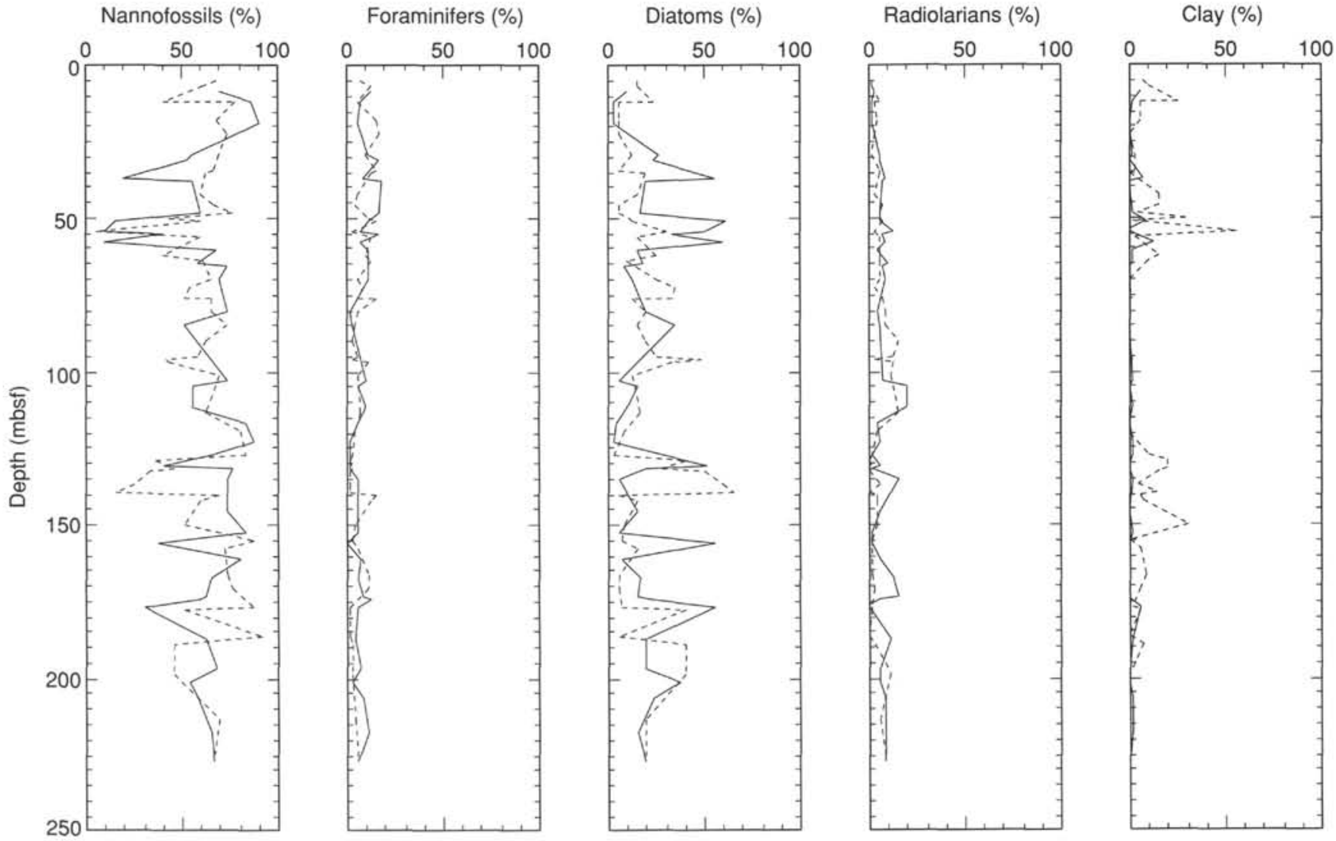

Figure 7. Smear slide data for Hole 847B (solid line) and Hole 847C (dashed line).

diatom ooze beds, but decreases in the beds that are the most diatom-rich (approximately 60% diatoms). In the older interval, bioturbation is difficult to see because the texture of the sediment is extremely rough. In the beds where sedimentary laminations exist there appears to be no bioturbation.

Small pieces of chert, approximately 3 to 4 cm in diameter, were recovered from the core catchers of Cores 138-847B-26X, -27X, and -847C-25X. These cherts were grayish-brown (5Y 5/2) and black (5Y 2.5/1). Since the XCB drilling could not break through the bottom chert layer, the total thickness of the layer is not known. The silica yield measured by the Geochemical Spectral Tool (see "Downhole Measurements" section, this chapter) is an order of magnitude higher than average from 241 mbsf to the base of Hole 847B (245 mbsf), indicating that the chert layer is at least 4 m thick above the bottom of Hole B. The chert from Sample 138-847B-27X-CC has small amounts of nannofossil ooze that apparently contain biostratigraphic nannofossil markers of early Miocene age (see "Biostratigraphy" section, this chapter). Unfortunately, a complete sedimentary sequence was not recovered below the bottom of Core 138-847B-25X (which has an approximate age of 6.5 Ma). Therefore, structural evidence for a hiatus or reworked sediments does not exist.

Trace Fossils

Bioturbation is common throughout the sequence recovered at Site 847 although trace fossils are indistinct in several cores due to the poor quality of the wire-cut surfaces. Solid burrows and *Planolites* are the most abundant trace fossils and occur throughout the sequence. Rind burrows with dark bluish "halos" are relatively common to depths of 120 mbsf but are very rare below this depth. Open burrows, which are partially filled with loose sulfide-rich material, occur to 80 mbsf. *Skolithos* is rare, but some pyritized vertical burrows occur near the diatom-rich intervals between 120–140 mbsf (Fig. 13). *Zoophycos* is common from 0–90 mbsf, but very rare below this depth. It is particularly common in the top 15 m and between 40 and 75 mbsf in the more diatom-rich interval (Fig. 14). In some cases, *Zoophycos* is observed only within the darker diatom-rich layers, where the general level of bioturbation is less than that of the surrounding carbonate sediment.

Burrowing is particularly indistinct between 140 and 165 mbsf, and cores in this interval show only irregular mottling. Other than very rare occurrences in burrow fill, *Chondrites* was not observed until around 165 mbsf from where it is common to abundant until 220 mbsf (Fig. 15). Complete pyritization of some *Chondrites* burrow networks occurs within this interval.

Summary of Lithology

The sedimentary sequence at Site 847 contains nannofossil ooze and diatom nannofossil ooze interbedded with diatom ooze and nannofossil diatom ooze. The interbedded diatom-rich intervals are generally 10–50 cm thick. There are two intervals, each approximately 10 meters thick, in which the sediments are dominated by diatom-rich sediments (46.7–63.2 mbsf, Hole B, and 127.4–139.8 mbsf, Hole B). The sedimentation rates (see "Sedimentation Rates" section, this chapter) during both the younger (1.45–2.0 Ma) and the older (4.3–4.6 Ma) of these diatom-rich intervals were higher than the average for the entire sequence. The older diatom-rich interval, as well as the underlying thinner interbedded intervals (with some laminations) are composed primarily of *Thalassiothrix longissima*. Foraminifer and radiolarian abundance varies between 0% and 15%. While the clay component is low (0%–7%) in the nannofossil-rich sediments, it composes a greater proportion (up to 15%) of the sediment in the two thick diatom-rich intervals.

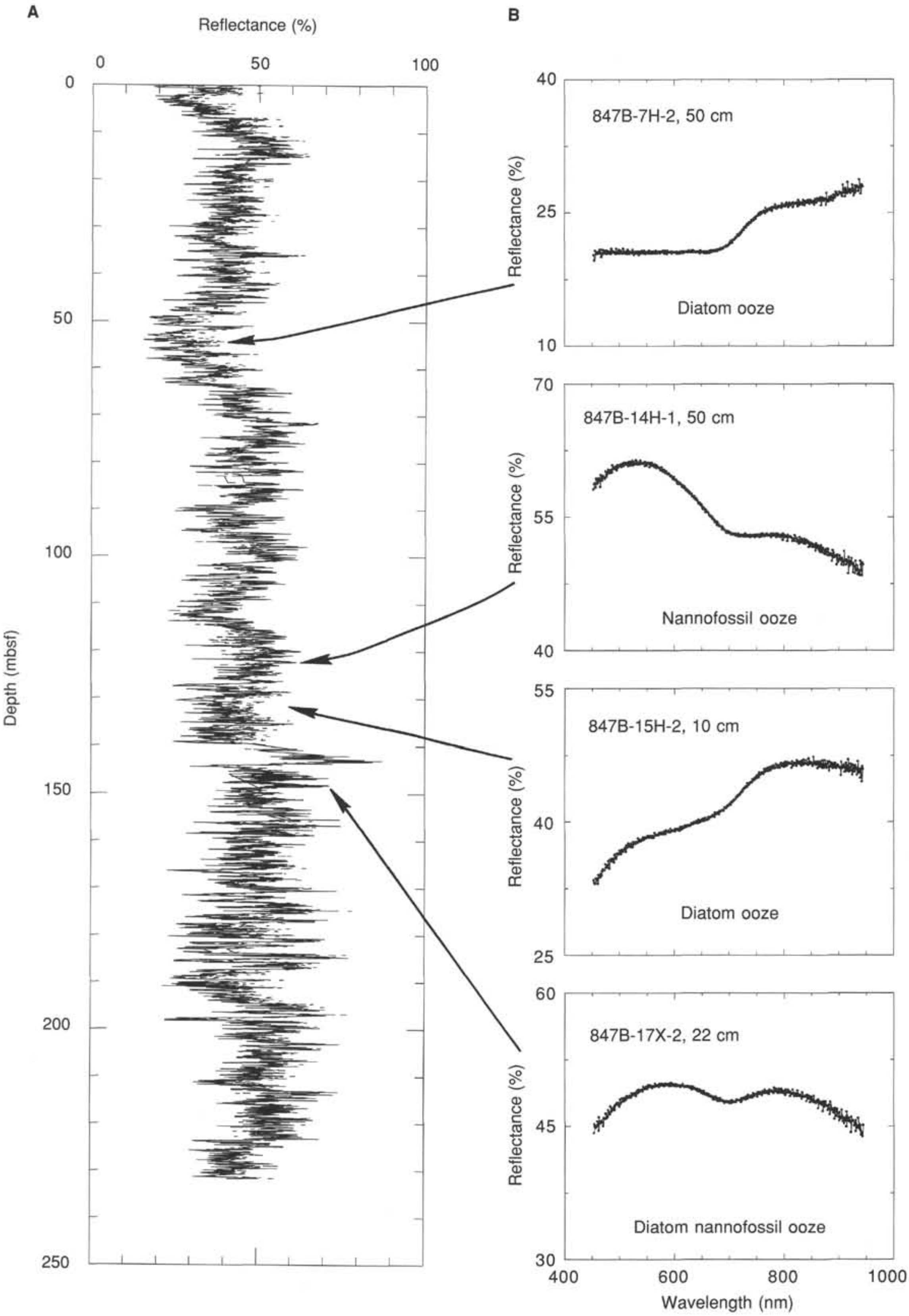

Figure 8. **A.** Percentage of reflectance in the blue (solid line), red (dashed line), and infrared (dotted line) color bands. **B.** Examples of reflectance spectra for four lithologic types.

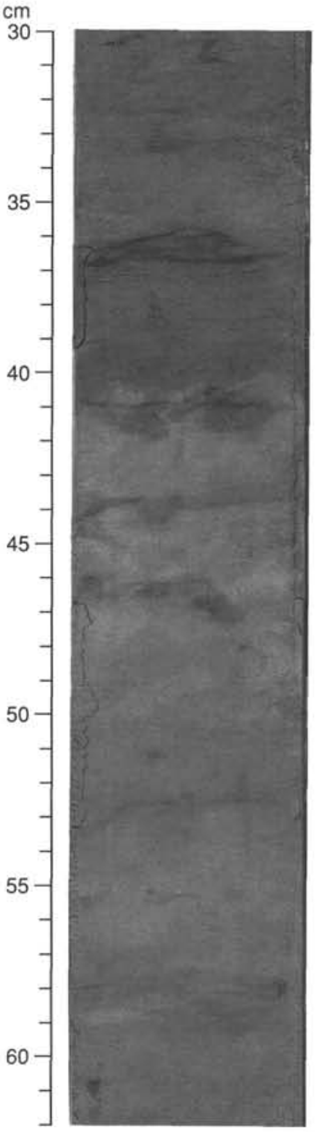

Figure 9. Example of color banding associated with lithological change from diatom-rich sediment (darker) to nannofossil-rich sediment (lighter) from Section 138-847B-6H-4, at 30–62 cm. Typically, contacts are obscured by bioturbation mixing between lithologies.

BIOSTRATIGRAPHY

Sediments recovered from the four holes (847A through 847D) cored at Site 847 provide a continuous sedimentary record for the late Pleistocene through the latest Miocene (equivalent to the last 6.1 m.y.). At the base of the sedimentary sequence a veneer of calcareous nannofossil ooze associated with a chert fragment yielded a calcareous nannofossil assemblage that contains common lower Miocene species mixed with rare middle and/or upper Miocene species. Rare, poorly-preserved radiolarians in this lowermost section suggest a late Miocene age, similar to that of overlying sediments.

Calcareous nannofossils, planktonic foraminifers, radiolarians, and diatoms are generally present throughout the section providing a well-constrained stratigraphy for the sequence recovered (Tables 3–6, Fig. 16). Calcareous nannofossils show good or moderate preservation in the Pleistocene through upper Pliocene interval, declining in the lower Pliocene and upper Miocene. Planktonic foraminifers exhibit good or moderate preservation in the upper Pleistocene. Foraminiferal preservation declines throughout the Pliocene and Miocene.

Table 1. Summary of coring operations at Site 847.

Core no.	Date (May 1991)	Time (UTC)	Depth (mbsf)	Length cored (m)	Length recovered (m)	Recovery (%)
138-847A-						
1H	28	0700	0.0–9.5	9.5	9.52	100.2
Coring totals				9.5	9.52	100.2
138-847B-						
1H	28	0745	0.0–6.5	6.5	6.59	101.0
2H	28	0825	6.5–16.0	9.5	9.58	101.0
3H	28	0905	16.0–25.5	9.5	10.02	105.5
4H	28	0955	25.5–35.0	9.5	10.08	106.1
5H	28	1040	35.0–44.5	9.5	10.09	106.2
6H	28	1130	44.5–54.0	9.5	10.10	106.3
7H	28	1215	54.0–63.5	9.5	10.10	106.3
8H	28	1300	63.5–73.0	9.5	9.33	98.2
9H	28	1350	73.0–82.5	9.5	10.10	106.3
10H	28	1440	82.5–92.0	9.5	10.18	107.1
11H	28	1530	92.0–101.5	9.5	9.56	100.0
12H	28	1615	101.5–111.0	9.5	10.08	106.1
13H	28	1700	111.0–120.5	9.5	10.05	105.8
14H	28	1745	120.5–130.0	9.5	9.85	103.0
15H	28	1850	130.0–139.5	9.5	9.81	103.0
16X	28	1950	139.5–145.8	6.3	9.48	150.0
17X	28	2035	145.8–155.4	9.6	9.33	97.2
18X	28	2120	155.4–164.7	9.3	9.69	104.0
19X	28	2205	164.7–173.9	9.2	9.82	107.0
20X	28	2250	173.9–183.5	9.6	9.34	97.3
21X	28	2330	183.5–193.2	9.7	9.85	101.0
22X	29	0015	193.2–202.8	9.6	9.77	102.0
23X	29	0100	202.8–212.5	9.7	9.63	99.3
24X	29	0140	212.5–222.2	9.7	9.77	101.0
25X	29	0225	222.2–231.9	9.7	9.81	101.0
26X	29	0330	231.9–241.5	9.6	0.14	1.5
27X	29	0540	241.5–247.0	5.5	0.04	0.7
Coring totals				247.0	242.19	98.1
138-847C-						
1H	30	0220	2.0–11.5	9.5	9.97	105.0
2H	30	0305	11.5–21.0	9.5	9.84	103.0
3H	30	0345	21.0–30.5	9.5	10.07	106.0
4H	30	0435	30.5–40.0	9.5	9.93	104.0
5H	30	0520	40.0–49.5	9.5	10.09	106.2
6H	30	0605	49.5–59.0	9.5	9.69	102.0
7H	30	0655	59.0–68.5	9.5	10.09	106.2
8H	30	0740	68.5–78.0	9.5	8.85	93.1
9H	30	0825	78.0–87.5	9.5	10.08	106.1
10H	30	0915	87.5–97.0	9.5	10.10	106.3
11H	30	1010	97.0–106.5	9.5	10.10	106.3
12H	30	1050	106.5–116.0	9.5	9.94	104.0
13H	30	1140	116.0–125.5	9.5	10.09	106.2
14X	30	1240	125.5–135.1	9.6	9.49	98.8
15X	30	1320	135.1–144.8	9.7	9.63	99.3
16X	30	1400	144.8–154.4	9.6	9.31	97.0
17X	30	1445	154.4–163.7	9.3	9.73	104.0
18X	30	1525	163.7–172.9	9.2	8.55	92.9
19X	30	1605	172.9–182.5	9.6	9.75	101.0
20X	30	1645	182.5–192.2	9.7	9.76	100.0
21X	30	1730	192.2–201.9	9.7	9.77	101.0
22X	30	1810	201.9–211.5	9.6	0.88	9.2
23X	30	1855	211.5–221.2	9.7	9.88	102.0
24X	30	1940	221.2–230.9	9.7	9.78	101.0
25X	30	2030	230.9–232.3	1.4	0.34	24.3
Coring totals				230.3	225.71	98.0
138-847D-						
1H	31	0015	0.0–6.6	6.6	6.61	100.0
2H	31	0100	6.6–16.1	9.5	9.94	104.0
3H	31	0150	16.1–25.6	9.5	9.74	102.0
4H	31	0240	25.6–35.1	9.5	9.90	104.0
5H	31	0325	35.1–44.6	9.5	9.78	103.0
6H	31	0410	44.6–54.1	9.5	9.14	96.2
7H	31	0455	54.1–63.6	9.5	9.54	100.0
8H	31	0540	63.6–73.1	9.5	9.60	101.0
9H	31	0625	73.1–82.6	9.5	10.15	106.8
10H	31	0710	82.6–92.1	9.5	9.68	102.0
11H	31	0800	92.1–101.6	9.5	10.09	106.2
12H	31	0845	101.6–111.1	9.5	9.91	104.0
13H	31	0935	111.1–120.6	9.5	9.99	105.0
14H	31	1022	120.6–130.1	9.5	9.50	100.0
Coring totals				130.1	133.57	102.7

Preservation of diatoms and radiolarians varies throughout the sequence from good to moderate.

Epoch boundaries are placed (approximated) as follows:

Boundary	Hole	Depth (mbsf)	Depth (mcd)	Event
Pleistocene/Pliocene	847B	48.1–49.6	53.18–54.68	B *Gephyrocapsa oceanica s.l.*
late/early Pliocene	847B	108.1–109.63	121.13–122.63	T. *Reticulofenestra pseudoumbilicus*
Pliocene/Miocene	847B	174.5–176	193.85–195.35	T. *Discoaster quinqueramus*

Table 2. Summary of logging operations at Site 847.

Local day	Local time	Cumulative hours	Base of string (mbsf)	Remarks
28 May 1991	23:40	0.0		Last core on deck
29 May 1991	2:00	2.3		Start rig up
29 May 1991	3:30	3.8		Geophysical tool rigged up (NGT/SDT/HLDT/DIT/TLT); RIH
29 May 1991	4:31	4.9	0.0	Pause at mudline
29 May 1991	4:35	4.9		Start downlog in pipe
29 May 1991	5:04	5.4	246.3	Stopped downlog; at TD; heave compensator on
29 May 1991	5:27	5.8	201.2	Start repeat log after first logging attempt needed recalibration
29 May 1991	5:46	6.1	128.3	Stop up log, go back to TD for main logging pass
29 May 1991	5:55	6.3	246.0	At TD, start main log up (NGT/SDT/HLDT/DIT/TLT)
29 May 1991	6:30	6.8	73.8	End repeat section; close calipers and POOH
29 May 1991	7:35	7.9		Geophysical tool string at well head
29 May 1991	9:25	9.8		RIH with geochemical string (NGT/ACT/GST/TLT)
29 May 1991	10:46	11.1	247.2	At TD; heave compensator on; calibrate while moving up slowly
29 May 1991	10:52	11.2	235.9	GST calibrated; go back to TD
29 May 1991	10:53	11.2	248.4	Start main log with geochemical string from TD
29 May 1991	11:30	11.8	155.4	Winch motor acting up; switched to backup
29 May 1991	11:30	11.8	169.5	Drop to here during motor change to prevent borehole activation; continue to log up
29 May 1991	12:05	12.4	67.7	Pause main log to turn heave compensator off before entering pipe
29 May 1991	12:22	12.7	0.0	Stop main log; POOH
29 May 1991	13:30	13.8		Geochemical string at wellhead
29 May 1991	15:00	15.3		RIH withFMS string (NGT/GPIT/FMS/TLT)
29 May 1991	16:15	16.6	0.0	At mud line; pause for 2 min
29 May 1991	16:26	16.8	247.2	At TD, start FMS main log; heave compensator on
29 May 1991	16:43	17.1	120.4	Noted intermittent short to caliper closing circuit; decided no repeat
29 May 1991	16:50	17.2	67.7	Stop main log, close calipers eventually, POOH
29 May 1991	18:00	18.3		FMS string at wellhead
29 May 1991	18:30	18.8		Rigged down from logging

The one core recovered from Hole 847A contains a microfossil assemblage characteristic of calcareous nannofossil Zones CN14b–CN15 (NN20–NN21) and the *Pseudoeunotia doliolus* diatom Zone. The following discussion focuses on biostratigraphic results from Holes 847B, 847C, and 847D.

Calcareous Nannofossils

Calcareous nannofossils recovered at Site 847 represent a stratigraphic succession from the upper Miocene (Zones CN9b and NN11) to the upper Pleistocene (Zones CN14b by Okada and Bukry, 1980; and NN20 by Martini, 1971). Calcareous nannofossils are abundant or common through the entire sequence and exhibit good to moderate preservation. Variations in abundance and preservation are shown in Figure 16. Calcareous nannofossil events recognized at Site 847 are presented in Table 3.

In the Pleistocene and Pliocene assemblages a slight etching affects placolith preservation, such as specimens of *Calcidiscus,* and some small reticulofenestrids. This slight etching, however, does not prevent the identification of the marker species. The Pleistocene assemblage is characterized by different morphotypes of *Gephyrocapsa* spp., *Pseudoemiliania lacunosa, Reticulofenestra* spp., *Calcidiscus* spp., helicoliths, and ceratolithids. The last occurrence of *P. lacunosa,* which defines the CN14a/CN14b (NN19/NN20) zonal boundary is recorded between Samples 847B-2H-5, 50 cm and -2H-6, 51 cm, and 847C-2H-1, 140 cm and -2H-1, 145 cm. The middle and lower Pleistocene nannofossil assemblage (Sections 847B-3H-1 through -6H-3) is assigned to Zones CN14a–CN13 (NN19). We have identified several stratigraphic events in this interval based on the different morphotypes of the *Gephyrocapsa* spp. taxonomic group, following Rio et al. (in press). These events are: (1) the first occurrence of *Gephyrocapsa* sp. 3 between Samples 847B-4H-2, 60 cm and -4H-3, 60 cm, and 847C-2H-CC and -3H-CC; (2) the first and last occurrences of specimens of *Gephyrocapsa* spp. larger than 5.5 μm placed in the interval between Samples 847B-5H-2, 60 cm, and -5H-CC; and (3) the first occurrence of *Gephyrocapsa oceanica* s.l., placed in the interval between Samples 847B-6H-3, 60 cm and -6H-4, 60 cm, and 847D-6H-CC and -7H-CC. In addition, the last occurrence of *Calcidiscus macintyrei* is placed just above the last occurrence of *G. oceanica* s.l. in Samples 847B-6H-2, 60 cm, 847C-5H-CC, and 847D-6H-CC.

The Pliocene nannofossil assemblage is characterized by the different morphotypes of *Reticulofenestra*, helicoliths, discoasterids, and ceratolithids. Sphenoliths are also characteristic of the lower Pliocene interval. Preservation varies throughout this interval. Some samples contain nannofossils exhibiting moderate overgrowth.

The last occurrence of *Discoaster brouweri*, recorded in Samples 847B-7H-7, 40 cm, 847C-7H-CC, and 847D-7H-CC, represents the upper boundary of Zone CN12d (NN18). Few specimens of *Discoaster triradiatus* occur with the interval assigned to Zone CN12d. The last occurrence of *Discoaster pentaradiatus,* which defines the top of Zone CN12c (NN17), is recorded in Sample 847B-9H-2, 60 cm. The last occurrence of *Discoaster surculus* is recorded in Sample 847B-9H-4, 60 cm, and *Discoaster tamalis* has its last occurrence in Samples 847B-9H-7, 40 cm, 847C-9H-CC, and 847D-9H-CC. The interval between these two events corresponds to Subzone CN12b

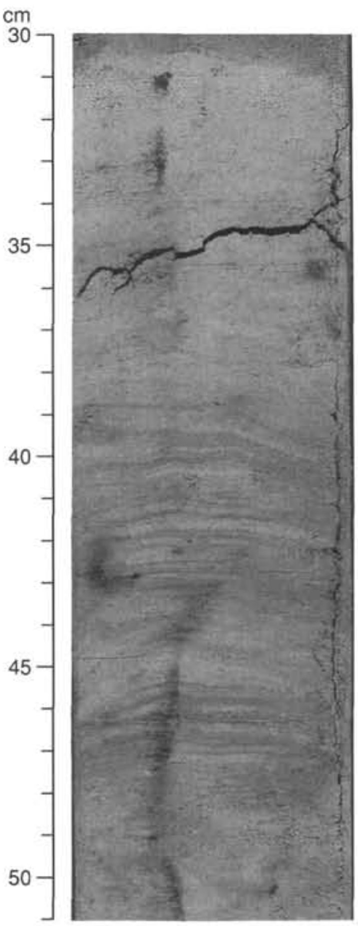

Figure 10. Example of diagenetic laminations caused by pyritization under reducing conditions from Section 138-847B-4H-7 at 30–51 cm.

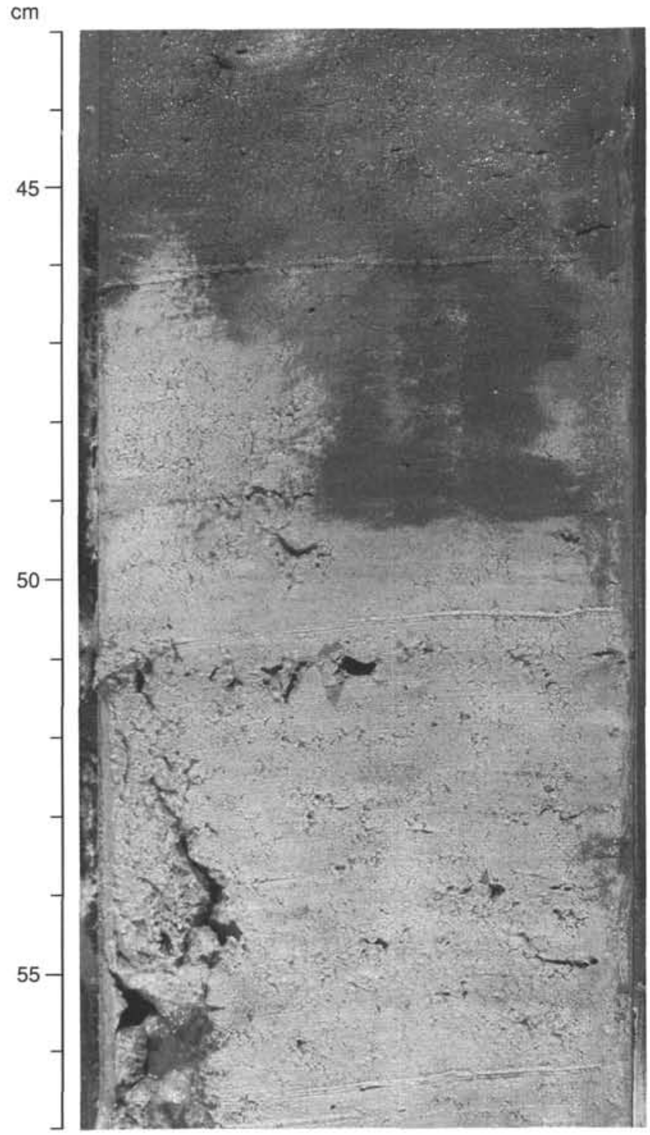

Figure 11. The brown/green transition in Section 138-847B-1H-1 at 43–57 cm, marking a change from oxidizing conditions above to reducing conditions below.

(upper NN16). The last occurrence of *Sphenolithus* spp. is located within Subzone CN12a between Samples 847B-12H-3, 60 cm, -12-4, 60 cm, Samples 847C-10H-CC and -11H-CC, and Samples 847D-10H-CC and -11-CC.

The boundary between Zones CN12 and CN11 (NN16/NN15), defined by the last occurrence of *Reticulofenestra pseudoumbilicus* is placed between Samples 847B-12H-5, 60 cm, and -12-6, 63 cm, 847C-11H-CC and -12H-CC, and 847D-11H-CC and -12H-CC. The last occurrences of *Amaurolithus primus* and *Ceratolithus acutus* approximates the boundary between Zones CN11 and CN10, and at Site 847 these events are recorded in Samples 847B-14H-5, 60 cm, and 847B-15H-1, 60 cm, respectively. *Ceratolithus rugosus* first occurs in Samples 847B-17X-5, 60 cm, and 847C-16X-CC marking the bottom of Subzone CN10c (NN13). *Ceratolithus acutus,* which defines the base of Subzone CN10b, is in Samples 847B-18X-6, 60 cm, and 847C-17X-CC.

In the upper Miocene interval, preservation of calcareous nannofossils decreases from good to moderate. The assemblage is characterized by the abundant presence of sphenoliths and *Reticulofenestra* spp., helicoliths, discoasterids, and sporadic ceratolithids. A marked increase of overgrowth in discoasterids is recorded in the lower interval at Site 847 (Cores 138-847B-22X through -25X) and prevents species identification. This interval is also characterized by reworked nannofossils typical of the lower Miocene.

The last occurrence of *Discoaster quinqueramus* was observed in Sample 138-847B-20X-2, 60 cm, and marks the CN9b/CN10a (NN11/NN12) zonal boundary. The presence of sporadic specimens of *Amaurolithus* spp. from Samples 138-847B-20X-2, 60 cm, through -25X-CC allows placing this interval in Subzone CN9b (NN11).

A calcareous ooze veneer associated with the chert fragments recovered from Sample 138-847B-27X-CC contains abundant calcareous nannofossils with moderate to good preservation. The nannofossil assemblage observed is characterized by abundant specimens of *Sphenolithus* spp., *Reticulofenestra* spp., *Dictyococcites* spp. with strongly overgrown discoasterids. In this assemblage, species restricted to the upper and middle Miocene are extremely rare. Among these, two poorly preserved specimens of five-rayed discoasterids and a few specimens of *C. macintyrei* and *R. pseudoumbilicus* were found after an extensive examination of nine different smear slides (22 × 30 mm) from the same sample. These species are associated here with common lower Miocene species such as *Sphenolithus conicus*, *S. dissimilis*, *Sphenolithus* cf. *belemnos* and few *Helicosphaera intermedia*.

Therefore, the sediments associated with the chert contain a mixture of upper and/or middle Miocene species and species typical of the lower Miocene. This assemblage dominated by lower Miocene

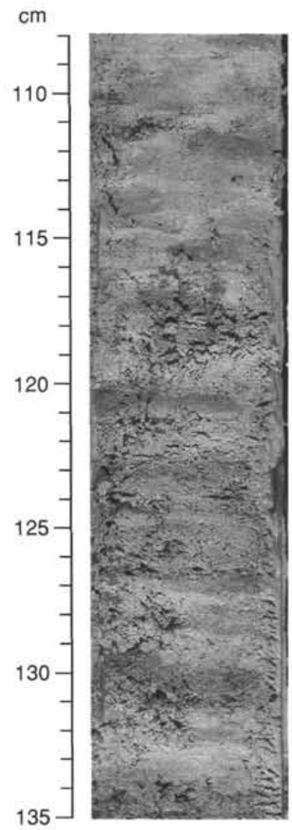

Figure 12. Diatom-rich interval from Section 138-847B-20X-3 at 108–135 cm. There are groups of submillimeter laminations of *Thalassiothrix longissima*. Color banding probably results from interbedding of diatom oozes with different quantities of nannofossils and clay.

species is difficult to interpret and could result from reworking of lower Miocene forms into younger sediments, or from contamination of rare middle to upper Miocene forms into lower Miocene sediments.

Planktonic Foraminifers

Planktonic foraminifers are common to abundant, and well to moderately-well preserved in the upper Pleistocene (Cores 138-847B-1H through -5H). Throughout the remainder of the section their preservation is poor, and their abundance decreases from few in Cores 847B-6H through -8H to rare below that interval. Throughout the entire sedimentary sequence radiolarians dominate the coarse-fraction residues. Other major coarse-fraction components common throughout most of the sequence are pyrite, echinoid spines, sponge spicules, and fish teeth.

The occurrence of pink *Globigerinoides ruber* in Sample 138-847B-1H-CC indicates that this interval is older than 0.125 Ma. The base of Zone N22 is placed in Sample 138-847B-8H-CC as is the first occurrence of *Globorotalia truncatulinoides* and the last occurrence of *Globorotalia limbata*. The base of Zone N21 is equated to the last occurrence at *Sphaeroidinellopsis* spp. in Sample 847B-12H-CC. The base of Zone N18 is tentatively placed in Sample 847B-18X-CC at the first occurrence of *Globorotalia tumida*, although this event may result from elimination of this species below that level by dissolution. The remainder of the section, assigned to the uppermost Miocene

Table 3. Sample interval, ODP depth, and composite depth constraints of calcareous nannofossil events for Holes 847B, 847C, and 847D.

	Hole 847B			Hole 847C			Hole 847D		
Event	Interval (cm)	Depth (mbsf)	Depth (mcd)	Interval (cm)	Depth (mbsf)	Depth (mcd)	Interval	Depth (mbsf)	Depth (mcd)
T *Pseudoemiliania lacunosa*	2H-5, 50–2H-6, 51	13.00–14.51	13.13–14.64	2H-1,140–2H-1,145	12.90–12.95	14.58–14.63			
B *Gephyrocapsa* sp. 3	4H-2, 60–4H-3, 60	27.60–29.10	30.43–31.93	2H-CC–3H-CC	21.34–31.07	23.03–33.47			
T >5.5 µm *Gephyrocapsa* spp.	5H-1, 60–5H-2, 60	35.60–37.10	38.40–39.90						
B >5.5 µm *Gephyrocapsa* spp.	5-CC–6H-1, 60	45.09–45.10	47.89–50.18						
T *Calcidiscus macintyrei*	6H-2, 60–6H-3, 60	46.60–48.10	51.68–53.18	4H-CC–5H-CC	40.43–50.09	43.73–54.59	5H-CC–6H-CC	44.88–53.74	49.08–59.94
B *Gephyrocapsa oceanica* s.l.	6H-3, 60–6H-4, 60	48.10–49.60	53.18–54.68				6H-CC–7H-CC	53.74–63.64	59.94–70.84
T *Discoaster brouweri*	7H-6, 60–7H-7, 40	62.10–63.40	68.85–70.15	6H-CC–7H CC	59.19–69.09	64.89–76.89	7H-CC–8H-CC	63.64–73.20	70.84–81.50
T *Discoaster pentaradiatus*	9H-1, 60–9H-2, 60	73.60–75.10	83.08–84.58						
T *Discoaster surculus*	9H-3, 60–9H-4, 60	76.60–78.10	86.08–87.58						
T *Discoaster tamalis*	9H-6, 70–9H-7, 40	81.20–82.40	90.68–91.88	8H-CC–9H-CC	77.35–88.08	85.55–97.98	7H-CC–8H-CC	63.64–73.20	70.84–81.50
T *Sphenolithus* spp.	12H-3, 60–12H-4, 60	105.10–106.60	118.13–119.63	10H-CC–11H-CC	97.60–107.10	108.30–119.00	10H-CC–11H-CC	92.28–102.19	103.98–114.89
T *Reticulofenestra pseudoumbilicus*	12H-5, 60–12H-6, 63	108.10–109.6	121.13–122.63	11H-CC–12H-CC	107.10–116.44	119.00–128.74	11H-CC–12H-CC	102.19–111.51	114.89–125.11
T *Amaurolithus primus*	14H-5, 60–14H-6, 60	127.10–128.60	142.58–144.08	12H-CC–13H-CC	116.44–126.09	128.74–139.94			
T *Ceratolithus acutus*	14-CC–15H-1, 60	130.35–130.60	145.83–146.55						
B *Ceratolithus rugosus*	17X-5, 60–17X-6, 60	152.40–153.90	171.75–173.25	16X-CC–17X-CC	154.11–164.13	173.51–184.13			
B *Ceratolithus acutus*	18X-6, 60–18X-7, 15	163.60–164.65	182.95–184.00	17X-CC–18X-CC	164.13–172.25	184.13–192.95			
T *Discoaster quinqueramus*	20X-1, 60–20X-2, 60	174.50–176.00	193.85–195.35	18X-CC–19X-CC	172.25–182.65	192.95–202.35			

T = top occurrence; B = bottom occurrence.

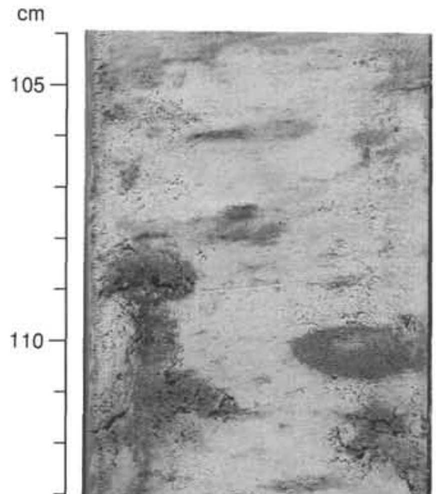

Figure 13. A vertical *Skolithos* burrow with a loose, pyrite-rich, fill cutting a solid burrow amid *Planolites* in Section 138-847D-14H-6 at 104–126 cm.

from other microfossil data, is tentatively placed in Zone N17, although no diagnostic marker for this interval was found. The dissolved assemblages in this interval consist mainly of rare robust forms including *Globoquadrina venezuelana*, *Globorotalia limbata,* and *Sphaeroidinellopsis* spp.

Planktonic foraminiferal datums identified in the sequence are given in Table 4. The last occurrence of *Dentoglobigerina altispira* in Sample 847B-14H-CC is unreliable at this site as it occurs stratigraphically lower than the last occurrence of *Sphaeroidinellopsis* spp. *Dentoglobigerina altispira* is more susceptible to dissolution than the latter species and the upper part of its range is curtailed here by dissolution.

Radiolarians

Radiolarians sampled at Site 847 range in age from the Quaternary (*Collosphaera tuberosa* Zone) to the late Miocene (*Didymocyrtis penultima* Zone). The most recent radiolarian zone (*Buccinosphaera invaginata*) was not identified, although it may be present in Section 847B-1H-1. It is clear from the description of this core (see "Lithostratigraphy" section, this chapter) that the uppermost, oxidized part of the sedimentary section was recovered. The oldest material recovered that could be identified to the zonal level (*D. penultima* Zone) is from Sample 847B-25X-CC.

Table 4. Sample interval, ODP depth, and composite depth constraints of planktonic foraminifer events for Hole 847B.

Event	Interval	Depth (mbsf)	Depth (mcd)
Pulleniatina coiling change from dextral above to sinistral	3H-CC–4H-CC	26.02–35.58	26.37–38.41
T *Globigerinoides fistulosus*	5H-CC–6H-CC	45.09–54.60	47.89–59.68
T *Globorotalia limbata*	7H-CC–8H-CC	64.10–72.83	76.89–81.01
B *Globorotalia truncatulinoides*	8H-CC–9H-CC	72.83–83.10	81.01–92.58
T *Globigerinoides obliquus*	8H-CC–9H-CC	72.83–83.10	81.01–92.58
T *Sphaeroidinellopsis* spp.	11H-CC–12H-CC	101.56–111.58	114.56–124.61
B *Pulleniatina spectabilis*	12H-CC–13H-CC	111.59121.05	124.61–135.05
B *Globorotalia tumida*	18H-CC–19H-CC	165.19–174.52	184.54–193.87

T = top occurrence; B = bottom occurrence.

Preservation and abundance of the radiolarians is generally good within the Pleistocene-Pliocene section. Slight dissolution and reprecipitation of biogenic silica does occur in this part of the section and necessitates the cleaning of many of the sieved residues with NaOH (even within Core 847B-1H). There was no detected reworking of older radiolarians into the younger part of the section.

The Pleistocene-Pliocene section is fairly complete, with nearly all the radiolarian zones and datums clearly identified. The *Anthocyrtidium jenghisi* Zone, however, is very compressed (Sections 847B-9H-3 through -9H-CC), and the *Phormostichoartus fistula* Zone could not be distinguished within the resolution of the sampling that was conducted (Table 5). Specimens of *P. fistula* do appear in the section, however, they are even rarer than usual and their last detected occurrence is coincident with that of *Phormostichoartus doliolum*. As in other sites of the eastern tropical Pacific Ocean, the appearances of *Amphirhopalum ypsilon* and *Spongaster tetras* are scattered. They do occur more commonly at this site than at other sites farther east, and their first occurrences are indicated in Table 5. The range of *Spongaster berminghami* was also impossible to define because of its very rare occurrence. A few specimens of *Spongaster pentas* were found in Core 847B-13H at and just below the first appearance of *S. tetras.*

Radiolarians are common to abundant throughout the upper Miocene part of the section and preservation is generally good. Only the two uppermost Miocene zones (*Didymocyrtis penultima* and *Solenosphaera omnitubus* Zones) were identified (Table 5). The placement of the upper boundary of the *S. omnitubus* Zone is difficult because of the rare and sporadic occurrence of *S. omnitubus* in Cores 847B-15H, -16X, and -17X. The boundary is tentatively placed between Samples 847B-17X-3 and -17X-CC, where the last consistent occurrence of *S. omnitubus* is found. The upper Miocene interval that was recovered appears to be expanded and offers good stratigraphic resolution. All of the major radiolarian datums above the last occurrence of *Calocycletta caepa* were identified in this section (Table 5). Specimens of *Acrobotrys tritubus* were not found in the samples studied.

Incomplete recovery of Cores 847B-26X and -27X, the occurrence of chert in these two cores, and the extremely poor preservation of the associated radiolarians make the assignment of an age to the deepest interval cored very speculative. A few highly altered radiolarians were recovered from a carbonate crust that was scraped from the surface of one of the pieces of chert (Sample 847B-27X-CC). The genera *Didymocyrtis, Lamprocyclas*, and *Dictyocorne*(?), and the species *Anthocyrtidium*(?) *pliocenica* and *Sticho-*

Table 5. Sample interval, ODP depth, and composite depth constraints for radiolarian events at Holes 847B, 847C, and 847D.

	Hole 847B			Hole 847C			Hole 847D		
Event	Interval	Depth (mbsf)	Depth (mcd)	Interval	Depth (mbsf)	Depth (mcd)	Interval	Depth (mbsf)	Depth (mcd)
B *Buccinosphaera invaginata*									
T *Stylatractus universus*	2H-5–2H-CC	13.60–16.08	13.78–16.21				1H-CC–2H-CC	6.61–16.54	6.61–18.34
B *Collosphaera tuberosa*	2H-CC–3H-3	16.08–20.10	16.21–20.45				2H-CC–3H-CC	16.54–25.84	18.34–28.84
T *Lamprocyrtis neoheteroporus*	4H-3–4H-5	29.60–32.60	32.43–35.43	2H-CC–3H-CC	21.34–31.07	23.02–33.47			
T *Anthocyrtidium angulare*	4H-3–4H-5	29.60–32.60	32.43–35.43	3H-CC–4H-CC	31.07–40.43	33.47–43.73			
T *Theocorythium vetulum*	4H-CC–5H-3	35.58–39.10	38.41–41.90				3H-CC–4H-CC	25.84–35.50	28.84–39.50
B *Lamprocyrtis nigriniae*	5H-5–5H-CC	42.10–45.09	44.50–47.89						
B *Theocorythium trachelium*	5H-CC–6H-3	45.09–48.60	47.89–53.68				4H-CC–5H-CC	35.50–44.88	39.50–49.08
B *Pterocorys minithorax*	5H-5–5H-CC	42.10–45.09	44.50–47.89						
B *Anthocyrtidium angulare*	6H-3–6H-5	48.60–51.60	53.68–56.68	5H-CC–6H-CC	50.09–59.19	54.59–64.89			
T *Pterocanium prismatium*	6H-3–6H-5	48.60–51.60	53.68–56.68	5H-CC–6H-CC	50.09–59.19	54.59–64.89			
T *Lamprocyrtis heteroporus*	7H-5–7H-CC	61.09–64.10	67.84–70.85				6H-CC–7H-CC	53.74–63.64	59.94–70.84
T *Anthocyrtidium jenghisi*	9H-3–9H-5	77.10–80.10	86.58–89.58						
B *Theocalyptra davisiana*	9H-5–9H-CC	80.10–83.10	89.58–92.58				8H.CC–9H-CC	73.20–83.25	81.50–91.95
T *Stichocorys peregrina*	9H-5–9H-CC	80.10–83.10	91.95–92.58				9H-CC–10H-CC	83.25–92.28	91.95–103.98
T *Anthocyrtidium pliocenica*	11H-3–11H-5	96.10–99.10	109.00–112.00						
B *Lamprocyrtis neoheteroporus*	10H-3–10H-5	86.59–89.59	97.98–99.82	9H-CC–10H-CC	88.08–97.60	97.98–108.30			
B *Lamprocyrtis heteroporus*	10H-CC–11H-3	92.68–96.10	102.91–109.00	10H-CC-11H-CC	97.60–107.10	108.30–119.00	10H-CC–11H-CC	92.28–102.19	103.98–114.89
T *Phormostichoartus fistula*	12H-CC–13H-3	111.58–115.10	124.61–129.10	12H-CC-13H-CC	116.40–126.09	128.74–139.94			
T *Lychnodictyum audax*	11H-CC–12H-3	101.56–105.60	114.46–118.63						
T *Phormostichoartus doliolum*	12H-CC–13H-3	111.58–115.10	124.61–129.10	12H-CC-13H-CC	116.40–126.09	128.74–139.94			
B *Amphirhopalum ypsilon*	11H-CC–12H-3	101.56–105.60	114.46–118.63						
B *Spongaster tetras*	13H-3–13H-5	115.10–118.10	129.10–132.10						
T *Didymocyrtis penultima*	13H-3–13H-5	115.10–118.10	129.10–132.10				13H-CC–14H-CC	121.15–130.10	134.95–145.10
B *Pterocanium prismatium*	16H-3–16H-5	143.60–146.10	160.05–162.55						
T *Solenosphaera omnitubus*	17X-3–17X-CC	149.90–155.10	169.25–174.48						
T *Siphostichartus corona*	20X-3–20X-5	177.99–181.00	197.34–200.35						
T *Stichocorys johnsoni*	25X-3–25X-5	226.29–229.30	245.64–248.64						
Stichocorys delmontensis > *S. peregrina*	24X-CC–25X-3	222.27–226.30	241.62–245.64						
T *Calocycletta caepa*	24X-5–24X-CC	218.60–222.30	237.95–241.62						

T = top occurrence: B = bottom occurrence: > = evolutionary transition.

Table 6. Sample interval, ODP depth, and composite depth constraints for diatom events at Hole 847B, 847C, and 847D.

	Hole 847B			Hole 847C			Hole 847D		
Event	Interval	Depth (mbsf)	Depth(mcd)	Interval	Depth (mbsf)	Depth (mcd)	Interval	Depth (mbsf)	Depth (mcd)
T *Nitzschia reinholdii*	1H-CC–2H-6	6.59–14.70	6.59–14.83	1H-CC–2H-CC	11.97–21.34	12.37–23.02	1H-CC–2H-CC	6.61–16.54	6.61–18.34
T *Nitzschia fossils*	2H-CC–3H-3	16.08–19.70	16.21–20.05	2H-CC–3H-CC	21.34–31.07	23.02–33.47	2H-CC–3H-CC	16.54–25.84	18.34–28.84
T *Rhizosolenia praebergonii* var. *robustus*	6H-1–6H-4	45.10–51.10	50.18–56.19	5H-6–5H-CC	47.70–50.09	52.20–54.49	5H-CC–6H-CC	44.88–53.74	49.08–59.94
B *Pseudoeunotia doliolus*	7H-5–7H-6	60.60–62.10	67.35–68.85	6H-CC–7H-CC	59.19–69.09	64.89–76.89	6H-CC–7H-CC	53.74–63.64	59.94–70.84
T *Thalassiosira convexa* var. *convexa*	8H-6–8H-CC	71.60–72.83	79.78–81.01	7H-CC–8H-CC	69.09–77.35	76.89–85.55	7H-CC–8H-CC	63.64–73.20	70.84–81.50
T *Nitzschia jouseae*	9H-CC–10H-2	83.10–84.60	92.58–94.83	9H-CC–10H-CC	88.08–97.60	97.98–108.30	9H-CC–10H-4	83.25–89.80	91.91–101.50
B *Rhizosolenia praebergonii*	10H-CC–11H-CC	92.68–101.56	102.91–114.46	10H-2–10H-4	90.40–93.40	101.10–104.10	10H-CC–11H-CC	92.28–102.19	103.98–114.89
T *Actinocyclus ellipticus* var. *lanceolata*	11H-CC–12H-CC	101.56–111.58	114.46–124.61						
T *Thalassiosira convexa* var. *convex*	12H-5–12H-CC	108.20–111.58	122.23–124.61	11H-CC–12H-CC	107.10–116.44	119.00–128.74	11H-CC–12H-CC	102.19–111.51	114.89–125.11
B *Asteromphalus elegans*	13H-2–13H-CC	113.10–121.05	127.10–135.05						
T *Nitzschia cylindrica*	14H-CC–15H-CC	130.35–139.81	145.83–155.76	15H-6–15H-CC	143.35–144.73	159.25–160.63			
B *Nitzschia jouseae*	18H-2–18H-4	157.90–160.90	177.25–180.25	17H-CC–18H-3	164.13–167.90	184.13–188.60			
B *Thalassiosira oestrupii*	18H-CC–19H-CC	165.19–174.52	184.54–193.87	18H-CC–19H-CC	172.25–182.65	192.95–202.35			
T *Nitzschia miocenia*	19H-CC–20H-5	174.52–180.50	193.87–199.85	20H-1–20H-2	183.70–185.20	203.40–204.90			
T *Thalassiosira praeconvexa*	22H-CC–23H-1	202.97–203.40	222.32–222.75	21H-3–21H-5	196.20–198.70	215.60–218.10			

corys delmontensis could be identified within this sample. Although these identifications are not sufficient to give a definitive age to the sample, they do suggest that it is not greatly older than the material recovered in Core 847B-25X.

Diatoms

Few through abundant diatoms are present in the Quaternary through upper Miocene sequence recovered from Holes 847A to 847D. Diatom preservation is variable ranging from poor to good. The Pliocene diatom assemblage is characterized by: *Azpeitia nodulifer, Nitzschia fossilis, Nitzschia jouseae, Nitzschia marina, Nitzschia reinholdii, Pseudoeunotia doliolus, Rhizosolenia bergonii, Rhizosolenia praebergonii, Roperia tesselata, Thalassionema nitzschioides,* and *T. nitzschioides* var. *parva, Thalassiosira convexa, Thalassiosira oestrupii,* and *Thalassiothrix longissima.* The Miocene assemblage is characterized by: *Actinocyclus ellipticus, Nitzschia cylindrica, Nitzschia miocenica, Thalassionema nitzschioides,* and *Thalassiothrix longissima.*

The occurrence of *P. doliolus* without *N. reinholdii* places Samples 847A-1H-CC, 847B-1H-CC, 847C-1H-CC and 847D-1H-CC in the Quaternary *P. doliolus* Zone. Samples 847B-2H-CC through -6H-CC, 847C-2H-CC through -5H-CC, and 845D-2H-CC through -5H-CC are assigned to Subzone A of the *N. reinholdii* Zone based on the co-occurrence of *N. reinholdii* and *P. doliolus*. The last occurrence of *Nitzschia fossilis* and the silicoflagellate *Mesocena quadrangula* in Samples 847B-3H-3, 70 cm; 847C-3H-CC, and 847D-3H-CC supports this zonal assignment.

The co-occurrence of *Rhizosolenia praebergonii* var. *robustus* and *P. doliolus* allows Samples 847B-6H-CC, 847C-5H-CC, and -6H-CC, and 847D-6H-CC to be assigned to Subzone A of the *N. reinholdii* Zone. The base of this subzone, defined by the first occurrence of *P. doliolus,* is placed in Samples 847B-6H-CC, 847C-6H-CC, and 847D-6H-CC.

Samples 847B-7H-CC through -10H-CC, 847C-7H-CC through -10H-2, 148 cm, and 847D-7H-CC through -10H-CC are assigned to the *R. praebergonii* Zone. The last occurrences of *T. convexa* var. *convexa* and *N. jouseae* occur within this stratigraphic interval and allow recognition of the C/B and B/A subzonal boundaries, respectively. The last occurrence of *T. convexa* var. *convexa* is placed in Samples 847B-8H-CC, 847C-8H-CC, and 847D-8H-CC. The last occurrence of *N. jouseae* is assigned to Samples 847B-10H-CC, 847C-10H-CC, and 847D-10H-4, 120 cm.

Samples 847B-10H-CC through 18H-2, 90 cm, 847C-10H-CC through -17X-CC, and 847D-10H-4, 120 cm, through -14H-CC (base of Hole 847D) are assigned to the *N. jouseae* Zone. The last occurrence of *Nitzschia cylindrica* is placed in Samples 847B-15H-CC and 847C-15X-CC. Specimens of *Thalassiothrix longissima* are common to abundant throughout this interval.

The remaining lower portion of Holes 847B and 847D that contains diatoms (Cores 847B-18X-4, 90 cm, through -26X-CC and 847C-18X-3, 120 cm, through -25X-CC) is assigned to the *T. convexa*

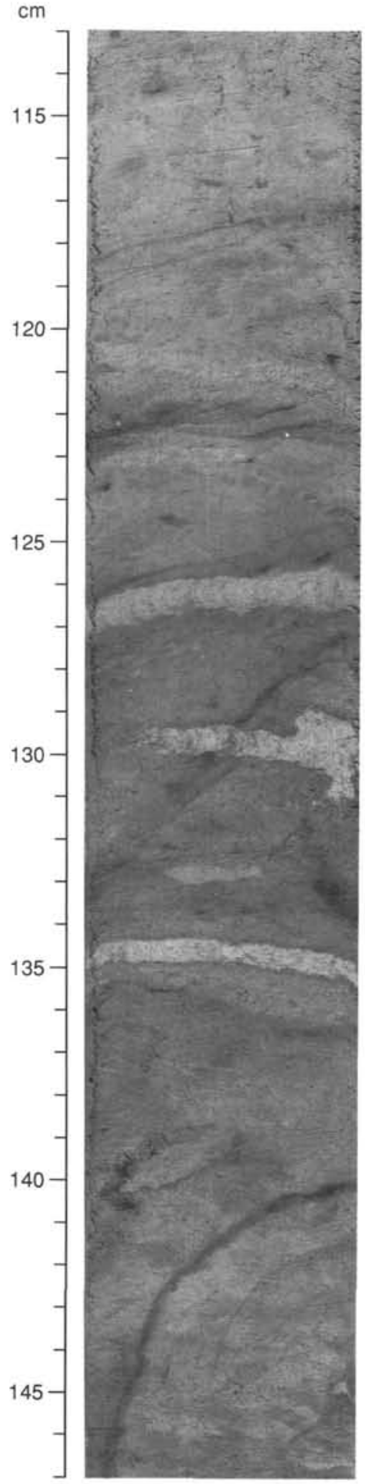

Figure 14. A series of *Zoophycos* burrows in a more diatom-rich bed in Section 138-847C-8H-5 at 113–147 cm.

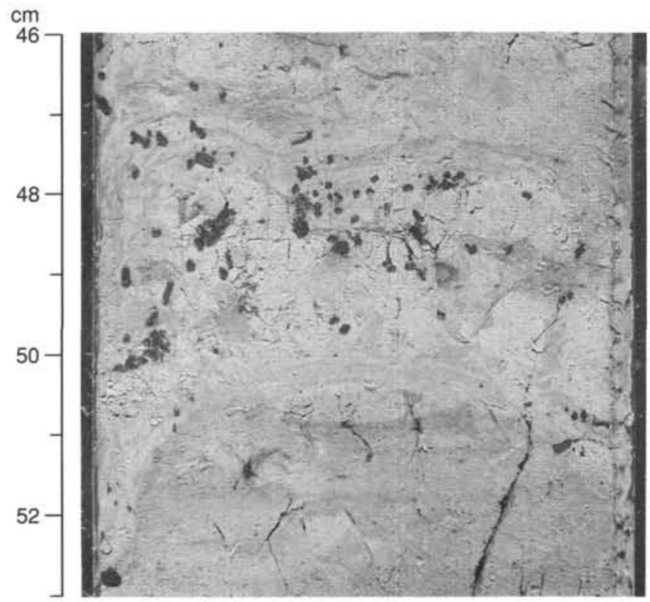

Figure 15. A completely pyritized *Chondrites* burrow network in Section 138-847C-23X-7 at 46–53 cm.

Zone based on the occurrence of *T. convexa* stratigraphically below the first occurrence of *N. jouseae*. The sporadic occurrence of *Thalassiosira miocenica* within this interval disallows the recognition of Subzone C of the *T. convexa* Zone. The interval between Samples 847B-20X-5, 60 cm, through -22X-CC and 847C-20X-2, 120 cm, through -21X-3, 100 cm is equivalent to Subzone B of this zone. This assignment is based on the rare occurrence of *N. miocenica* stratigraphically above the last occurrence of *Thalassiosira praeconvexa*. The interval between Samples 847B-23X-1, 60 cm through -26X-CC and -21X-5, 50 cm, through -25X-CC is equivalent to Subzone A, defined as the interval from the first occurrence of *T. convexa* to the last occurrence of *Thalassiosira praeconvexa*. The occurrence of *T. miocenica* in several of these samples supports this zonal assignment. Below this interval diatoms were absent.

PALEOMAGNETISM

Remanent Magnetization

The natural remanent magnetization (NRM) of the sediments recovered at Site 847 is, as with previously cored sites, dominated by a steep upward component. The intensity of NRM is on the order of 1 mA/m and is thus readily measurable with instruments on board the ship; after 15 mT demagnetization, however, the intensity was reduced to about 0.1 mA/m, which is at the limit of measurement capabilities. Consequently, the remanence directions we obtained are generally quite scattered. Exceptions occur over limited intervals of a few meters length, where the intensity is perhaps slightly higher and remanence directions appear more stable.

Because of the poor results obtained from Core 847A-1H and the 15 APC cores of Hole 847B, we suspended remanence measurements without studying the XCB cores from Hole 847B and measured only

Cores 847C-1H through -4H of Hole 847C. Our measurements were uniformly performed after 15 mT demagnetization except for 2 sections per core for which we also measured the NRM. The relatively stable intervals found in Hole 847B include 0–5 mbsf, 10–15 mbsf, 19–23 mbsf, 27–31 mbsf, 55–57 mbsf, 87–90 mbsf, 97–101 mbsf, 114–120 mbsf, and 125–129 mbsf. The upper 5 m of sediment appear particularly stable in Core 847B-1H, with relatively strong magnetization intensity (about 1 mA/m after demagnetization) and shallow inclinations that are appropriate for this equatorial site. The other intervals specified are much less regular, but do have largely consistent declinations. In particular, the interval between 114 and 120 mbsf contains a distinct declination shift of about 140° that could possibly reflect a polarity reversal. Clearly these sediments will require study with a more sensitive magnetometer to determine whether a primary remanence signal might be present in this sequence.

Susceptibility

The susceptibilities measured from Holes 847B, 847C, and 847D fall almost entirely in the range of -1 to 3×10^{-5} SI. The susceptibility signal, like magnetization intensity, is highest in the uppermost few meters of sediment. Interestingly, a distinct interval of diamagnetic susceptibility (distinct negative values) coincides with the diatom-rich zone at 143–155 mcd (Fig. 17). The reason for the correspondence is unknown.

Despite the generally weak signal level at Site 847, the susceptibility remains useful for intra-site correlations (see Site 847, "Sedimentation Rates" section, this volume). Susceptibility measurements, although low at Site 847, clearly display many thin zones of relatively high susceptibility that correlate well from hole to hole and so cannot result from contaminants such as rust particles (Fig. 18), although such erratic readings do occur (particularly near the tops of cores). The multiple susceptibility records available from the three holes thus confirm that many of the spikes, which otherwise might appear to be spurious, do in fact constitute a real signal.

SEDIMENTATION RATES

A sedimentary section almost 250 m thick covering the time interval from the late Pleistocene to the late Miocene was recovered at Site 847. Biostratigraphic age control was provided by all four of the chief planktonic microfossil groups.

The composite depth section for Site 847 is given in Table 7. This composite was formed by comparing shipboard measurements of GRAPE, magnetic susceptibility, and percent reflectance (from the automated color analyzer) at adjacent holes. These comparisons were then integrated to form a single composite depth section for the site (a detailed discussion on the construction of composite sections during Leg 138 is presented in Hagelberg et al., this volume).

For the holes and cores listed in Column 1 of Table 7, Column 2 gives the ODP sub-bottom depth of the core's top and bottom in meters below seafloor (mbsf). Column 3 shows the length of core recovered. Column 4 gives the composite depth of the core's top and bottom (in meters composite depth, or mcd). Column 5 indicates the amount of offset between the ODP and composite depths. Conversion from ODP sub-bottom to composite depths was done by adding the offset listed in Column 5 for a given core.

GRAPE density and percent reflectance data both produced records with high amplitudes and variability through Holes 847A (1 core), 847B, 847C, and 847D. Although the large-scale (5–10 m scale) features in these three records are similar, smaller-scale (order of 1 m) features that are not similar between GRAPE and reflectance data allow a fairly detailed correlation to be made. Magnetic susceptibility at this site was generally of low amplitude, but because of its very different character from the GRAPE and reflectance data records, it was also a useful tool for hole to hole correlation (Fig. 19, back pocket).

Analysis of the composite section for Site 847 (Fig. 19, back pocket) indicates continuous recovery with overlap down to approximately 175 mcd in the XCB-cored interval (between Cores 847B-17X and 847C-17X). Below 175 mcd, overlap between cores in the two holes does not continue, but the correlation between Holes 847B and 847C is excellent. In this interval, Hole 847B was held fixed and the depth of cores in Hole 847C were adjusted to match the Hole 847B records for the Composite Depth Section. In the APC-cored and XCB-cored interval down to 175 mcd, the GRAPE, reflectance, and susceptibility records are consistent with one another, indicating excellent agreement between holes.

Developing a satisfactory sedimentation rate record for Site 847 was hampered by the absence of a paleomagnetic record. However, all four microfossil groups provided good biostratigraphic information in different parts of the record. Table 8 gives the control points selected to generate the age-depth plots shown in Figure 20.

Control points were selected as shown in Table 8 (in all cases the details may be found in the biostratigraphy section, this chapter). In the lowest part of the section, a diatom and a radiolarian datum were used to supplement the nannofossil datums. Figure 20 shows the age-depth relationship selected, compared with the limits of the datums provided by the four microfossil groups. To first order, agreement between the datums is excellent.

Sedimentation rates are presented vs. age and depth (mcd) in Figures 21 and 22, respectively. Sedimentation rates are relatively high (around 30 m/m.y.) through the entire section except during the lower Pliocene where the sedimentation rate appears to have been about twice as high. It is clear that there must have been a high sedimentation rate at some time or times in the lower Pliocene and/or late Miocene, but biostratigraphic controls do not have sufficient temporal resolution to constrain possible bursts of sedimentation. Thus Figures 21 and 22 must be used with caution. Tuning to astronomical cycles is the only tool available that might resolve the question of the time scale over which sedimentation rate varied at Site 847.

INORGANIC GEOCHEMISTRY

Eleven interstitial-water samples were collected at Site 847, three from Hole 847A at depths ranging from 1.5 to 7.4 mbsf and eight from Hole 847B at depths ranging from 25.0 to 221.5 mbsf (Table 9). Results from these two holes are considered to constitute a single depth profile in this report. Three interstitial-water samples were taken from the solitary core making up Hole 847A. Sediments in this core consisted of olive gray clayey diatom foraminifer nannofossil ooze of Pleistocene age (see "Lithostratigraphy" section, this chapter). Interstitial-water sampling in Hole 847B began with a sample from the last full section of the third core (Sample 138-847B-3H-6). The sediments in this core are late Pliocene in age and consist of interbedded light gray foraminifer diatom nannofossil ooze with radiolarians and olive gray to olive foraminifer nannofossil diatom ooze with clay. The deepest two interstitial-water samples from this site (138-847B-21X-6 and -24X-6) were squeezed from the upper Miocene radiolarian diatom nannofossil oozes that characterize the bottom of this hole (see "Lithostratigraphy" section, this chapter).

Coring in Hole 847B ended at 241.5 mbsf with Core 847B-27X-1, which recovered 15 cm of dark gray to black chert. The chert layer at the bottom of this hole shows up as a large positive anomaly in the "Si yield" channel from the geochemistry log (see "Downhole Measurements" section, this chapter). The top of this chert layer is about 50 m above basement, as estimated from the seismic survey.

Chemical gradients at this site (Table 9) are governed by diagenesis, recrystallization, and the diffusive influence of basalt alteration

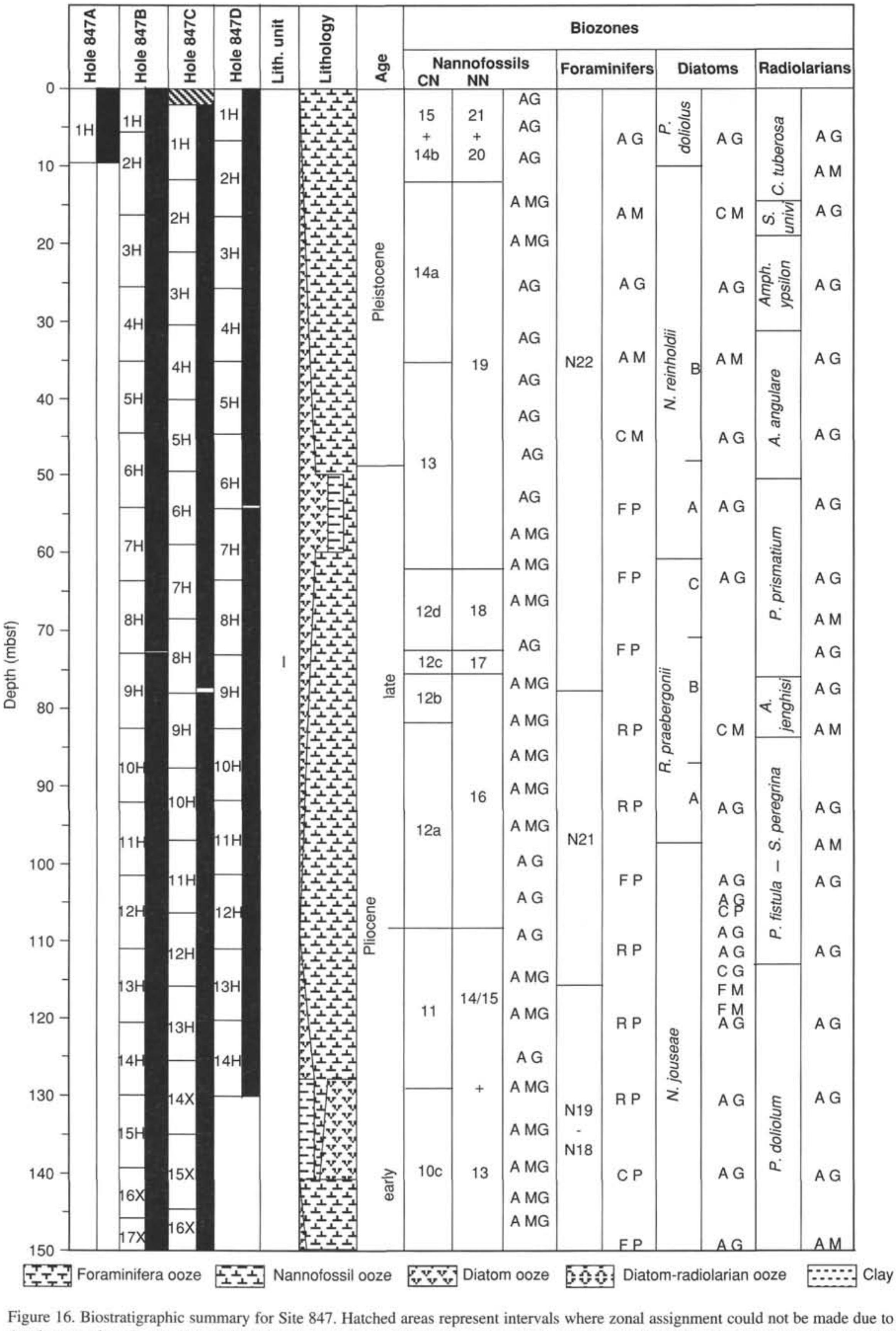

Figure 16. Biostratigraphic summary for Site 847. Hatched areas represent intervals where zonal assignment could not be made due to the absence of marker species. Dashed lines represents uncertainty in placement of a zonal boundary. Microfossil abundance is recorded as: A = Abundant; C = Common; F = Few; R = Rare; B = Barren. Microfossil preservation is recorded as: G = Good; M = Moderate; MG = Moderate to Good; P = Poor. This figure is intended as a general overview of the biostratigraphic results at Site 847. The data presented in the figure are based on results from Hole 847B. Placement of specific stratigraphic boundaries may differ slightly between Holes 847B, 847C, and 847D.

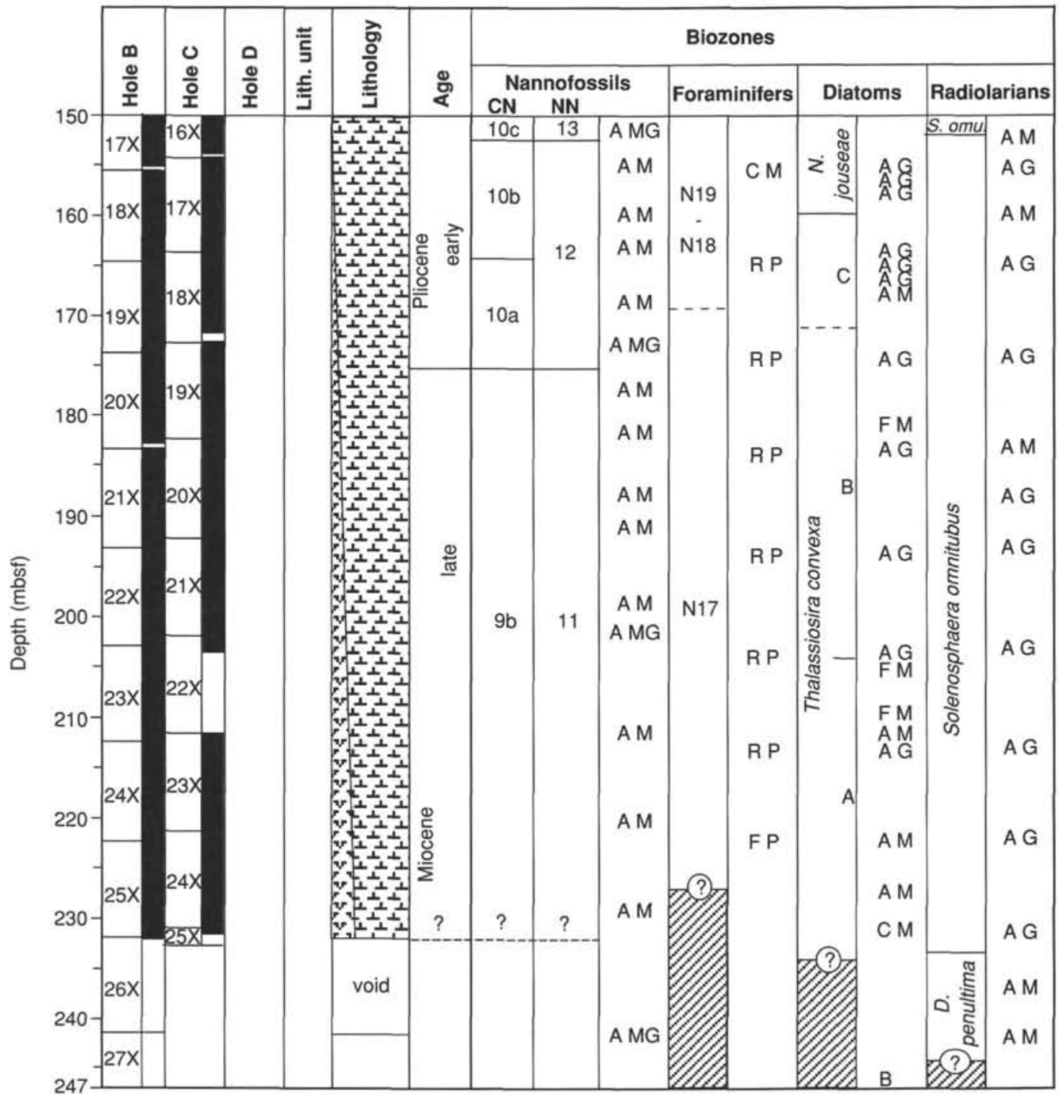

Figure 16 (continued).

reactions in basement rocks. Unlike the three previous sites drilled on this leg, however, many of the profiles from Site 847 are dominated by trends that originate at the bottom of the hole.

Sodium (Fig. 23A) and chloride (Fig. 23B) systematically increase by 2% within the top 50 m of sediment. While quite small, the change in chloride is five-fold larger than the precision of the titration method. Variations in sodium and chloride are unusual in sediments not affected by extensive diagenesis, especially at these shallow sediment depths. The shapes of these concentration-depth profiles coupled withthe observation that there is a relatively high geothermal gradient associated with this site (see "Downhole Measurements" section, this chapter) suggests that upward advection of fluids is affecting the interstitial water chemistry at Site 847.

The noticeable smell of H_2S that characterized Site 846 was absent in cores from Site 847. This contrast in reductive intensity is consistent with other diagenetic indicators: alkalinity, sulfate, and ammonia.

The alkalinity levels at Site 847 (Fig. 23C) are only moderately high for interstitial waters from this leg. What distinguishes the alkalinity data from this site is the unusual concentration-depth profile (Fig. 23C). Alkalinity is generated in sediments during the process of organic matter degradation by microbes (Claypool and Kaplan, 1974). Alkalinities in truly reducing sediments (i.e., zero sulfate) can reach concentrations that are 10-fold higher than the levels found at this site, such as those sampled by Harrison et al. (1982) at Sites 496 and 497 on the Middle America Trench slope during DSDP Leg 67. Since alkalinity production is related to organic matter degradation, alkalinity profiles usually show maxima relatively near the sediment/water interface where labile organics are broken down. Alkalinity levels at this site do not display this typical downhole pattern but instead show a rather diffuse pattern, with increasing concentrations to nearly 200 mbsf. This alkalinity profile cannot be explained by invoking diagenesis alone.

The profile of sulfate with depth (Fig. 23D) is essentially the mirror-image of alkalinity. Below Sample 847B-3H-6 (25.0 mbsf), sulfate decreases almost linearly down to basement. Ammonia variations with depth at this site (Fig. 24C) are consistent with profiles for alkalinity and sulfate. Again, none of these profiles fit a typical picture of diagenesis and diffusion.

Magnesium (Fig. 25A) and potassium (Fig. 25C) decrease downhole at this site. The overall change is 7% and 11% for magnesium and potassium, respectively. While these changes are not large, they are well within our analytical capabilities. Moreover, if one assumes that these profiles are sustained by reaction deep in the basement, then the real change within the sediment column is actually greater since the deepest sample recovered at this site is still 50 m above basement.

The calcium profile (Fig. 25B) does not show the deep, broad concentration maximum which characterized Sites 844 and 845, nor

Table 7. Depths of top and bottom of each core in composite depth section of Site 847.

Hole, core	ODP depth (mbsf)	Core length (m)	Composite depth (mcd)	Δ (m)
847A-1H	0.00–9.52	9.52	1.80–11.32	1.80
847B-1H	0.00–6.59	6.59	0.00–6.59	0.00
847B-2H	6.50–16.08	9.58	6.63–16.21	0.13
847B-3H	16.00–26.02	10.02	16.35–26.37	0.35
847B-4H	25.50–35.58	10.08	28.33–38.41	2.83
847B-5H	35.00–45.09	10.09	37.80–47.89	2.80
847B-6H	44.50–54.60	10.10	49.58–59.68	5.08
847B-7H	54.00–64.10	10.10	60.75–70.85	6.75
847B-8H	63.50–72.83	9.33	71.68–81.01	8.18
847B-9H	73.00–83.10	10.10	82.48–92.58	9.48
847B-10H	82.50–92.68	10.18	92.73–102.91	10.23
847B-11H	92.00–101.56	9.56	104.90–114.46	12.90
847B-12H	101.50–111.58	10.08	114.53–124.61	13.03
847B-13H	111.00–121.05	10.05	125.00–135.05	14.00
847B-14H	120.50–130.35	9.85	135.98–145.83	15.48
847B-15H	130.00–139.81	9.81	145.95–155.76	15.95
847B-16X	139.50–148.98	9.48	155.95–165.43	16.45
847B-17X	145.80–155.13	9.33	165.15–174.48	19.35
847B-18X	155.50–165.19	9.69	174.85–184.54	19.35
847B-19X	164.70–174.52	9.82	184.05–193.87	19.35
847B-20X	173.90–183.24	9.34	193.25–202.59	19.35
847B-21X	183.50–193.35	9.85	202.85–212.70	19.35
847B-22X	193.20–202.97	9.77	212.55–222.32	19.35
847B-23X	202.80–212.43	9.63	222.15–231.78	19.35
847B-24X	212.50–222.27	9.77	231.85–241.62	19.35
847B-25X	222.20–232.01	9.81	241.55–251.36	19.35
847B-26X	231.90–232.04	0.14	251.25–251.39	19.35
847B-27X	241.50–241.54	0.04	260.85–260.89	19.35
847C-1H	2.00–11.97	9.97	2.40–12.37	0.40
847C-2H	11.50–21.34	9.84	13.18–23.02	1.68
847C-3H	21.00–31.07	10.07	23.40–33.47	2.40
847C-4H	30.50–40.43	9.93	33.80–43.73	3.30
847C-5H	40.00–50.09	10.09	44.50–54.59	4.50
847C-6H	49.50–59.19	9.69	55.20–64.89	5.70
847C-7H	59.00–69.09	10.09	66.80–76.89	7.80
847C-8H	68.50–77.35	8.85	76.70–85.55	8.20
847C-9H	78.00–88.08	10.08	87.90–97.98	9.90
847C-10H	87.50–97.60	10.10	98.20–108.30	10.70
847C-11H	97.00–107.10	10.10	108.90–119.00	11.90
847C-12H	106.50–116.44	9.94	118.80–128.74	12.30
847C-13H	116.00–126.09	10.09	129.85–139.94	13.85
847C-14X	125.50–134.99	9.49	139.30–148.79	13.80
847C-15X	135.10–144.73	9.63	151.00–160.63	15.90
847C-16X	144.80–154.11	9.31	164.20–173.51	19.40
847C-17X	154.40–164.13	9.73	174.40–184.13	20.00
847C-18X	163.70–172.25	8.55	184.40–192.95	20.70
847C-19X	172.90–182.65	9.75	192.60–202.35	19.70
847C-20X	182.50–192.26	9.76	202.20–211.96	19.70
847C-21X	192.20–201.97	9.77	211.60–221.37	19.40
847C-22X	201.90–202.78	0.88	221.30–222.18	19.40
847C-23X	211.50–221.38	9.88	230.90–240.78	19.40
847C-24X	221.20–230.98	9.78	240.60–250.38	19.40
847C-25X	230.90–231.24	0.34	250.30–250.64	19.40
847D-1H	0.00–6.61	6.61	0.00–6.61	0.00
847D-2H	6.60–16.54	9.94	8.40–18.34	1.80
847D-3H	16.10–25.84	9.74	19.10–28.84	3.00
847D-4H	25.60–35.50	9.90	29.60–39.50	4.00
847D-5H	35.10–44.88	9.78	39.30–49.08	4.20
847D-6H	44.60–53.74	9.14	50.80–59.94	6.20
847D-7H	54.10–63.64	9.54	61.30–70.84	7.20
847D-8H	63.60–73.20	9.60	71.90–81.50	8.30
847D-9H	73.10–83.25	10.15	81.80–91.95	8.70
847D-10H	82.60–92.28	9.68	94.30–103.98	11.70
847D-11H	92.10–102.19	10.09	104.80–114.89	12.70
847D-12H	101.60–111.51	9.91	115.20–125.11	13.60
847D-13H	111.10–121.15	10.05	124.90–134.95	13.80
847D-14H	120.60–130.10	9.50	135.60–145.10	15.00

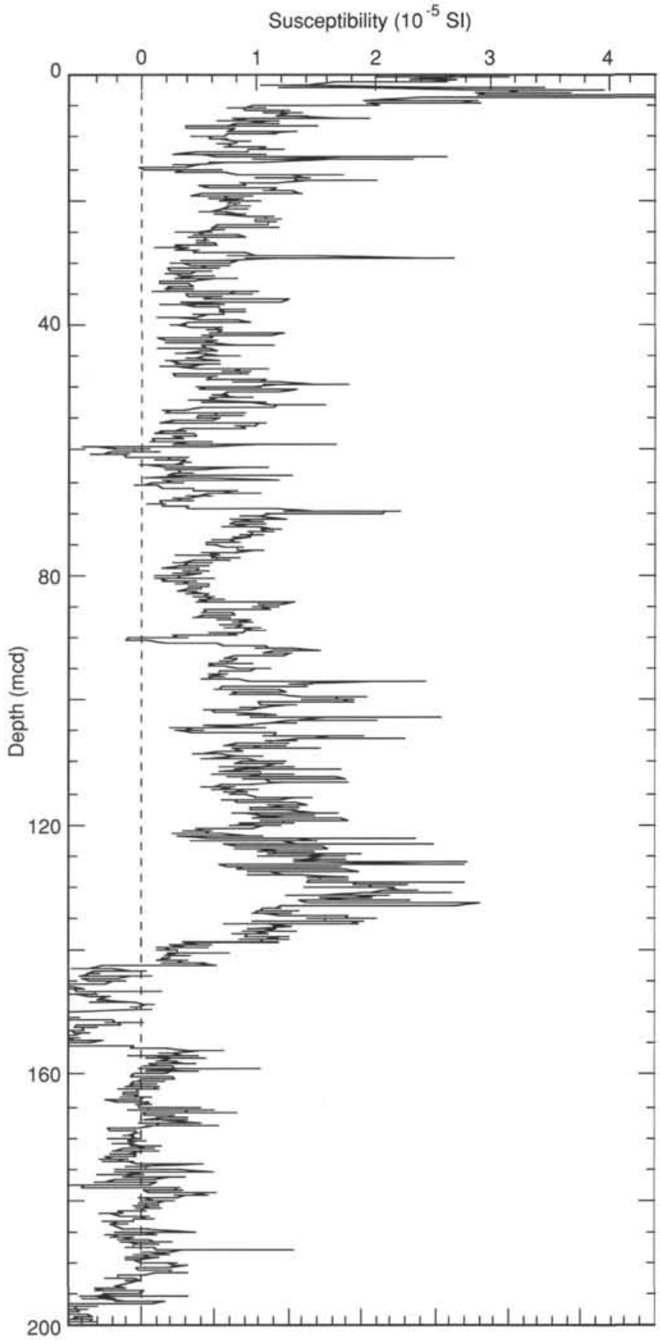

Figure 17. Average susceptibility record obtained at Site 847. Record generated by interpolating values measured in each core and averaging between cores at 5-cm intervals of composite depth. Note the low values between 143 and 155 mcd, which coincide with a diatom-rich interval.

is there any hint of a decreasing trend reminiscent of Site 846. Instead calcium remains constant at a seawater level down through Sample 847B-9H-6. Below 82 mbsf calcium levels rise steadily to the bottom of the hole. This downhole trend is consistent with the release of calcium during recrystallization of calcite below 100 m which is compatible with preservation indices (see "Biostratigraphy" section, this chapter).

Dissolved silica levels at this site (Fig. 25D) are generally high and gradually increase downcore. There is microscopic evidence for recrystallization at this site (see "Biostratigraphy" section, this chapter) and this process may explain why silica increases with depth (Gieskes, 1974). What is surprising about this silica profile is the lack of any anomaly above the chert layer that terminated this hole. Precipitous gradients in interstitial silica are common above chert layers in other holes, notably that observed by Harrison et al. (1982) at Site 495 during DSDP Leg 67. Silica also decreased dramatically above the chert layer at Site 846, but not in this hole. Either the chert here is less reactive or the silica gradient is being obscured by another process; advection is one possibility.

Concentrations of interstitial strontium are known to increase during the recrystallization of calcite (Elderfield and Gieskes, 1982; Gieskes et al., 1986). It is likely that the profile of interstitial strontium at this site (Fig. 24B) is dominated by this process. This analysis is

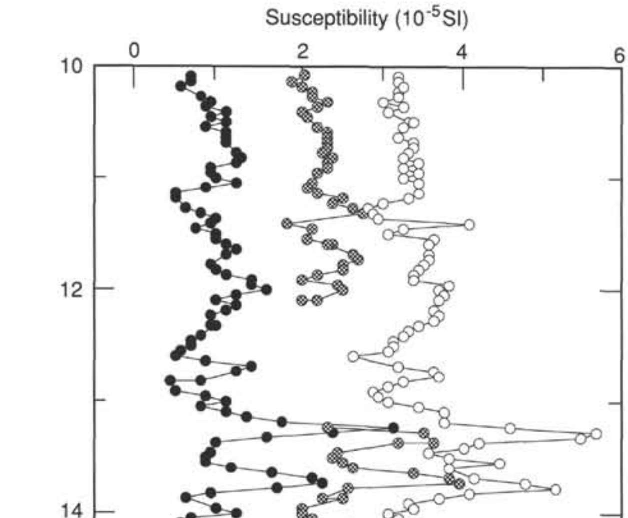

Figure 18. Detail of susceptibility records for 10–20 mcd showing spikes (e.g., near 13 mcd and 16 mcd) that correlate from hole to hole. Hole 847B, solid circles; Hole 847C, darkly shaded circles; Hole 847D, open circles. Results from successive holes are offset 1.26 units for clarity. The apparent data gaps result from repositioning of cores in composite depth.

consistent with microscopic evidence (see "Biostratigraphy" section, this chapter) and supported by the observation that the strontium and calcium profiles in this hole are closely matched, even in detail.

Lithium (Fig. 24A) displays a trend opposite to that for strontium. As at the previous sites, the lithium profile here indicates substantial removal within deeper sections of the sediment column.

In summary, recrystallization and basalt alteration influence the interstitial water chemistry at Site 847. Profiles of the diagenetic indicators, alkalinity (Fig. 23C), sulfate (Fig. 23D), and ammonia (Fig. 24C) seem to be modified by another process at this site, possibly upward advection. The presence of significant advection would be consistent with the relatively large geothermal gradient in this hole and also would explain the convex-upward profiles of sodium and chloride. Calcium (Fig. 25B), silica (Fig. 25D), and strontium (Fig. 24B) indicate that some recrystallization is ongoing at this site, below about 80 mbsf. Alteration of basement rocks are influencing the profiles of magnesium, calcium, potassium, silica, lithium and strontium, to varying degrees.

Table 8. Control points for accumulation rates.

Composite depth (mcd)	Sediment rate (m/m.y.)	Age (Ma)	Remarks
0		0	Core top
	31.8		
14.64		0.461	T *Pseudoemiliania lacunosa*
	37.2		
39.15		1.12	T *Gephyrocapsa* spp. > 5.5 µm
	40.2		
52.43		1.45	T *Calcidiscus mcintyrei*
	39.9		
69.6		1.88	T *Discoaster brouweri*
	32.5		
86.81		2.41	T *Discoaster surculus*
	30.5		
121.88		3.56	T *Reticlofenestra pseudoumbilicus*
	26.5		
143.33		4.37	T *Amaurolithus primus*
	84.1		
194.6		4.98	T *Discoaster quinqueramus*
	34.1		
222.54		5.80	T *Thalassiosira praeconvexa*
	30.1		
243.63		6.50	T *Calocycletta caepa*
	38.7		
251.36		6.70	Upper limit; within the range of *Amaurolithus primus*

T = top occurrence.

ORGANIC GEOCHEMISTRY

Carbonate and Organic Carbon

Concentrations of inorganic carbon were measured in Core 847A-1H and in each section in cores from Hole 847B. From these measurements, we calculated the weight percentages of calcium carbonate (%$CaCO_3$). Total carbon was determined in one sample per core in Hole 847B on the samples taken for headspace gas analysis. The analytical methods are outlined in the "Explanatory Notes" chapter (this volume). The analytical results (reported as means of several measurements, where applicable) are listed in Table 10 (CD ROM, back pocket) with respect to both ODP depth (mbsf) and to composite depth (mcd; see "Sedimentation Rates" section, this chapter). Duplicate %$CaCO_3$ analyses of aliquots from the same sample show that, on average, the values are reproducible to within 0.6% (Table 11). Figure 26 depicts %$CaCO_3$ and %C_{org} in Holes 847A and 847B vs. ODP depth (mbsf). Figure 27 uses composite depth and age assignments (see "Sedimentation Rates" section, this chapter) to show the temporal variability of %$CaCO_3$ and %C_{org}.

Only one lithological unit was recognized at Site 847; it has an average $CaCO_3$ content of 63.6% (range 18.6%–87.9%) and C_{org} concentration of 0.3%.

Accumulation Rates

Following the methodology outlined in the "Explanatory Notes" chapter (this volume), we calculated the average values of several sedimentary parameters in time intervals delimited by the chronostratigraphic levels discussed in the "Sedimentation Rates" section, this chapter. The average values of %$CaCO_3$, %C_{org}, linear sedimentation rate (LSR), dry bulk density (DBD), bulk-sediment mass accumulation rate (bulk MAR), $CaCO_3$ MAR, and C_{org} MAR for 10 intervals since 7 Ma are listed in Table 12. The mean values are presented in Figures 28 and 29. Superimposed on the mean values are estimates of the instantaneous MAR calculated for each sample.

Gas Geochemistry

We took samples for gas analysis from each core of Hole 847B. Gas was released from a sediment sample (about 5 cm^3) by thermal

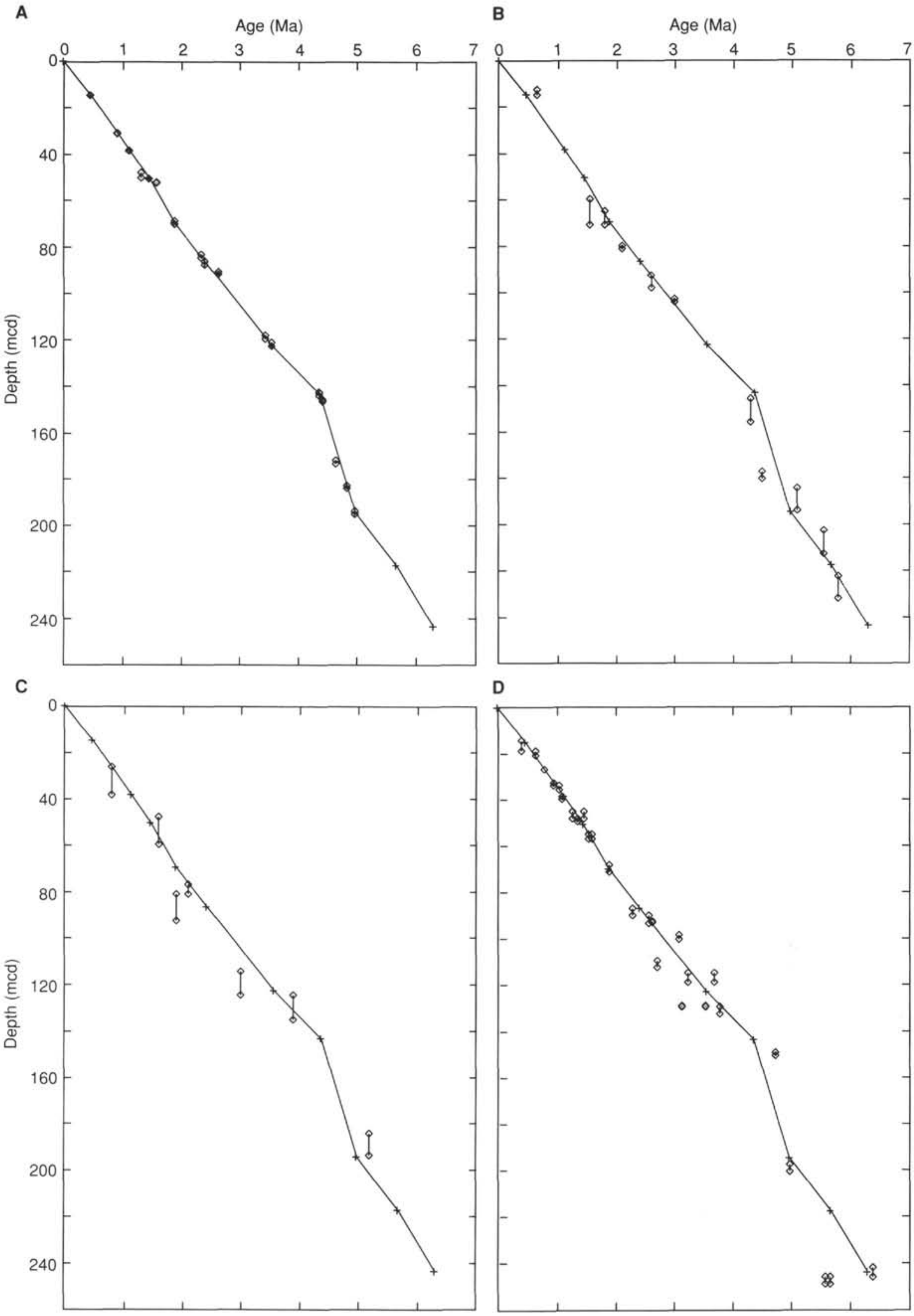

Figure 20. Plot of age vs. depth for Hole 847B based on the calibration points in Table 8 (solid line in each panel), compared with the microfossil datums: (**A**) nannofossils; (**B**) diatoms; (**C**) foraminifers; (**D**) radiolarians. In each panel, the depth range within which each datum was recognized is indicated by two symbols joined by a line; if the line is not visible, the datums are determined to within the size of the symbols.

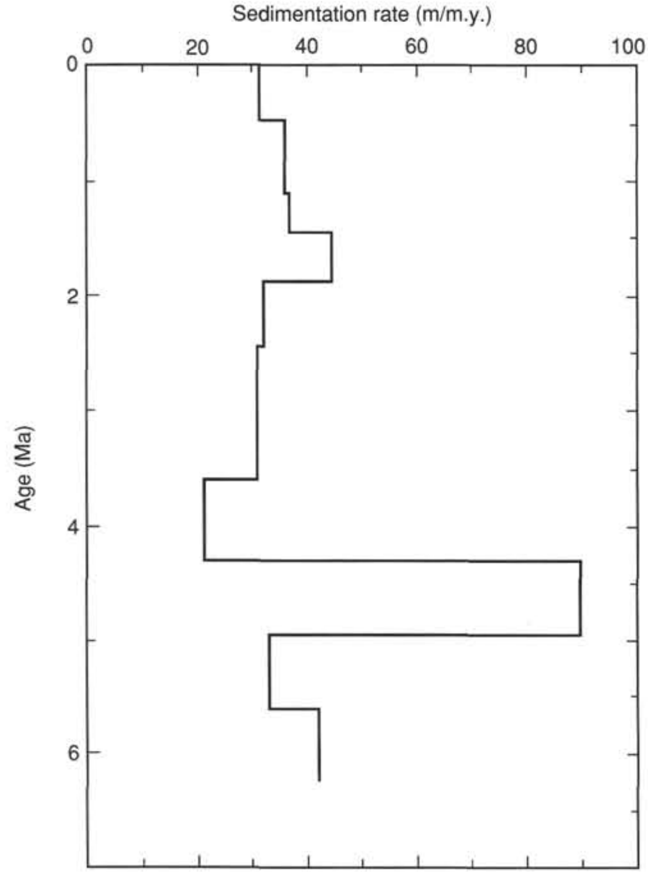

Figure 21. Linear sedimentation rate vs. age based on the data in Table 8.

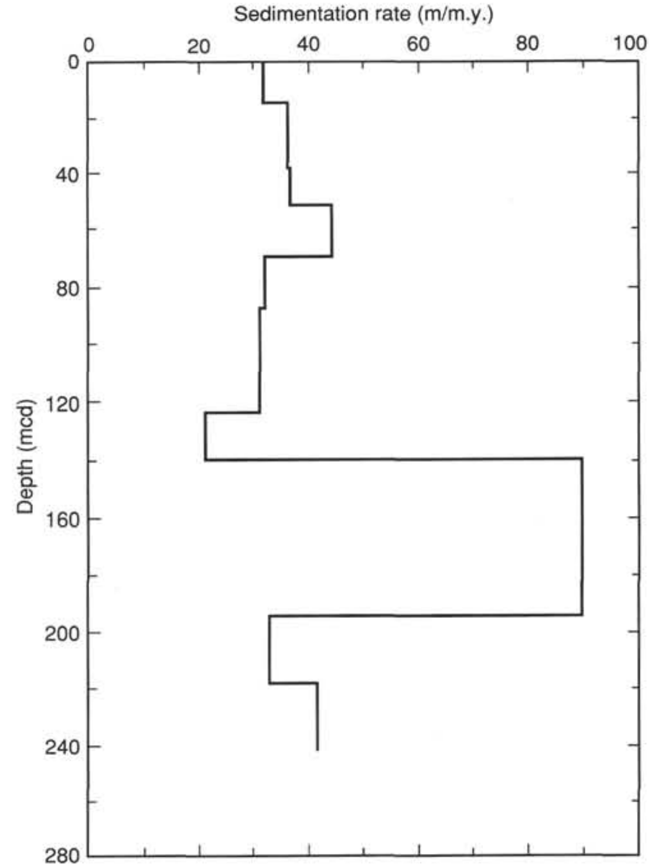

Figure 22. Linear sedimentation rate vs. composite depth based on the data in Table 8.

desorption (see "Explanatory Notes," chapter, this volume) and the measured concentrations of hydrocarbons in the headspace volume (in ppm) were converted to μL/L of sediment and are reported in Table 13. Methane shows an increase with depth in the uppermost 50 m, but concentrations do not exceed 15 μL/L and remain uniformly low from 50 mbsf to the bottom of Hole 847B (Fig. 30). Ethane and higher hydrocarbon gases are below detection limits. A small decrease in interstitial sulfate concentration (see "Inorganic Geochemistry" section, this chapter) corresponds to the observed increase in methane, and both show the inverse relationship previously observed at Site 846. However, the extent of organic matter diagenesis at Site 847 is much smaller than at Site 846.

To evaluate how concentrations of methane depend on the concentrations of organic carbon, C_{org} was measured in the sample splits used for headspace analyses. Because low organic carbon levels and high carbonate concentrations render the results of the "difference method" unreliable, (see "Explanatory Notes," this volume), we adopted a different approach and analyzed total carbon and nitrogen in the dried, carbonate-free residues remaining after carbonate analyses. All results are listed in Table 13. In Figure 30, the concentration of organic carbon in the sediments is compared to the concentration of methane. In general, C_{org} remains low throughout the entire sequence except for the interval from 53 to 63 mbsf, in which values reach about 1% C_{org}. There is no apparent correlation between C_{org} and methane, and we may assume that organic carbon is not a limiting factor for microbial methane formation at Site 847. The concentration of nitrogen is within the expected range in those samples with elevated concentrations of organic carbon, resulting in C/N ratios in the range of 8–10 by weight. In the majority of samples, however, nitrogen is below the detection limit. The low nitrogen content of organic matter may indicate considerable aerobic degradation of organic matter in the water column or in the sediment.

PHYSICAL PROPERTIES

Introduction

Physical properties measured routinely on whole cores recovered at Site 847 include GRAPE-density, compressional-wave velocity (using the multisensor track, MST), and thermal conductivity. For split-cores, index properties such as wet- and dry-bulk densities, water content, porosity, and void ratio were measured in discrete samples. Compressional-wave velocity (using the digital sonic velocimeter, DSV) and vane shear strength also were measured in split cores. The methods of analyses are described in the "Explanatory Notes" chapter (this volume).

Two discrete physical property determinations were carried out on each section of the cores from Hole 847B. Cores from Hole 847C were sampled once per section. Thermal conductivity was routinely determined for two sections (2 and 5) from cores in Hole 847B to a depth of 230 mbsf. No shear strength tests and thermal conductivity determinations were carried out on cores from Hole 847C. Index property samples were always taken at the same depth interval as the velocity measurements. Here, we describe the downhole distribution of the physical properties from Hole 847B because this hole has the highest data resolution. Results of the physical property data determined at Site 847 are summarized in Tables 14 through 17 (CD ROM, back pocket) and illustrated in Figures 31 through 37.

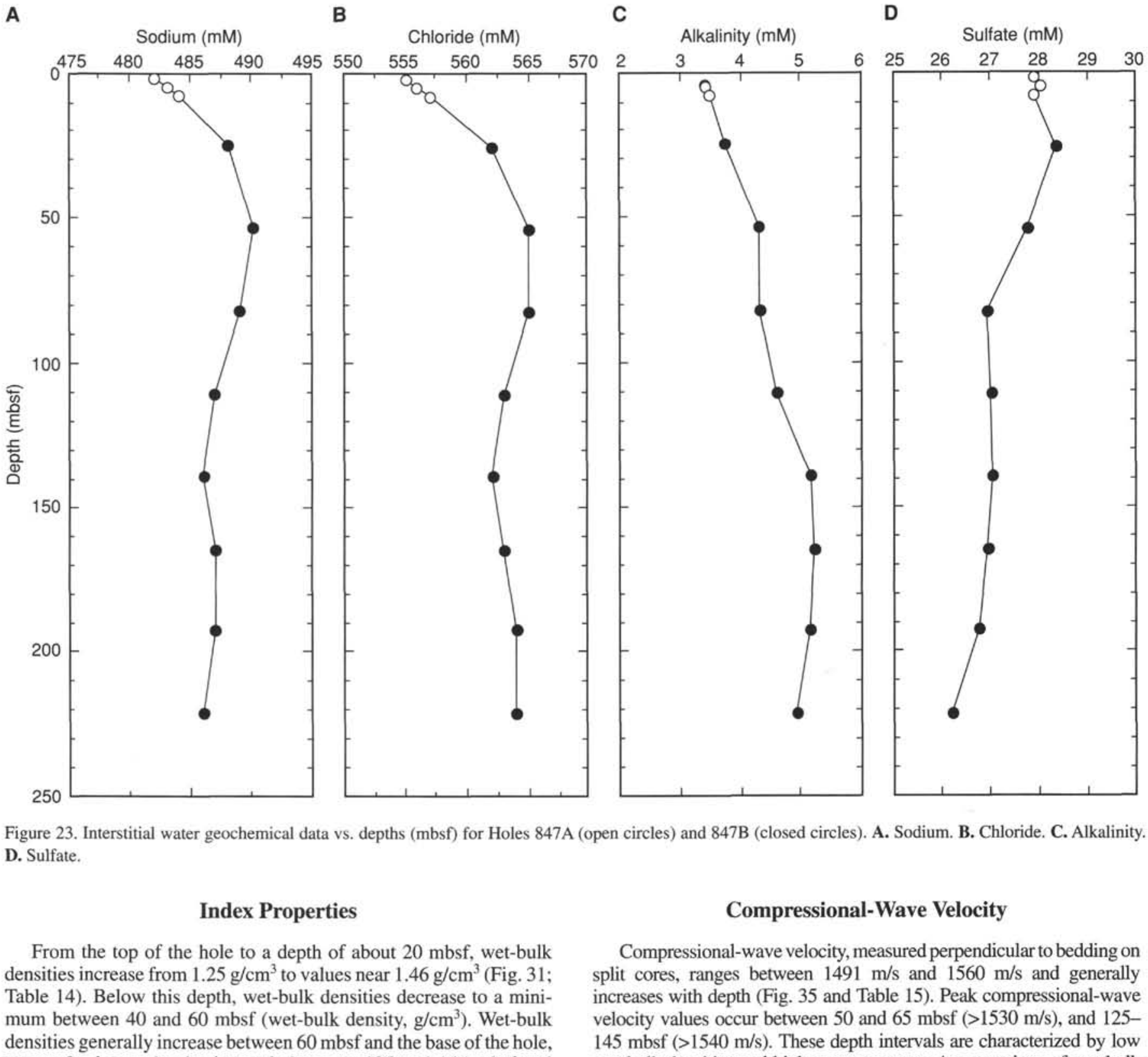

Figure 23. Interstitial water geochemical data vs. depths (mbsf) for Holes 847A (open circles) and 847B (closed circles). **A.** Sodium. **B.** Chloride. **C.** Alkalinity. **D.** Sulfate.

Index Properties

From the top of the hole to a depth of about 20 mbsf, wet-bulk densities increase from 1.25 g/cm^3 to values near 1.46 g/cm^3 (Fig. 31; Table 14). Below this depth, wet-bulk densities decrease to a minimum between 40 and 60 mbsf (wet-bulk density, g/cm^3). Wet-bulk densities generally increase between 60 mbsf and the base of the hole, except for lower density intervals between 125 and 145 mbsf and between 175 and 195 mbsf.

From the top of Hole 847B to about 20 mbsf, water content decreases sharply (Fig. 32; Table 14). Between 40 and 60 mbsf water content increases to values of 300%. Below 60 mbsf water content decreases more or less continuously to the bottom of the hole, except for zones with higher water contents located between 125 and 145 mbsf (water content >150%) and 175 and 195 mbsf (water content >150%).

Porosity (Fig. 33 and Table 14) ranges between 66% and 90% and generally decreases with depth. The downhole variation of porosity shows the same trends as water content.

Grain density (Fig. 34 and Table 14) varies between 2.09 g/cm^3 and 2.83 g/cm^3 with a mean value of 2.54 g/cm^3. No downhole trend is seen in the data. Intervals with low grain densities occur at 40–60 mbsf (grain densities <2.35 g/cm^3), 125 to 145 mbsf (grain densities <2.40 g/cm^3) and 175 and 195 mbsf (grain densities <2.50 g/cm^3). These depth intervals also are characterized by low wet-bulk densities and high water contents.

Compressional-Wave Velocity

Compressional-wave velocity, measured perpendicular to bedding on split cores, ranges between 1491 m/s and 1560 m/s and generally increases with depth (Fig. 35 and Table 15). Peak compressional-wave velocity values occur between 50 and 65 mbsf (>1530 m/s), and 125–145 mbsf (>1540 m/s). These depth intervals are characterized by low wet-bulk densities and high water contents. A comparison of wet-bulk density (Fig. 31) and compressional-wave velocity (Fig. 35) shows an inverse correlation between these two parameters from 0 to 160 mbsf and a positive correlation below 160 mbsf.

Shear Strength

Shear strength values range between 6.8 and 129.6 kPa and increase with depth to 100 mbsf (Fig. 36 and Table 16). Between 100 and 140 mbsf, shear strength values are highly variable. Below 140 mbsf shear strength decreases sharply then generally increases again to the base of the hole. The switch from APC to XCB coring occurred at 140 mbsf.

Thermal Conductivity

Thermal conductivities vary between 0.79 W/(m•K) and 1.25 W/(m•K) with a mean value of 0.98 W/(m•K) (Fig. 37 and Table 17).

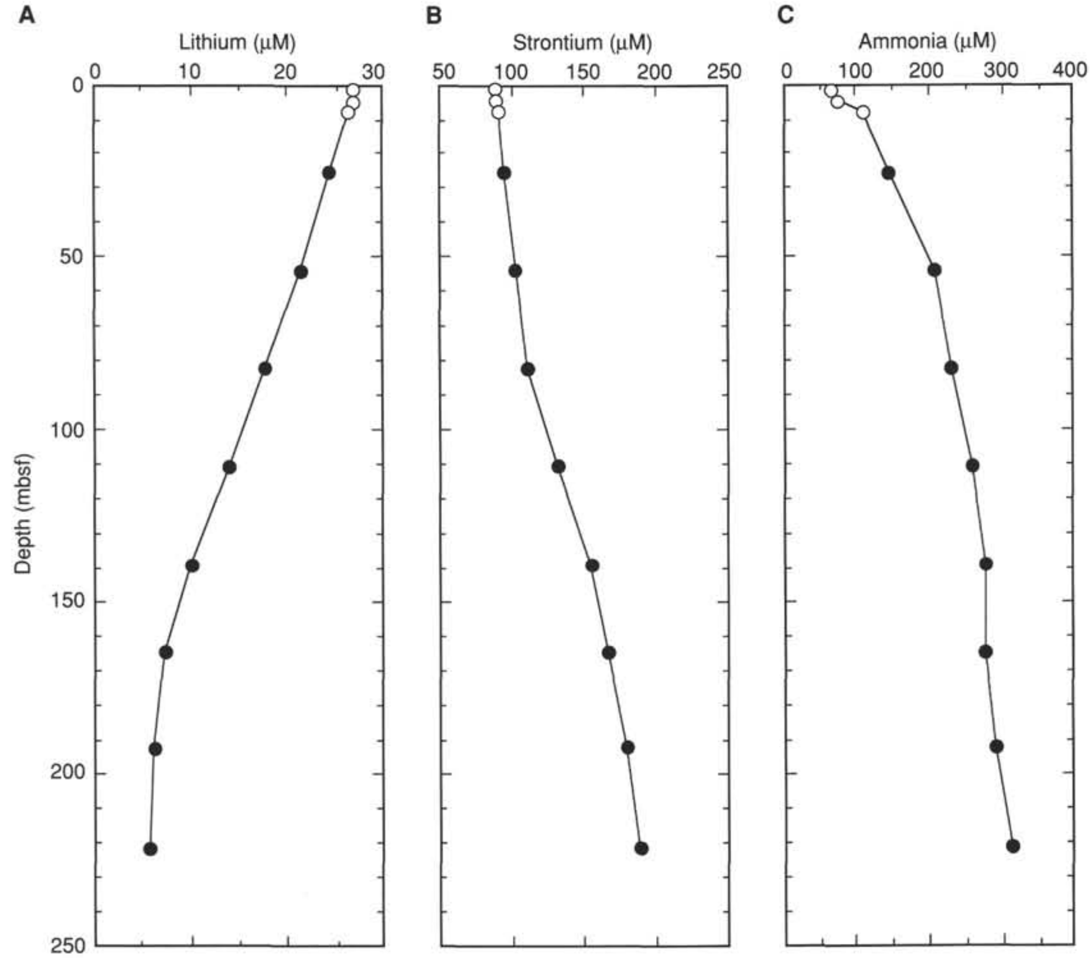

Figure 24. Interstitial water geochemical data vs. depths (mbsf) for Holes 847A (open circles) and 847B (closed circles). **A.** Lithium. **B.** Strontium. **C.** Ammonia.

Table 9. Interstitial-water geochemical data for Hole 847A and 847B.

Hole, core, section, interval (cm)	Depth (mbsf)	pH	Salinity (‰)	Chloride (mM)	Sodium (mM)	Alkalinity (mM)	Sulfate (mM)	Magnesium (mM)	Calcium (mM)	Potassium (mM)	Strontium (µM)	Lithium (µM)	Silica (µM)	Ammonia (µM)
847A														
1H-1, 145–150	1.5	7.39	35.0	555	482	3.165	27.89	54.16	10.48	11.0	86.9	26.6	901	66
1H-3, 135–140	4.4	7.15	35.0	556	483	3.421	28.02	54.00	10.40	10.9	88.2	26.5	965	72
1H-5, 135–140	7.4	7.21	35.5	557	484	3.491	27.88	53.78	10.38	11.0	88.3	26.1	1028	107
847B														
3H-6, 145–150	25.0	7.08	35.8	562	488	3.752	28.33	54.81	10.31	10.4	93.0	24.2	955	146
6H-6, 145–150	53.5	7.15	35.8	565	490	4.315	27.77	54.76	10.45	10.4	101.0	21.1	1075	204
9H-6, 145–150	82.0	7.03	35.8	565	489	4.321	26.95	54.60	10.37	10.3	109.0	17.5	1136	229
12H-6, 145–150	110.5	7.03	35.8	563	487	4.591	27.02	53.75	11.21	10.1	131.0	13.7	1249	256
15H-6, 145–150	139.0	6.95	35.5	562	486	5.155	27.04	53.06	12.06	9.9	154.0	9.9	1455	276
18X-6, 145–150	164.5	6.90	35.5	563	487	5.218	26.93	52.31	12.81	9.8	166.0	7.4	1521	276
21X-6, 140–150	192.5	7.19	35.8	564	487	5.172	26.78	52.18	13.02	9.8	180.0	6.1	1536	287
24X-6, 140–150	221.5	7.00	36.0	564	486	4.919	26.20	51.15	13.89	9.9	188.0	5.8	1640	309

The profile for thermal conductivity generally mirrors the wet-bulk density profile and is inversely related to water content and porosity.

Relationships of Physical Properties to Lithology

The trends in physical property data at Site 847 are controlled by three factors: simple downhole mechanical compaction, diagenesis, and variations in lithology. Gravitational compaction, due to increasing overburden, results in a reduction in water content and porosity (and concomitant increase in wet bulk density) with depth. Shear strength also increases with depth as a result of compaction. The switch from APC to XCB coring, necessary to penetrate the increasingly consolidated sediments, is reflected, in part, by the low shear strength values around 140 mbsf. the first few XCB cores often are more disturbed by the drilling process than cores deeper in the section.

Superimposed on this general downhole compaction trend are fluctuations related to changes in lithology. The sediments at Site 847 consists of alternations between nannofossil ooze and diatomaceous ooze. A comparison of physical properties with lithology reveals that low wet-bulk densities and grain densities and high water contents and porosities at 40 to 60 mbsf, 125 to 145 mbsf, and 175 to 195 mbsf correspond to changes in lithology from nannofossil ooze to diatom ooze. The high shear strength values and high compressional-wave velocities at 125 to 140 mbsf also reflect the higher concentrations of siliceous microfossils.

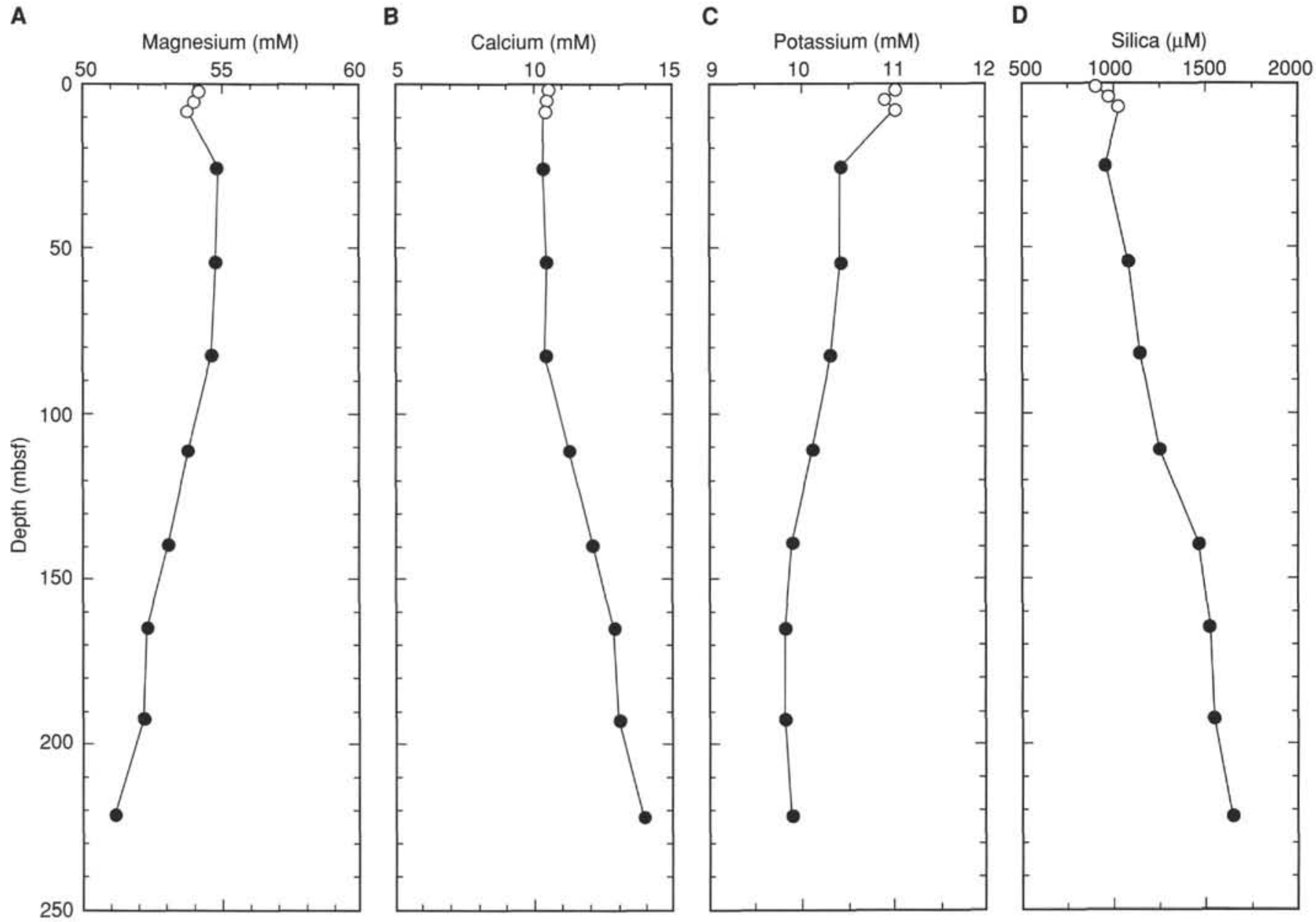

Figure 25. Interstitial water geochemical data vs. depths (mbsf) for Holes 847A (open circles) and 847B (closed circles). **A.** Magnesium. **B.** Calcium. **C.** Potassium. **D.** Silica.

The interlocking structure of the siliceous tests support a higher porosity at depth than carbonate ooze. Thermal conductivity also mirrors the changes in lithology at those depth intervals.

DOWNHOLE MEASUREMENTS

Quality of Data

Geophysical and geochemical logs at Site 847 are very good. Comparison with laboratory density measurements indicate that no drop-outs are present in the density log. Four intervals of low long-spaced velocity measurements (<1.5 km/s) are present at about 60–70 mbsf. Three of the four coincide with low resistivity values. In addition, all short-spaced velocity measurements in this interval are low. We attribute these anomalously low values to poor hole conditions that may be related to the relatively large diameter borehole near the base of the pipe. Correlations between natural gamma-ray measurements obtained during runs of the three tool strings are good, facilitating comparison of the three logs on the same depth scale. Geophysical logs were shifted downward by 0.86 m and the geochemical logs upward by 1.23 m to match the depth of the FMS log. Correlations between FMS data and geophysical tool string resistivity measurements in chert layers near the base of the borehole (see below), however, suggest that slight offsets may be present near the bottom and that the depth measurements are not completely accurate.

Because of electrical problems that developed in the connection between the cable and tool head during the initial run of the FMS tool, only one pass was made. Although no overlap is available, the entire open-hole section was measured during the one run. The large diameter of the borehole shallower than approximately 140 mbsf resulted in degraded images because of lack of contact of two of the FMS pads with the borehole wall. Below 140 mbsf, image quality was good. A short interval from 75 to approximately 90 mbsf was also small enough in diameter to produce good four-pad data. Depth ranges of the usable logs run at Site 847 are listed in Table 18.

Logging Units

At Site 847, we chose to divide the downhole profiles of the logging data into two log stratigraphic units based primarily on changes in the character of the density, resistivity, and velocity logs. Sediment properties in log stratigraphic Units 1 and 2 differ, both in trends of the properties with depth, and in inter-property relationships. Log stratigraphic Units 1 and 2 are separated by a 33-m-thick interval, in which most of the major changes take place. Because changes in the different properties do not occur at the same depths (i.e., synchronously), we identify the interval between the two distinctly different units as a transition zone.

Log Stratigraphic Unit 1 (53–138.1 mbsf: <4.5 Ma)

Log stratigraphic Unit 1 is characterized by low velocity values that increase slightly with depth (Table 19; Fig. 38). Density and

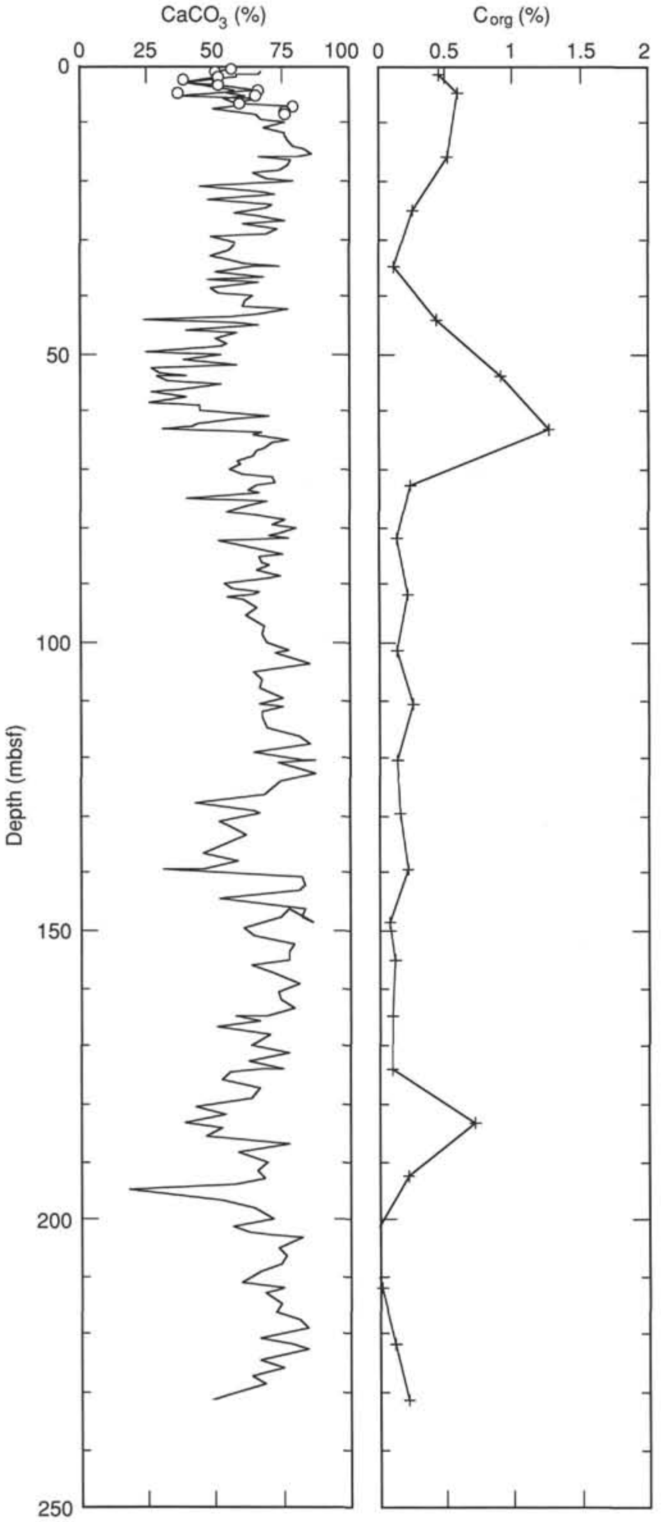

Figure 26. Downhole records of percentages of $CaCO_3$ and C_{org} vs. ODP depth (mbsf) for Hole 847A (open circles) and 847B.

Table 11. Duplicate analyses of $CaCO_3$ in samples from Site 847.

Hole, core, section, interval (cm)	ODP depth (mbsf)	Composite depth (mcd)	First run $CaCO_3$ (%)	Second run $CaCO_3$ (%)	Third run $CaCO_3$ (%)	Absolute value of $CaCO_3$ (difference)
847A-1H-4, 33–35	4.84	4.84	37.00	37.50		0.50
847A-1H-5, 84–86	6.85	6.85	79.59	79.84		0.25
847B-1H-1, 145–150	1.48	1.48	58.75	58.70		0.06
847B-1H-3, 145–150	4.48	4.48	55.17	54.33		0.84
847B-2H-3, 32–34	9.83	9.96	77.01	76.09		0.92
847B-2H-6, 145–150	15.48	15.61	81.76	81.75		0.01
847B-3H-4, 31–33	20.82	21.17	45.75	45.67		0.08
847B-3H-5, 102–104	23.03	23.38	49.17	47.25		1.92
847B-3H-6, 140–145	24.93	25.28	64.34	64.33		0.00
847B-4H-6, 145–150	34.48	37.31	74.84	74.75		0.09
847B-5H-6, 145–150	43.98	46.78	24.84	24.83		0.00
847B-6H-4, 32–34	49.33	54.41	26.59	24.00		2.58
847B-6H-6, 140–145	53.43	58.51	39.59	41.67	40.92	2.08
847B-7H-6, 33–35	61.84	68.59	45.17	43.75		1.42
847B-7H-6, 103–105	62.54	69.29	42.75	41.84		0.92
847B-7H-6, 145–150	62.98	69.73	31.50	32.17		0.66
847B-7H-7, 37–39	63.38	70.13	68.26	68.42		0.17
847B-8H-6, 145–150	72.48	80.66	65.17	66.50	65.92	1.33
847B-9H-2, 26–28	74.77	84.25	40.17	40.25	41.92	1.75
847B-9H-6, 140–145	81.93	91.41	77.51	77.58		0.08
847B-9H-7, 33–35	82.34	91.82	52.59	52.59		0.00
847B-10H-7, 0–5	91.53	101.76	64.67	64.58		0.09
847B-11H-6, 145–150	100.98	113.88	77.67	77.83		0.16
847B-12H-6, 140–145	110.43	123.46	66.26	67.25	67.50	1.25
847B-13H-6, 145–150	119.98	133.98	83.17	83.25		0.08
847B-13H-7, 33–35	120.34	134.34	88.59	87.17		1.42
847B-14H-1, 33–35	120.84	136.32	73.59	74.67		1.08
847B-14H-5, 102–104	127.53	143.01	42.84	43.00		0.17
847B-14H-6, 145–150	129.48	144.96	66.76	66.00	67.00	0.75
847B-15H-6, 145–150	138.98	154.93	46.00	46.33		0.33
847B-15H-7, 33–35	139.34	155.29	31.84	31.75		0.08
847B-16X-4, 33–35	144.34	160.79	51.75	53.50		1.75
847B-16H-6, 145–150	148.48	164.93	87.09	86.92		0.17
847B-17X-2, 32–34	147.63	166.98	75.67	74.92		0.75
847B-17X-6, 145–150	154.78	174.13	77.34	77.50		0.16
847B-18X-6, 140–145	164.43	183.78	70.34	70.25		0.09
847B-19X-6, 145–150	173.68	193.03	75.51	75.33		0.17
847B-20X-6, 145–150	182.88	202.23	40.00	39.58		0.42
847B-21X-6, 140–145	192.43	211.78	68.01	67.08		0.92
847B-22X-2, 13–15	194.84	214.19	18.58	18.58		0.00
847B-22X-6, 145–150	202.18	221.53	63.09	62.75		0.34
847B-24X-6, 140–145	221.43	240.78	79.09	79.42		0.33
847B-25X-6, 145–150	231.18	250.53	49.75	48.67		1.09
					Average	0.63

resistivity values in log Unit 1 display similar trends. Large-scale (approximately 20 m in length) cycles are most obvious in the density log (Fig. 38) and correlate well to laboratory measurements of carbonate content (Fig. 39A).

Log Stratigraphic Unit 2 (170.9–~250 mbsf; 4.92 Ma–>6.3 Ma)

Velocity increases at a higher rate in log Unit 2 than in Unit 1. Fine-scale variability is also higher. Density and resistivity values in Unit 2 are also more variable than in Unit 1 (Table 19) and no large-scale cyclicity is observed. Smaller-scale variations in density, on the order of 1 to 2 m, however, correlate well with carbonate content and Ca-yield variabilities at the same scale (Fig. 39B). Density and velocity variations correlate well in this unit, even on scales of approximately 1 m (Fig. 40), suggesting that velocity is strongly controlled by porosity/density changes in this unit.

Transition Zone (~138–171 mbsf)

Density and resistivity values increase abruptly at the base of log Unit 1 and are high throughout the transition zone (Table 19, Fig. 38). Velocity increases at a level over 6 m deeper than the density increase (about 144.5 mbsf) and displays a much weaker relationship with depth than in either Unit 1 or 2. We chose to separate the transition zone from Units 1 and 2 primarily because of changes observed in trends with depth and in inter-property relationships within this

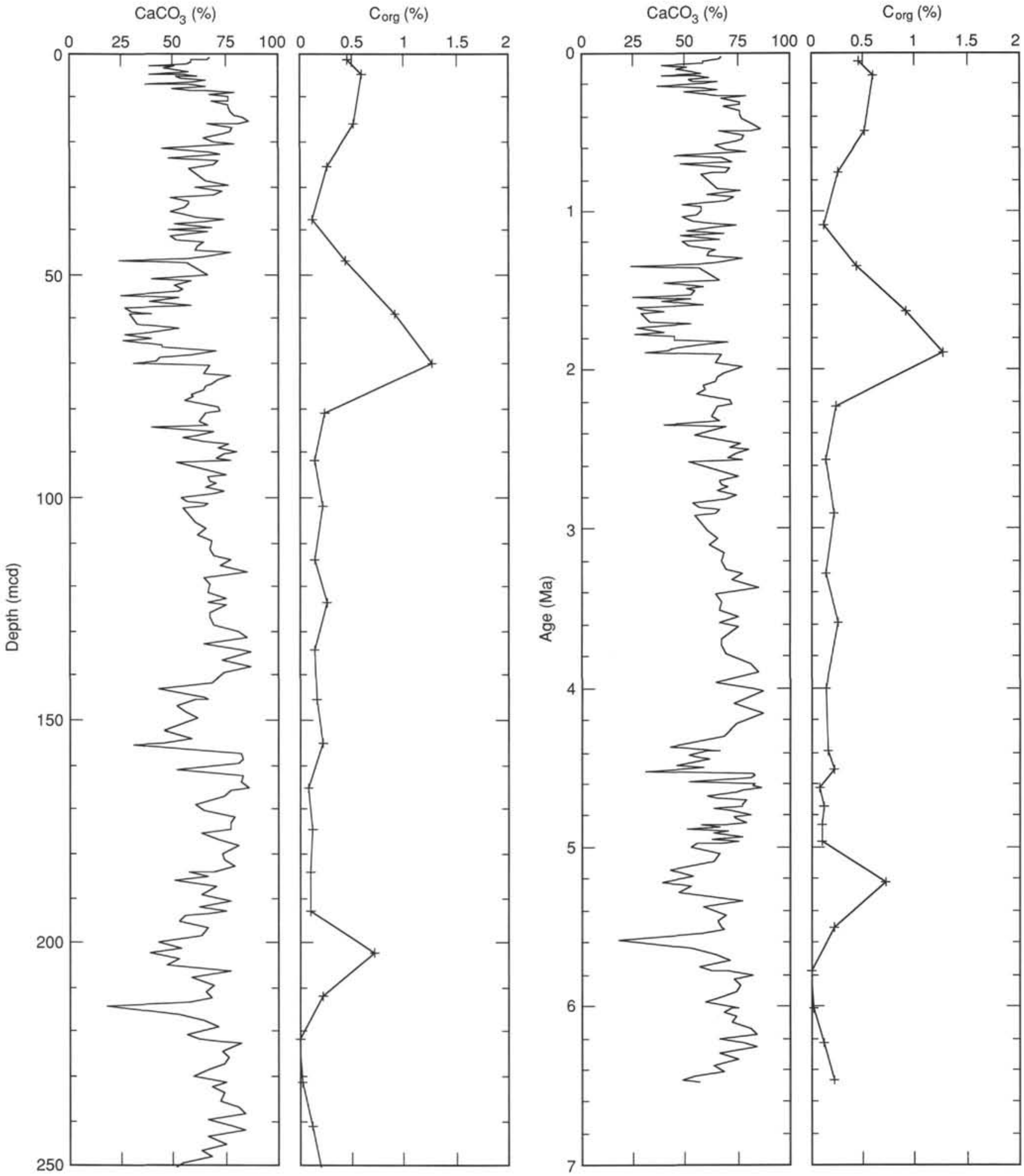

Figure 27. Plots of percentages of $CaCO_3$ and C_{org} vs. composite depth (mcd) and age for Hole 847B.

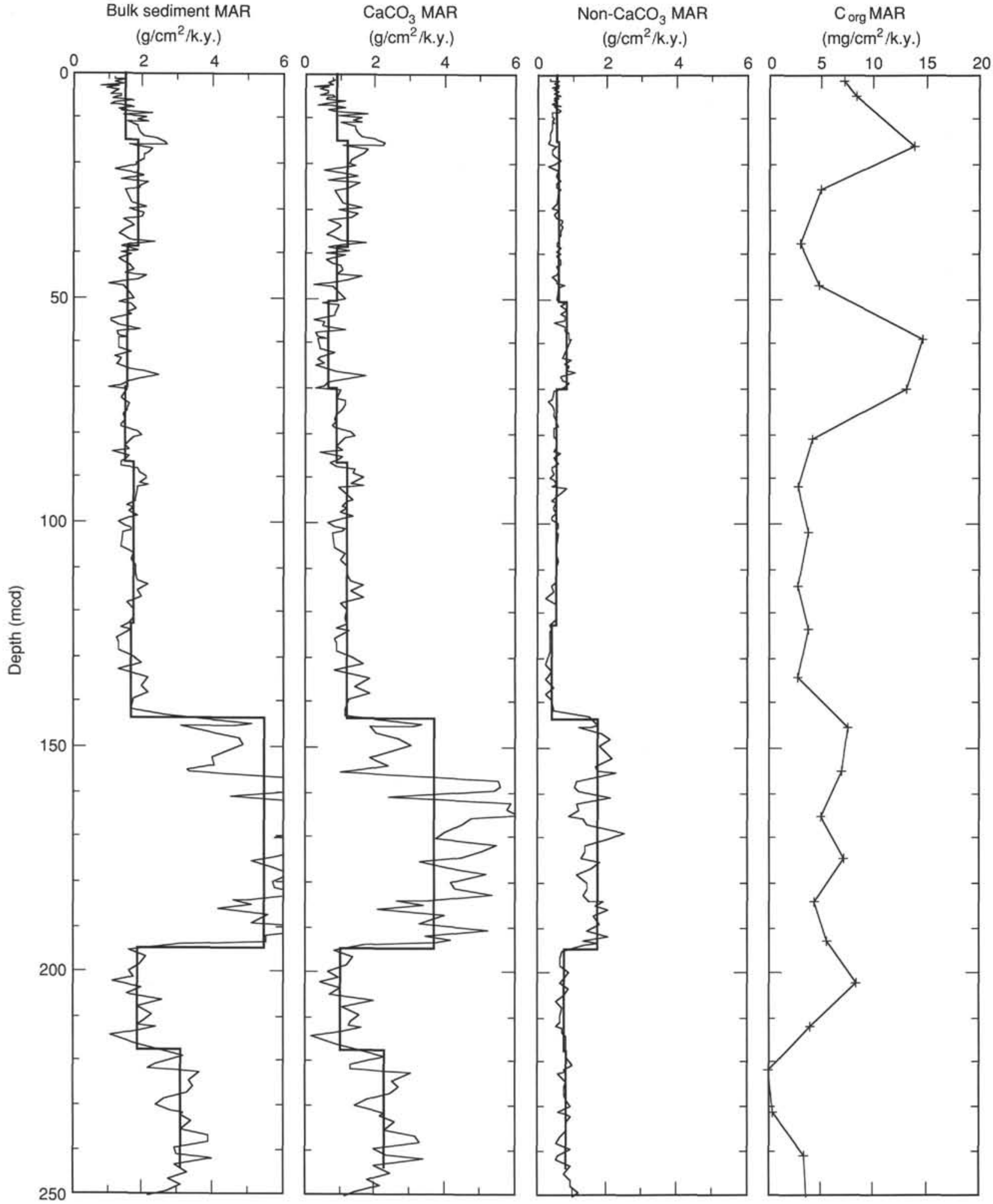

Figure 28. Mass accumulation rates (MAR) of bulk sediment and $CaCO_3$, non-$CaCO_3$ (calculated as 100% minus $\%CaCO_3$), and C_{org} sedimentary components vs. composite depth at Site 847. Note different units for C_{org}. The thick line is the mean value between each stratigraphic datum plane, the thin line shows discrete accumulation rates calculated for each sample.

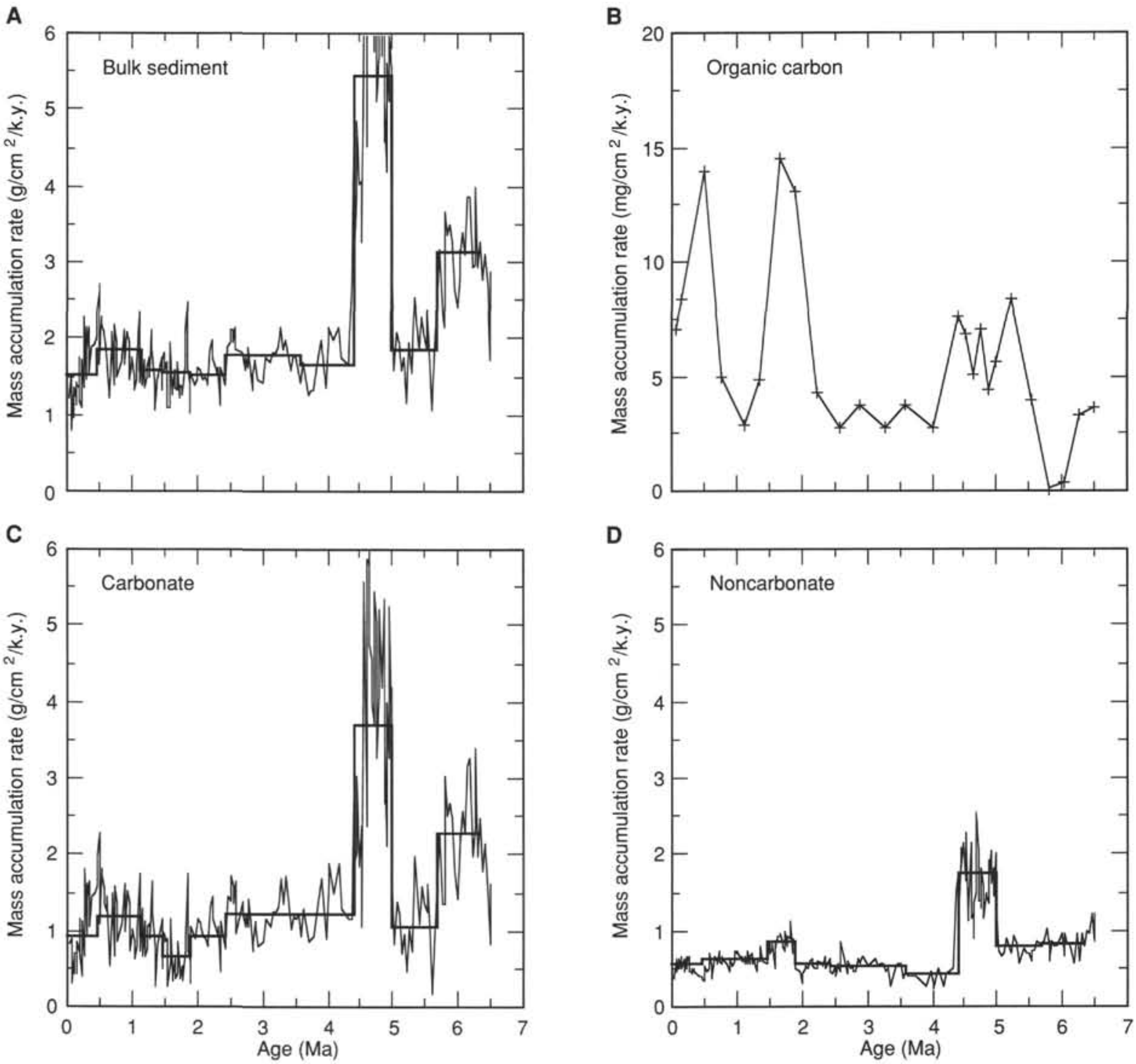

Figure 29. Accumulation rates of (**A**) bulk sediment, (**B**) organic carbon, (**C**) carbonate, and (**D**) noncarbonate (calculated as 100% minus $\%CaCO_3$) vs. age in sediments from Site 847. Thick line is the mean value between each stratigraphic datum plane, the thin line shows discrete accumulation rates calculated for each sample. In **B**, the line has been omitted for clarity.

interval. As at previous sites, the sharp increase in velocity corresponds to the point where the sediments could no longer be penetrated by the APC-coring system. We interpret this recurring phenomenon as evidence of the important role which diagenesis plays in the velocity structure of these sediments.

Controls on Physical Properties

Decreases in porosity and concurrent increases in bulk density resulting from normal sediment consolidation account for most of the velocity increase observed with depth at this site. In Unit 1, large-scale (20 m) variations in density are mirrored in velocity (Fig. 38); both properties increase steadily with depth (Fig. 38). In Unit 2, small-scale variations in density, on the order of 1–2 m, are also reflected in velocity values (Fig. 40). The most significant and abrupt velocity change at 144.5 mbsf, however, is due to an increase in rigidity, rather than a density increase, as indicated by the depth difference of the two transitions and by an abrupt change in the character of the velocity vs. porosity trend at this depth (Fig. 41). The increased rigidity most likely results from cementation of the sediment structure.

Density changes are controlled primarily by lithologic changes as evidenced by good correlations between density and carbonate content (Fig. 39) and Ca-yield values (Fig. 42). At Site 847, lithologic variability results primarily from changes in the concentrations of carbonate and siliceous microfossils although input of terrigenous clay is significant in some intervals (see "Lithostratigraphy" section, this chapter). Thus, the small-scale variability in Unit 2 is presumably due to events of relatively short duration, whereas larger-scale variations in log Unit 1 represent longer-term events. Analogous alternating bands of high and low resistivity, approximately 1–2 m thick are the characteristic features of the FMS log also. This layering corresponds to variations observed in bulk density values and so is also related to changes in carbonate content. Consolidation/compaction of deeper strata has the effect of decreasing the thickness of each layer, exaggerating the difference between the density structure in the two types of sediment. Consolidation also plays a role in density changes

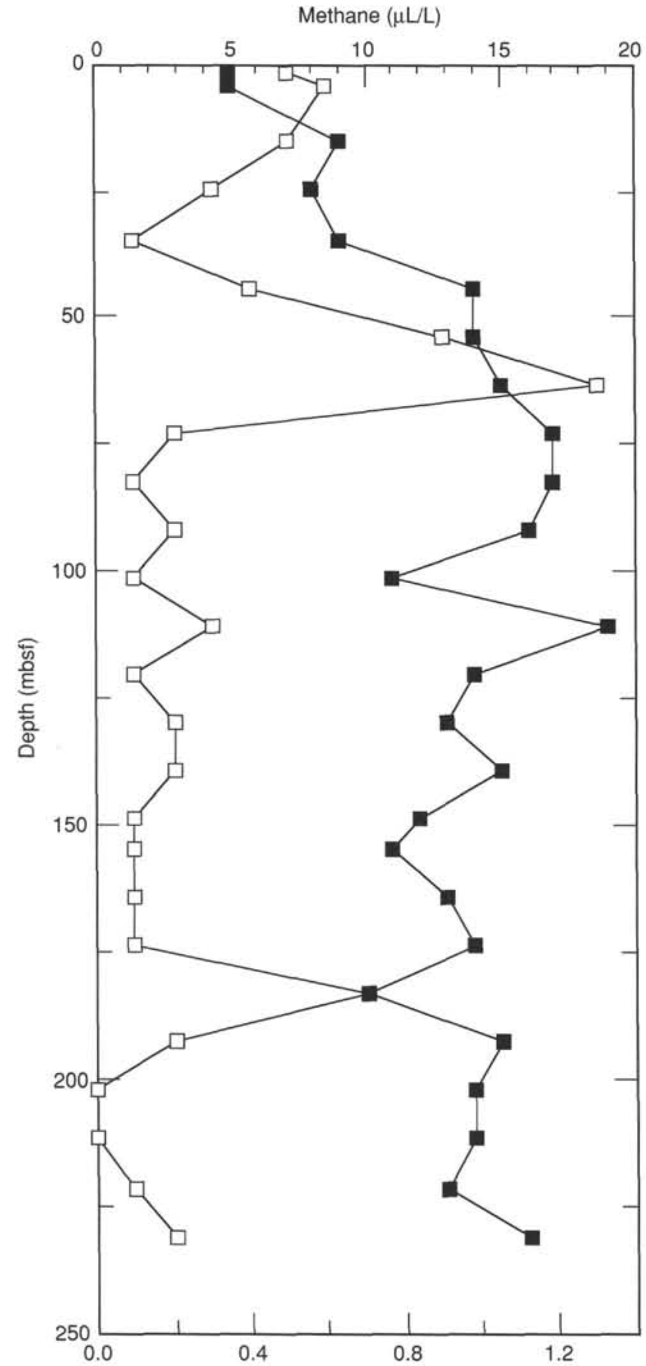

Figure 30. Variation of methane concentration (solid squares) and C_{org} (open squares) vs. depth in Hole 847B.

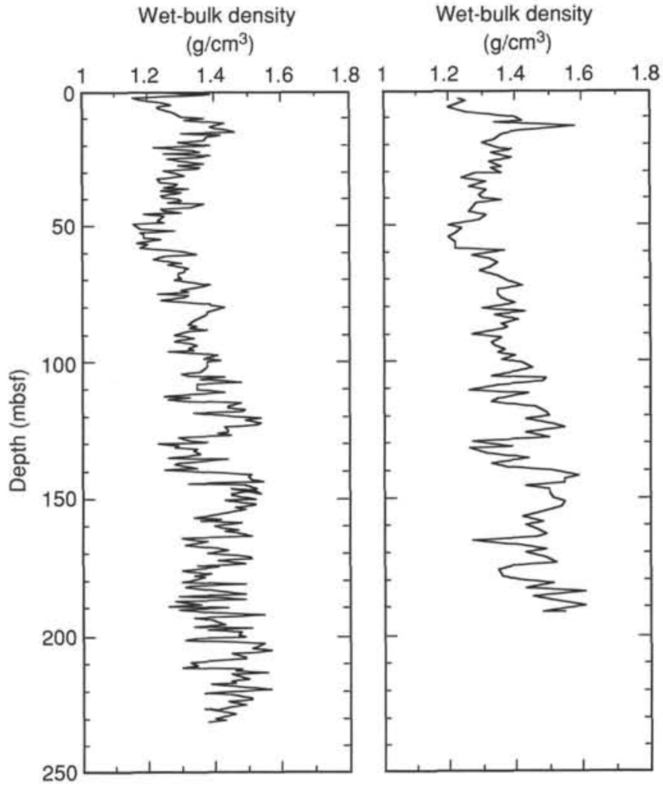

Figure 31. Wet-bulk density vs. depth, Hole 847B (left) and Hole 847C (right).

with depth. Positive correlations between density and depth are observed in Units 1 and 2 and a slight overall trend of increasing bulk density with depth is observed at Site 847. The basic character of the record, however, is one of fine-scale variability, influenced primarily by changes in carbonate content.

We observe anomalous trends in resistivity at this site (Fig. 43). Despite good correlations between small-scale variations in resistivity and density (Fig. 38), resistivity decreases with depth overall (Table 19, Fig. 38). Because both log and lab density and porosity values (see "Physical Properties" section, this chapter) decrease with depth, this resistivity change cannot be caused by higher porosity deeper in the deposit. Changes in interstitial water chemistry are also not great enough (see "Inorganic Geochemistry" section, this chapter) to generate the changes we observe in resistivity. Instead, the increase must be related to changes in pore geometry, specifically, an increase in the "inter-connectiveness" of the pore spaces. In other words, the flow of electrical energy through the fluid phase of the deposit is enhanced in the deeper strata, despite a decrease in the amount of pore volume. One possible cause of this phenomenon is fractures, another is a change in sediment microstructure. For example, a correlation between numbers of high intra-particle porosity foraminifer tests and low conductivity (high resistivity) has been observed elsewhere (Wilkens et al., in press). Although foraminiferal sediments have high porosities, resistivity is anomalously high because much of this porosity is isolated within the tests. A weak positive correlation between resistivity and the concentration of foraminifers (determined from smear slides, "Lithostratigraphy" section, this chapter) suggests that a similar phenomenon may occur at Site 847.

Diagenesis and Chert Formation

Two chert layers in Hole 847B were detected successfully by the FMS tool string (Fig. 44). The shallow layer at 232.9–233.2 mbsf (based on FMS depth measurements) is less than 30 cm thick. It is underlain by material that is far less resistive (higher porosity), which we identify as sediment. At 241.4 mbsf, a second, thicker (>1.5 m) chert layer is observed. This layer is the base of the cored interval in Hole 847B; the upper layer is the bottom of Hole 847C. Chert fragments were recovered in both Holes 847B and 847C, but, without the logging results, the existence of two discrete layers separated by sedimentary strata would have been impossible to confirm. In addition, the thickness of the upper chert bed is well-constrained by the FMS log. The full extent of the deeper layer is still uncertain because its base was not penetrated by the borehole, but its thickness is clearly much greater than what was actually recovered in the core. The caliper

Table 12. Average values of sedimentary parameters measured or calculated over time intervals defined by chronostratigraphic levels.

Composite depth (mcd)	Age (Ma)	Mean $CaCO_3$ (%)	Mean C_{org} (%)	Mean sedimentation rate (m/m.y.)	Mean DBD (g/cm^3)	Mean bulk MAR (g/cm^2/ k.y.)	Mean $CaCO_3$ MAR (g/cm^2 /k.y.)	Mean Non-$CaCO_3$ MAR (g/cm/ k.y.)	Mean C_{org} MAR (mg/cm^2/ k.y.)
0.00	0.00								
		62.36	0.52	31.80	0.48	1.53	0.95	0.57	7.89
14.66	0.46								
		65.84	0.29	36.07	0.52	1.86	1.22	0.64	5.48
38.43	1.12								
		59.05	0.44	36.65	0.44	1.60	0.95	0.66	7.06
50.53	1.45								
		43.71	0.90	44.36	0.35	1.56	0.68	0.88	14.00
69.60	1.88								
		62.81	0.75	32.08	0.48	1.54	0.96	0.57	11.50
86.60	2.41								
		68.80	0.16	31.37	0.57	1.79	1.23	0.56	2.81
122.68	3.56								
		73.38	0.20	25.49	0.66	1.68	1.23	0.45	3.33
143.33	4.37								
		67.85	0.12	84.05	0.65	5.47	3.71	1.76	6.76
194.60	4.98								
		57.03	0.46	32.96	0.57	1.87	1.07	0.80	8.51
217.51	5.68								
		72.87	0.04	41.79	0.75	3.15	2.30	0.86	1.26
243.63	6.30								

Note: DBD: dry bulk density; MAR = mass accumulation rate. After this table was constructed on board the ship, changes were made to the depths of the age control points (see "Sedimentation Rates" section, this chapter, for the final selection of age control points). These depth changes are often minor (less than 5 m). None of these changes have been incorporated in this table nor in the accompanying Figures 28 and 29.

Table 13. Concentrations of total carbon, inorganic carbon, organic carbon, total nitrogen, and total methane vs. ODP depth and composite depth in sediments of Hole 847B.

Hole, core, section, interval (cm)	ODP depth (mbsf)	Composite depth (mcd)	Total carbon (%)	Inorganic carbon (%)	Organic carbon (%)	Total nitrogen (%)	Total methane (%)
847B-1H-1, 145–150	1.48	1.48	7.50	7.0	0.5	0.0	5
847B-1H-3, 145–150	4.48	4.48	7.15	6.6	0.6	0.0	5
847B-2H-6, 145–150	15.48	15.61	10.32	9.8	0.5	0.0	9
847B-3H-6, 140–145	24.93	25.28	7.97	7.7	0.3	0.0	8
847B-4H-6, 145–150	34.48	37.31	9.10	9.0	0.1	0.0	9
847B-5H-6, 145–150	43.98	46.78	3.42	3.0	0.4	0.0	14
847B-6H-6, 140–145	53.43	58.51	5.79	4.9	0.9	0.12	14
847B-7H-6, 145–150	62.98	69.73	5.08	3.8	1.3	0.11	15
847B-8H-6, 145–150	72.48	80.66	8.14	7.9	0.2	0.0	17
847B-9H-6, 140–145	81.93	91.41	9.43	9.3	0.1	0.0	17
847B-10H-7, 0–5	91.53	101.76	7.98	7.8	0.2	0.03	16
847B-11H-6, 145–150	100.98	113.88	9.46	9.3	0.1	0.0	11
847B-12H-6, 140–145	110.43	123.46	8.30	8.0	0.3	0.0	19
847B-13H-6, 145–150	119.98	133.98	10.12	10.0	0.1	0.0	14
847B-14H-6, 145–150	129.48	144.96	8.15	8.0	0.2	0.0	13
847B-15H-6, 145–150	138.98	154.93	5.75	5.5	0.2	0.0	15
847B-16H-6, 145–150	148.48	164.93	10.51	10.4	0.1	0.0	12
847B-17X-6, 145–150	154.78	174.13	9.41	9.3	0.1	0.0	11
847B-18X-6, 140–145	164.43	183.78	8.52	8.4	0.1	0.0	13
847B-19X-6, 145–150	173.68	193.03	9.15	9.0	0.1	0.0	14
847B-20X-6, 145–150	182.88	202.23	5.48	4.8	0.7	0.0	10
847B-21X-6, 140–145	192.43	211.78	8.32	8.1	0.2	0.0	15
847B-22X-6, 145–150	202.18	221.53	7.52	7.5	0.0	0.0	14
847B-23X-6, 145–150	211.78	231.13	9.16	9.2	0.0	0.0	14
847B-24X-6, 140–145	221.43	240.78	9.62	9.5	0.1	0.0	13
847B-25X-6, 145–150	231.18	250.53	6.12	5.9	0.2	0.0	16

Note: Values are from samples used for gas desorption.

record is also useful for identification of the cherts, particularly the shallow bed, showing a distinctly smaller borehole in this very hard, resistive (to coring) material.

The bottom chert layer displays internal structure when examined in detail on the FMS logs. The upper chert does not, but we are uncertain as to whether this is a function of its thickness. Structure in the deeper layer is indicated by resistivity variations within the chert, which probably are caused by porosity variability and the existence of fractures. We also note that the sediment immediately overlying each chert bed has very low resistivity and high porosity values. Sediment underlying the upper chert layer is highly resistive, but resistivity decreases with depth; the material overlying the deeper chert layer also has low resistivity and high porosity values. We suspect that these resistivity/porosity changes, as well as the variability within the deeper chert, are tied to the mechanisms of chert formation and may be related to fluid flow and the character of the original sediment (e.g., type of microfossils present).

No internal structure is seen by the FMS tool within the thinner shallow chert layer, suggesting that this layer is homogenous near the vicinity of the borehole. Geophysical tool string resistivity measurements, however, indicate that this layer is laterally heterogeneous (Table 20). The SFLU, shallow focussed resistivity tool, measures

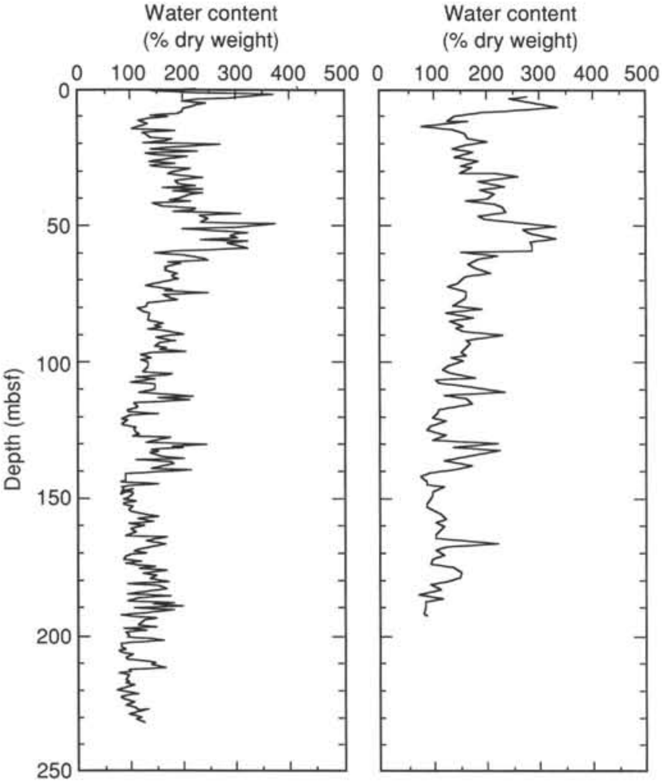

Figure 32. Water content (% dry weight) vs. depth, Hole 847B (left) and Hole 847C (right).

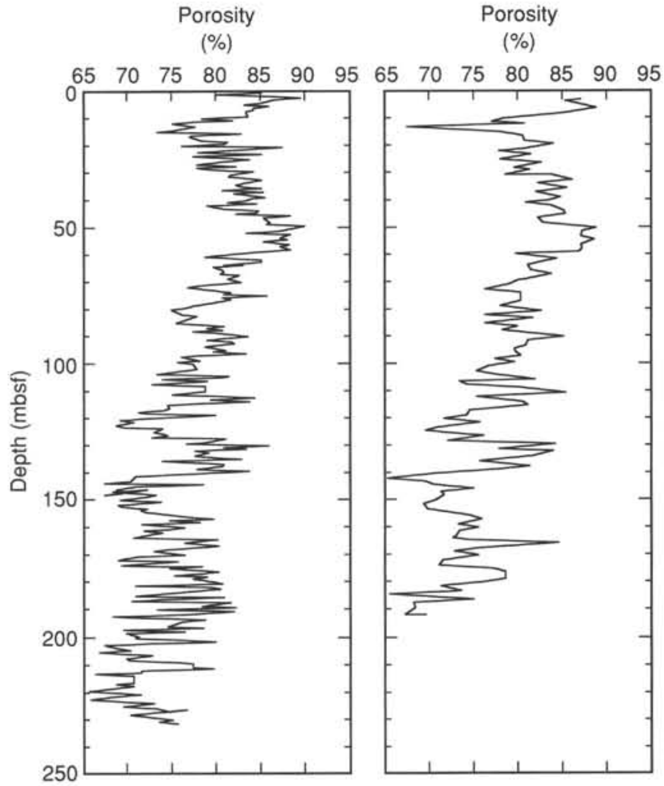

Figure 33. Porosity vs. depth, Hole 847B (left) and Hole 847C (right).

resistivity 41 cm into the deposit; the IMPH, intermediate resistivity tool, averages resistivity over an interval of approximately 70 cm into the formation (Schlumberger, 1989). Figure 45 illustrates the different resistivity measurements obtained by these two tools and suggests that the upper chert layer is less than 1 m thick in lateral continuity in the vicinity of the borehole. The presence of fractures in a more or less continuous layer, rather than nodular chert, is also suggested by the FMS data and by the recovery of an analogous chert bed at the base of Hole 847C.

Measurements of resistivity of the lower chert bed also were made by the resistivity tool. Values of shallow focused (SFLU) resistivity reach a maximum of nearly 10,000 ohm-m (Table 20, Fig. 45) at 240.8 mbsf, indicating an interval of extremely low porosity. Another peak in resistivity 0.9 m shallower indicates vertical heterogeneity in this layer, confirming the presence of internal structure observed in the FMS. Only one resistivity increase is observed in the intermediate resistivity (IMPH) measurement. As is the case in the shallow layer, we interpret this as indicative of the lack of lateral continuity of the bed, probably resulting from the presence of fractures.

The two chert beds at Site 847 were also detected in the geochemical logs. Silica yield increases at 233.7–234 mbsf (upper chert layer), then increases again, abruptly at 243 mbsf, remaining high to the base of the borehole (Fig. 46). Hydrogen yield, which is related to the amount of water in the deposit, and thus the porosity, decreases concurrently with the silica increases (Fig. 46). Similar decreases are observed in CSIG measurements, an estimate of the total capture-cross section. Variations in porosity within the deeper chert bed are indicated by the H-yield measurements; compositional variability is indicated by the changes in Si-yield over this interval.

Comparison with Site 846

Chert was also recovered at Site 846, but much deeper, at approximately 365 mbsf (see "Site 846" chapter, this volume). These two sites have similar depositional histories, sediment types, and sedimentation rates. The much shallower occurrence of chert at Site 847 in much younger sediments (approximately 6.6 Ma at Site 847, 12 Ma at Site 846) may be due to a much higher geothermal gradient and the presence of advection at Site 847. Although no equilibrium temperatures are currently available, we calculated minimum geothermal gradients at Sites 846 and 847 based on temperature measurements from the final tool string run, during which the measured borehole temperature most closely approximates *in-situ* temperatures. Using the maximum temperature measured at the base of the borehole, bottom-water temperature, and assuming a linear gradient, geothermal gradients are 39° C/km at Site 846 and 76° C/km at Site 847. In addition, interstitial-water chemistry suggests the existence of advection at Site 847 (see "Inorganic Geochemistry" section, this chapter) that may be related to the higher geothermal gradient and clearly is involved in the formation of chert at relatively shallow depths at Site 847.

To better compare the data at Sites 846 and 847, we related density logs at the two sites using CORPAC, a nonlinear correlation program (Martinson et al., 1982), by tying distinct features at Site 847 to similar events at Site 846. Density profiles in the depth interval in which Sites 846 and 847 overlap are nearly identical in magnitude, with similar variability. Density values average 1.44 $\pm$0.09 g/cm^3 at Site 847 and 1.48 $\pm$ 0.06 g/cm^3 in the top 240 mbsf at Site 846. The difference between log bulk density values at Site 846 and at Site 847 are less than $\pm$ 0.15 g/cm^3 and do not show any distinct trends with depth (Fig. 47A). Resistivity values at Site 847, however, are significantly less than values at equivalent depths at Site 846 (Fig. 47B). The average difference between intermediate resistivity values at the two sites is 0.194 $\pm$ 0.051 ohm-m and increases slightly with depth. Velocity differences decrease abruptly at approximately 170 mbsf (depth at Site 846; Fig. 47C). Below 170 mbsf, velocities at Site 847 increase sharply relative to those at Site 846 and remain generally higher to the base of Hole 847B (Fig. 47C). This depth marks the point at which lithification in Hole 847B required XCB-drilling. We attribute the higher velocity values at Site 847 to a greater degree of

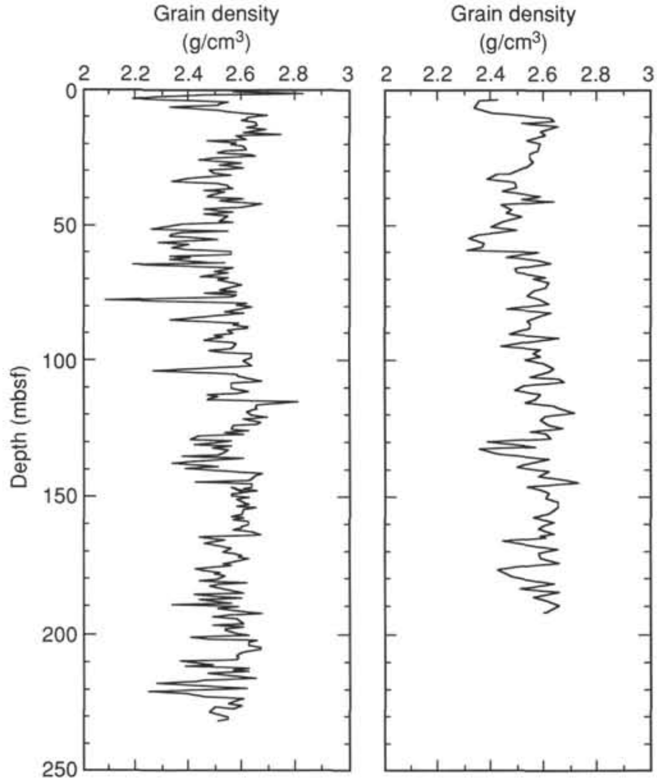

Figure 34. Grain density vs. depth, Hole 847B (left) and Hole 847C (right).

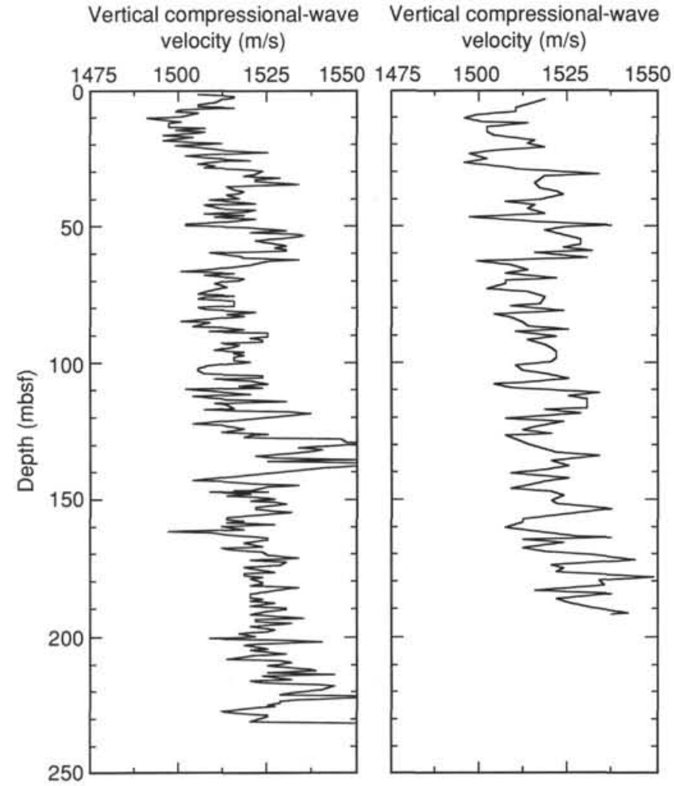

Figure 35. Vertical compressional-wave velocity vs. depth, Hole 847B (left) and Hole 847C (right).

diagenetic recrystallization and cementation of the sediment structure. Enhanced cementation fits into the scenario, suggested above, of hydrothermally-driven pore fluids resulting in early diagenetic changes, but does not explain the consistent patterns of velocity and density observed at Site 847 (Fig. 40). Lithologic changes and consolidation influence density and velocity characteristics at both sites. At Site 847, however, the effects of diagenetic cementation also contribute to velocity variations with depth.

Log to Laboratory Comparisons

Comparisons between log density and density values determined by MST GRAPE measurements are good (Fig. 48). All major events, such as the 20 m cyclicity in log Unit 1 and the higher frequency variability in log Unit 2 are observed in both records. In addition, smaller-scale variations, on the order of 2–3 m, are present in both log and GRAPE data. The offset between the two density datasets decreases with depth. GRAPE measurements in log Unit 1 and the transition zone are slightly higher (0.04 g/cm^3, on average) than log data. Below approximately 200 mbsf, the magnitude of the two measurements are very similar (less than 0.01 g/cm^3 difference; Fig. 48). Densities determined gravimetrically (see "Physical Properties" section, this chapter), however, are lower than log values (Fig. 49). Trends of these two measurements with depth do not compare as well as those in log and GRAPE data, although major features, such as the density increase at the bottom of log Unit 1, are present in the gravimetric record. Differences between log and physical property density values are, on average, slightly less in the transition zone, but no consistent trends with depth are observed (Table 19).

SEISMIC STRATIGRAPHY

Modeling Procedure

Synthetic seismograms were generated from velocity and density models for Site 847 in order to correlate reflectors in the seismic section to stratigraphic changes.

The density model was created by merging laboratory density to *in-situ* logging density. Depth-shifted logging density (by correlation with the Hole 847B GRAPE density) was used over the interval 64.1–231.4 m (64.1–231.1 mbsf) (see "Downhole Measurements" section, this chapter). Over the interval 0–64.1 mbsf, a 10-point boxcar-filtered GRAPE density from Hole 847B was merged with the depth-shifted logging density. Beyond 231.1 mbsf to the depth of coring refusal (247.5 mbsf), a constant density of 1.5 g/cm^3 was used.

The velocity model was created in a similar manner as above. From 52.5 to 226.4 mbsf, depth-shifted log velocity was employed. To fill the gap in the upper part of the section, laboratory velocity collected with the DSV were corrected to *in-situ* conditions for changes of sound speed as a function of temperature and pressure, assuming a temperature gradient of 74.6° C/km and a bottom-water temperature of 1.81° C, as determined from the temperature log. From 226.4 to 247.5 mbsf, a constant velocity equal to the final log velocity (1752 m/s) was used.

The accuracy of the traveltime-to-depth conversion can be evaluated by the generation of synthetic seismograms and the subsequent comparison to the seismic record collected over the site. Synthetic seismograms were generated using the above merged velocity and density data. These data were resampled at a 1-ms sample interval

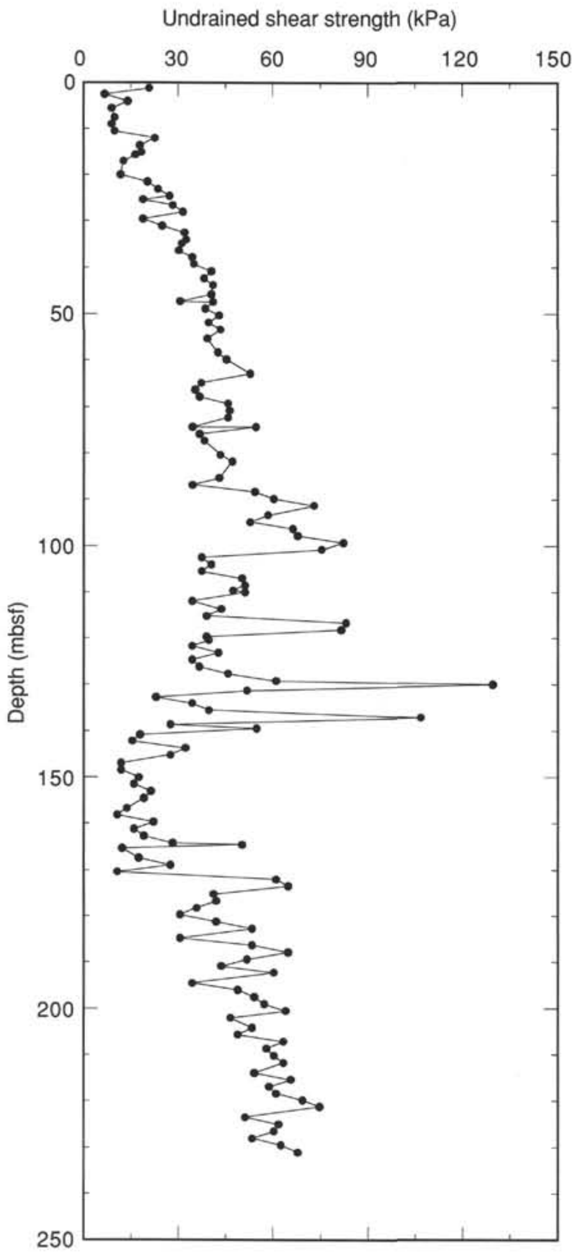

Figure 36. Undrained shear strength vs. depth, Hole 847B.

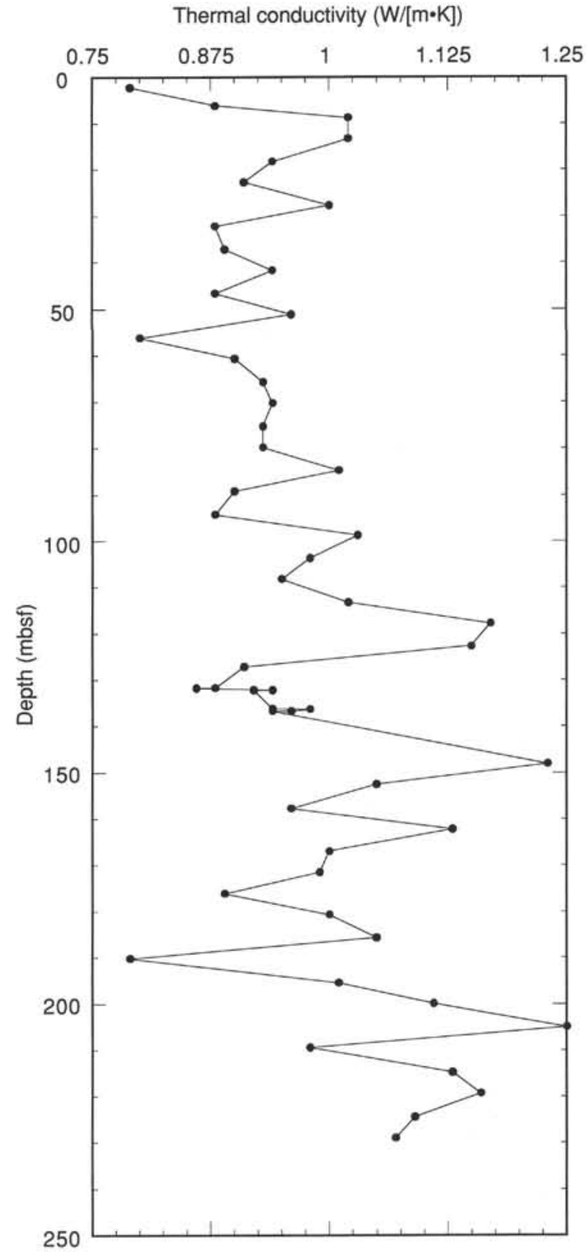

Figure 37. Thermal conductivity vs. depth, Hole 847B.

(approximately 60 cm) and then used to calculate acoustic impedance and reflection coefficients and finally, a synthetic seismogram. Density and velocity values typical of chert (2.0 g/cm^3 and 2500 m/s, respectively) were added at the depth of coring refusal (247.5 mbsf) to generate a chert reflector in the synthetic. The model used to generate the synthetic seismogram assumes plane waves, no multiples, and no signal attenuation; the model is described in Mayer et al. (1985). The final synthetic seismogram was filtered from 70 to 250 Hz, the same filter parameters as the field record collected on the site survey cruise aboard the *Thomas Washington*.

Results

A comparison of the synthetic seismogram with the seismic profile collected at Site 847 shows a good match between the two (Fig. 50). There is an excellent correspondence between major reflectors, although a match between the chert reflector in the synthetic seismogram and the field record is not clear. This agreement suggests that the traveltime-to-depth conversion is fairly accurate.

Given that the velocity model is quite acceptable for all the labeled reflectors, the origin of some of these reflectors can be analyzed. We emphasize that these are preliminary results that will be undoubtedly modified after more careful analysis. Eleven major reflectors or reflector packages were identified. These reflectors were selected on the basis of amplitude and lateral coherency in the seismic record in the immediate area of Site 847. The two-way traveltime on the synthetic of the top and bottom of each reflector was measured, and by using the assumed velocity model, the depth range of each reflector was determined.

The velocity, density, and acoustic impedance models were compared to the depth ranges calculated from the traveltime to determine the changes in physical properties causing the selected seismic reflectors. In general, within each calculated depth range, a large change in density and/or velocity can be associated with each reflector (Fig. 51).

Table 18. Logging data for Hole 847B.

Log type	Depth in Hole 847B (mbsf)
Resistivity	57.4–241.0
Bulk density	64.2–236.9
Sonic velocity	52.7–226.4
Sonic waveforms	52.7–226.4
Gamma ray/U-Th-K	0–243.0
Aluminum	0–240.6
Geochemistry	0–243.0
Caliper	68.7–243.0
Formation microscanner	68.7–243.0
LDGO temperature	0–243.0

Note: Values assume seafloor is at 3346 mbrf (meters below rig floor). A common scale for all logs was obtained by shifting the geophysical logs downward by 0.86 m and the geochemical logs upward by 1.23 m.

For the most part, the reflectors are related to large changes in density. Reflector 9 appears to be caused by the velocity maximum at about 150 mbsf, although there is a small density maximum at about 153 mbsf. Reflectors 14 and 15 are due to synchronous fluctuations in velocity and density, although the amplitude of the density fluctuations are much greater. The depths (synthetic, mbsf, and mcd) and ages (based on magnetostratigraphy and biostratigraphy of Site 847; see "Sedimentation Rates" section, this chapter) of these reflectors are presented in Table 21. A detailed understanding of the lithological, biostratigraphic, and, ultimately, the paleoceanographic significance of these events must await shore-based studies at this time.

SUMMARY AND CONCLUSIONS

Site 847 is located within the equatorial divergence approximately 380 km west of the Galapagos Islands. The surface oceanographic conditions of this region of the equatorial Pacific reflect the interaction of three major oceanic elements: (1) the eastern end of the westward-flowing South Equatorial Current (SEC) (which is also influenced by the cold northward-flowing Peru Current); (2) divergence and upwelling caused by the change in the direction of the Coriolis force at the equator and; (3) the seasonal shoaling of the eastward-flowing sub-surface Equatorial Undercurrent. The site was selected in an effort to extract the late Neogene record of changes in this circulation–changes which may reflect variations in global atmospheric conditions and climate.

In addition to being influenced by a complex surface oceanographic regime, the sediment at Site 847 also reflects the interaction of tectonism and deep-ocean chemistry. Estimates of basement age for the site can be made based on tectonic reconstructions of the eastern Pacific (Hey, 1977; Hey et al., 1977). The site is located near the boundary between crust formed at the Galapagos Spreading Center to the north and the East Pacific Rise to the west of the site. While it is difficult to distinguish from which of the two spreading centers the site originated, it is not critical to paleoceanographic reconstructions because the absolute motion of all crust in the region is dominated by the Pacific-Nazca pole of rotation and thus the site has remained in its present equatorial (and thus oceanographic) setting for most of its history (Table 22). Of greater concern is the age of the crust. While Site 847 sits in region whose tectonics is not well determined, the reconstruction of Hey (1977) calls for the age of the crust generated at either of these ridge crests to be approximately 9 Ma. The deepest samples recovered at Site 847 were, however, cherts with a calcareous veneer that contained abundant nannofossils of lower Miocene (approximately 22 Ma) age. The sediments immediately above the chert were approximately 6.5 Ma in age. While the lower Miocene material may be reworked, its presence in an area of crust thought to be about 9 Ma raises a number of questions about the tectonic history of this region. These questions are beyond the scope of shipboard analyses and will be the subject of future study. The presence of chert at a relatively shallow depth also implies higher than normal geothermal gradients. The proximity of the spreading centers and the Galapagos hot spot must thus be taken into account in reconstructing the geologic history of the sediments at Site 847. Given our uncertainty in the nature of the earliest history of the site, we will restrict our discussion of its geologic history to that period represented by the sediment overlying the chert–the last 6.5 m.y.

Four holes were drilled at the site. Holes B and C were both APC-cored to approximately 135 mbsf and then continued with the XCB coring system to 247 and 232 mbsf, respectively. Both holes were terminated when chert, an indication of increased temperature gradients, stopped penetration of the XCB. APC coring in conjunction with real-time monitoring of laboratory core logs (GRAPE, color, and susceptibility), assured that in the upper 135 m a continuous section was recovered. Double XCB coring of the lower part of the section allowed further assessment of the potential of XCB-cored material for high-resolution paleoceanographic studies and helped extend the section over which continuous recovery could be assured.

The drilled section represents what appears to be continuous sedimentation over the last 6.5 m.y. Sedimentation rates are, in general, high, being consistently over 30 m/m.y. and during the early Pliocene may be as high as 85 m/m.y. (Fig. 52A). The sediments are predominately nannofossil oozes with varying amounts of biogenic silica. A few intervals are dominantly calcareous nannofossil diatom ooze with higher proportions of clay.

To a first order, the properties of the sediments reflect the interplay between calcareous and biogenic silica deposition while to a second order, diagenesis also influences the section. Sediment density and color reflection show a very high degree of similarity (Fig. 52B, C); both of these properties representing changes in calcium carbonate content (Fig. 52D). The interval from 6.5 to 5 Ma is characterized by high sedimentation rates (approximately 30 m/m.y.–Fig. 52A) and high-frequency fluctuations in the proportions of nannofossils relative to diatoms; clay content is low and remains fairly constant throughout the interval. The relationship of these carbonate/silica cycles to variations in ocean chemistry (dissolution), changes in surface water conditions (productivity) and climatic forcing will be the subject of detailed shore-based study.

Based on long-term sedimentation and accumulation rate changes, it is possible to make a few general inferences. There are two prominent intervals of high diatom abundances within the section. The youngest at about 1.5–1.9 Ma is marked by a small increase in sedimentation rates and a marked decrease in color reflectance, sediment density, and calcium carbonate (Fig. 52). Mass accumulation rates show that the interval is a time of increased non-carbonate (assumed to be predominately biogenic silica), and organic carbon accumulation with a decrease in carbonate flux. We infer that this interval is a time of increased productivity and that the decrease in calcium carbonate may reflect enhanced dissolution due to increased organic carbon regeneration within the sediments.

The older interval of high diatom abundances, at about 4.5 Ma, is most clearly illustrated by a zone of negative magnetic susceptibility. This interval, however, is marked by an increased flux of all sedimentary components. This difference between these two intervals may reflect a number of different processes that will need further evaluation. For example, if the younger interval reflects increased production of opal and carbon that resulted into increased dissolution of calcium carbonate, then during the older interval the ratio of carbonate to organic carbon flux must have been sufficiently higher so that the increased production of organic carbon did not reduce an overall decrease in carbonate burial. Thus, the difference in these intervals may reflect changes in the biological communities producing the carbonate, opal, and organic carbonate as well as processes associated with dissolution of these components. Finally, the timing of this event seems to coincide with similar increases in sedimentation rates at

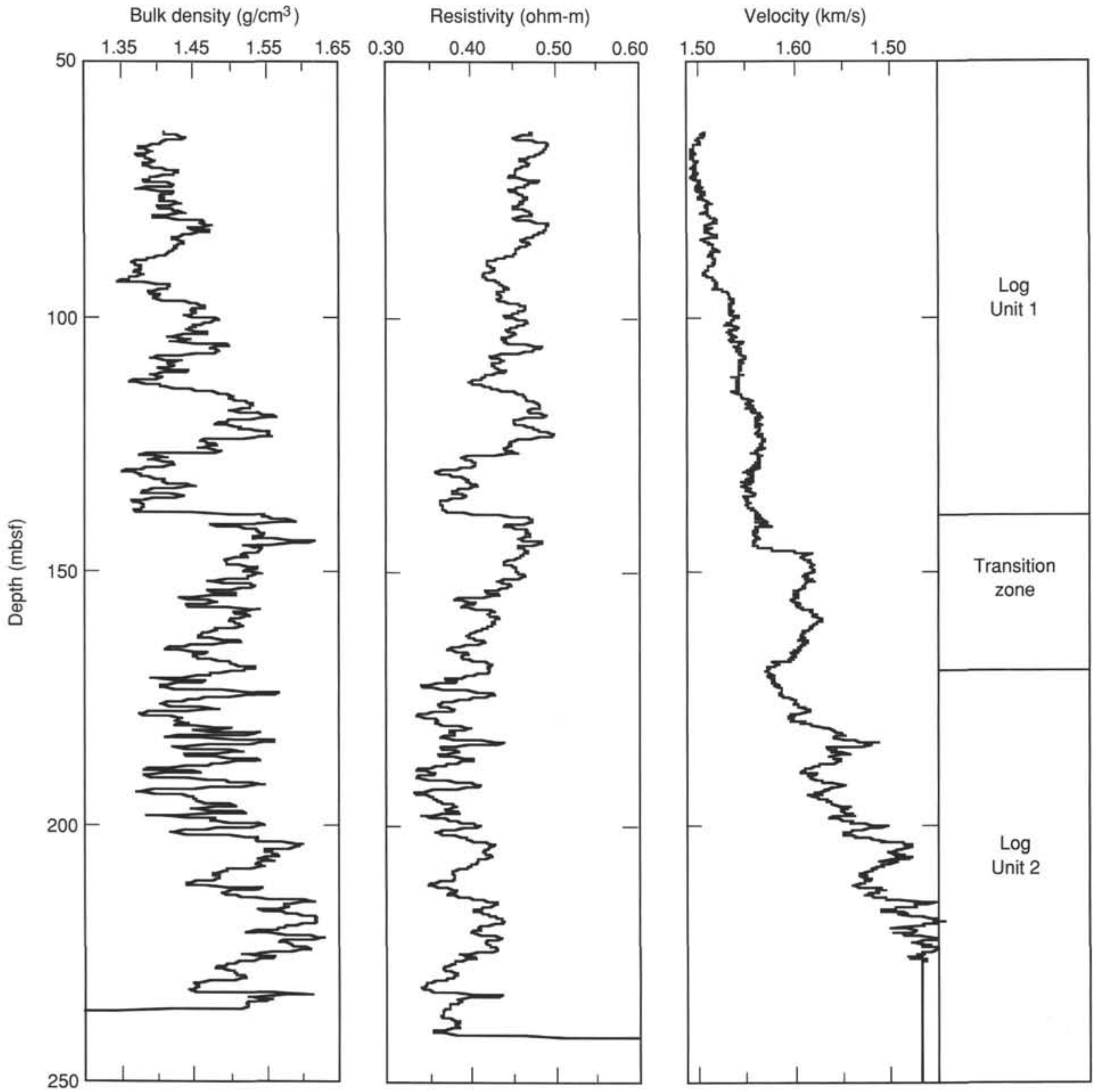

Figure 38. Plots of logging bulk density, intermediate resistivity, and long-spaced velocity vs. depth at Site 847. Boundaries of the log stratigraphic units are indicated.

other sites within the Pacific. The completion of the Leg 138 transects should provide significant new insights into the oceanographic processes associated with these intervals.

Superimposed on the paleoceanographic signal at Site 847 is geochemical evidence for fluid advection, particularly in the deeper part of the section. Interstitial water profiles of alkalinity, sulfate, and ammonia appear to be modified by upward advection as do the convex-upward profiles of sodium and chloride. The presence of fluid advection as well as the relatively high temperature gradients found at Site 847 (approximately 0.076° C/m) provide an explanation for the presence of chert at relatively shallow depths. The concentration of organic matter is low throughout the entire sequence except for the interval between 53 and 63 mbsf, in which C_{org} values reach around 1%. There is no apparent correlation between C_{org} and methane content in the sediments, suggesting that content of organic carbon may not be the limiting factor for microbial formation of methane.

One of the primary objectives of Leg 138 is the study of high-resolution climate change (time scales within the Milankovitch frequency bands requiring sampling intervals of at most 5 ky) during the late Neogene. While much of this effort will require significant shore-based laboratory work, one of the essential elements of these studies is a high-resolution chronostratigraphic framework. In the Pleistocene such a framework has been established by using the presence of orbitally related frequency components within the climate record (e.g., Imbrie, et al., 1985; Martinson et al., 1987). Mayer (1991) has shown that in the equatorial Pacific the near continuous GRAPE density record is a proxy for carbonate content and that, if carefully spliced, the GRAPE record can be used to provide an extremely detailed paleoceanographic record suitable for orbital tuning. We have extended this approach to all of the high-resolution real-time data acquisition systems used during Leg 138 (GRAPE, color reflectance, and magnetic susceptibility) and begun to evaluate the possibility of orbitally tuning through the late Neogene. The quality of the GRAPE density data in Site 847, and its high degree of correlation to Site 846, suggested that both very high-resolution stratigraphic correlations could be achieved with these data. This evaluation was

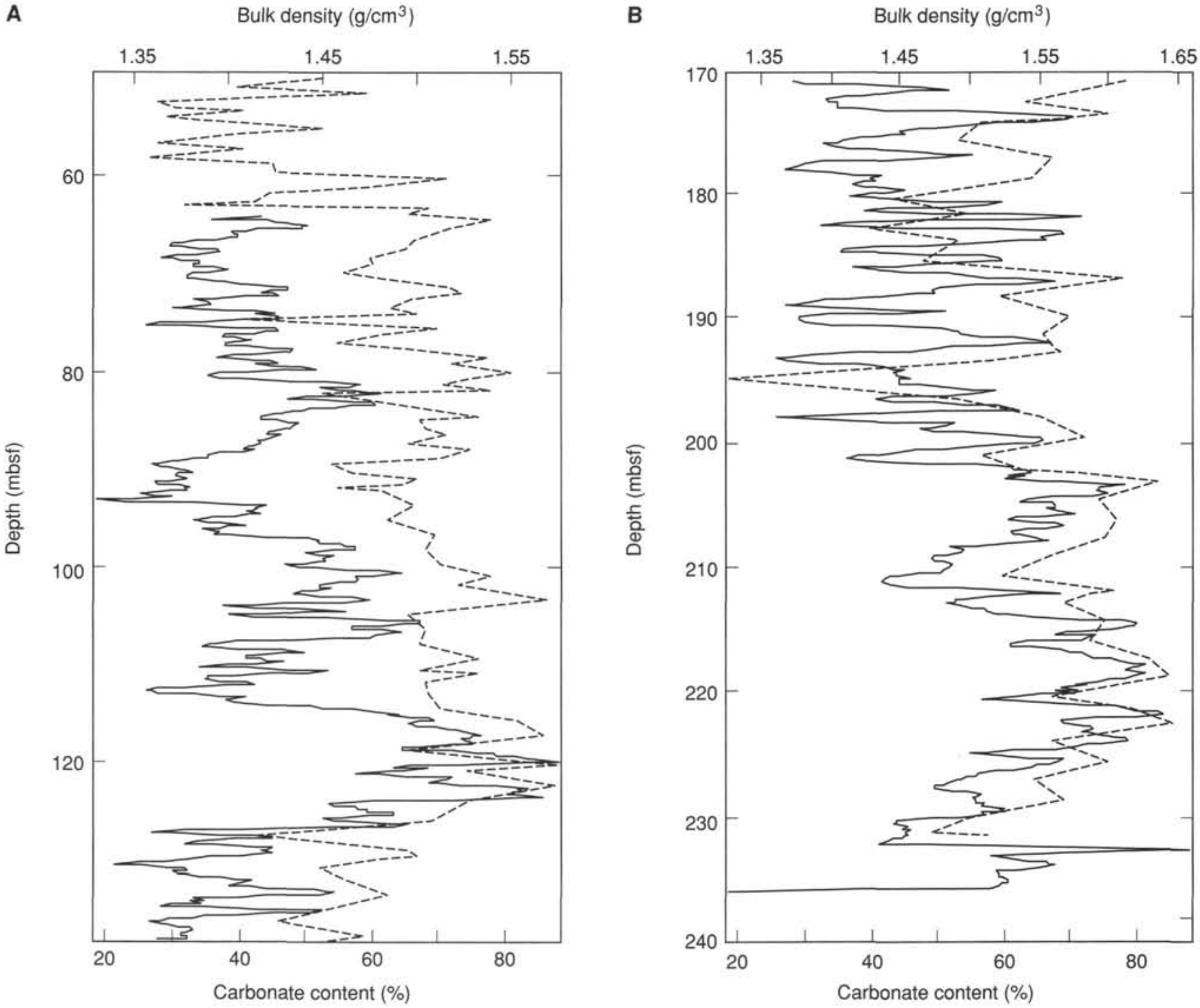

Figure 39. Log density (solid line) and carbonate content determined on core samples (dashed line) vs. depth in log Unit 1 (**A**) and in Unit 2 (**B**). Note the strong similarities between the two curves.

greatly aided by the composite sections which could be constructed from the overlapping cores as described in the "Sedimentation Rates" section (this chapter). The series used in these analyses were assembled by selecting the best data set from specific cores. By splicing these cores together a continuous GRAPE density record was constructed and the data, plotted on initial time scales seemed to reflect orbital forcing.

Initial orbital tuning was started for the time interval 2–5 Ma (Fig. 53). An evolutionary spectral plot shows how the variance within the GRAPE time series is distributed with respect to frequency and how this variance changes over the interval from 2 to 5 Ma (Fig. 54). Of particular interest is the change in the frequency bands associated with orbital tilt and precession. Over the entire interval the spectra are in general "red" with the highest concentration of variance in the low-frequency bands. Between 2 and 3 Ma there is concentration of variance in the 41,000-yr tilt band without a significant concentration in the precession band. Three million years ago marks the end of an interval where precessional frequencies are important in these records. Between 3 and 5 Ma. there is a concentration of variance at both the 23,000 and 19,000 frequency bands of precession (Fig. 53) as well as increased variance in the low frequencies. Thus, there is strong evidence for orbital response in these sediment records and that this response evolves through the late Neogene. More importantly this strongly suggests that the continuous section at Site 847 will provide an excellent paleoceanographic record of the equatorial Pacific.

REFERENCES

Claypool, G. E., and Kaplan, I. R., 1974. The origin and distribution of methane in marine sediments. *In* Kaplan, I. R. (Ed.), *Natural Gases in Marine Sediments.* Mar. Sci. 3:99–140.

Elderfield, H., and Gieskes, J. M., 1982. Sr isotopes in interstitial waters of marine sediments from Deep Sea Drilling Project cores. *Nature,* 333:493–497.

Gieskes, J. M., 1974. Chemistry of interstitial waters of marine sediments. *Annu. Rev. Earth Planet. Sci.,* 3:433–394.

Gieskes, J. M., Elderfield, H., and Palmer, M. R., 1986. Strontium and its isotopic composition in interstitial waters of marine carbonate sediments. *Earth Planet. Sci. Lett.,* 77:229–235.

Harrison, W. E., Hesse, R. , and Gieskes, J. M., 1982. Relationship between sedimentary facies and interstitial water chemistry of slope, trench, and Cocos Plate sites from the Middle America Trench transect, active margin off Guatemala, Deep Sea Drilling Project Leg 67. *In* Aubouin, J., von Huene, R., et al., *Init. Repts. DSDP,* 67: Washington (U.S. Govt. Printing Office), 603–613.

Hey, R., 1977. Tectonic evolution of the Cocos-Nazca spreading center. *Geol. Soc. Am. Bull.,* 88:1404–1420.

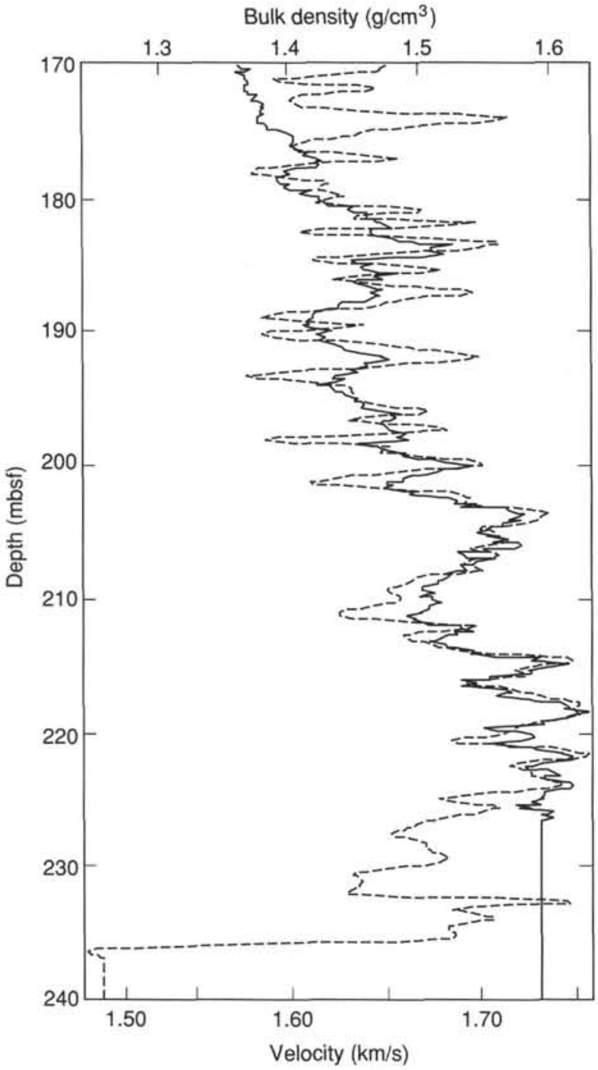

Figure 40. Log density (dashed line) and velocity (solid line) values vs. depth in log Unit 2. Note the good correlation between the two properties.

Hey, R., Johnson, L., and Lowrie, A., 1977. Recent plate motions in the Galapagos area. *Geol. Soc. Am. Bull.*, 88:1385–1403.

Imbrie, J., Hays, J., Martinson, D. G., McIntyre, A., Mix, A. C., Morley, J. J., Pisias, N. G., Prell, W. L., and Shackleton, N. J., 1984. The orbital theory of Pleistocene climate: support from a revised chronology of the marine ^{18}O record. *In* Berger, A., Imbrie, J., Hays, J., Kukla, G., Saltzman, B. (Eds.), *Milankovitch and Climate (Pt. 1):* Dordrecht, The Netherlands (D. Reidel), 269–305.

Johnson, G. R., and Olhoeft, G. R., 1984. Density of rocks and minerals. *In* Carmichael, R. S. (Ed.) *CRC Handbook of physical properties of rocks,* Vol. III: Boca Raton, FL (CRC Press), 1–38.

Lyle, M., 1983. The brown-green color transition in marine sediments a marker of the Fe(III)-Fe(II) redox boundary. *Limnol. Oceanogr.*, 28(5):1026–1033.

Martinson, D. G., Menke, W., and Stoffa, P., 1982. An inverse approach to signal correlation. *J. Geophy. Res.*, 87:4807–4818.

Martinson, D. G., Pisias, N. G., Hays, J. D., Imbrie, J., Moore, T. C., Jr., Shackleton, N. J., 1987. Age dating and the orbital theory of the ice ages: development of a high-resolution 0 to 300,000-year chronostratigraphy. *Quat. Res.*, 27:1–29.

Mayer, L. A., 1979. The origin of fine-scale acoustic stratigraphy in deep-sea carbonates. *J. Geophys. Res.*, 804:6177–6184.

Mayer, L. A., Shipley, T. H., Theyer, F., Wilkens, R. W., and Winterer, E. L., 1985. Seismic modeling and paleoceanography at DSDP Site 574. *In* Mayer, L. A., Theyer, F., Thomas, E., et al., *Init. Repts. DSDP,* 85: Washington (U.S. Govt. Printing Office), 947–970.

———, 1991. Extraction of high-resolution carbonate data for paleoclimatic reconstruction. *Nature,* 352:148–151.

Mayer, F., Vincent, E., and Mayer, L. A., 1989. Sedimentation and paleoceanography of the central equatorial Pacific. *In* Winterer, E. L., Hussong, D. M., and Decker, R. (Eds), *The Geology of North America: The Eastern Pacific Ocean and Hawaii.* Geol. Soc. Am., 347–372.

Okada, H., and Bukry, D., 1980. Supplementary modification and introduction of code numbers to the low-latitude coccolith biostratigrafic zonation (Bukry, 1973; 1975). *Mar. Micropaleontol.*, 5:321–325.

Martini, E., 1971. Standard Tertiary and Quaternary calcareous nannoplankton zonation. *Proc. 2nd Conf. Planktonic Microfossils, Roma 1970:* Rome (Ed. Tecnoscienza), 739–785.

Rio, D., Backman, J. and, Raffi, I. (in press). Calcareous nannofossil biochronology and the Pliocene-Pleistocene boundary. *In* Van Couvering (Ed.), *Final Repts. IGCP, Project 41.*

Schlumberger, 1989. *Log interpretation Principles/Applications:* Houston (Schlumberger Educational Services).

Ms 138A-112

NOTE: For all sites drilled, core description forms ("barrel sheets") and core photographs have been reproduced on coated paper and can be found in Section 4, beginning on page 397. Forms containing smear-slide data can be found in Section 5, beginning on page 663.

Formation microscanner images for this site are presented on microfiche in the back of Part 2.

Table 19. Means and standard deviations of physical property and geochemical measurements in each log stratigraphic unit and the transition zone.

	Unit 1		Transition zone		Unit 2	
Depth (mbsf)	Mean	Standard deviation	Mean	Standard deviation	Mean	Standard deviation
Depth of unit (mbsf)	53–138		138–171		171–~250	
Far velocity (km/s)	1.54	0.023	1.62	0.03	1.67	0.044
Near velocity (km/s)	1.53	0.023	1.58	0.022	1.66	0.048
Density (g/cm^3)	1.43	0.049	1.5	0.044	1.5	0.072
Gamma-ray (API units)	6.1	1.59	5.5	1.04	6.08	1.18
Intermediate resistivity (ohm-m)	0.443	0.032	0.429	0.029	0.384	0.027
Shallow resistivity (ohm-m)	0.427	0.038	0.428	0.048	0.386	0.047
Calcium yield (x 10^3)	64.5	27.7	86.8	25.0	74.0	27.0
Silica yield (x10^3)	8.2	18.0	0.35	16.0	13.7	16.0
Log density-Lab (PP) density	0.07	0.055	0.051	0.07	0.073	0.07
Log density–GRAPE density	-0.04	0.05	-0.03	0.07	-0.007	0.07

Table 20. Measured values of specific properties within the two chert layers near the base of Hole 847B.

Parameter	Depth (mbsf)	Value
Shallow resistivity	231.5 U	3.24 ohm-m
	239.9 U	0.96 ohm-m
	240.8 L	9677 ohm-m
Intermediate resistivity	232.9 U	0.43 ohm-m
	242.4 L	1.49 ohm-m
Bulk density	232.6 U	1.66 g/cm^3
Calculated porosity		50.3%

Note: "U" indicates that the value was measured in the shallow (upper) chert; "L" refers to the deeper chert layer. Porosity was calculated using an average grain density of 2.3 for cristobalite (Johnson and Olhoeft, 1984) and the density log.

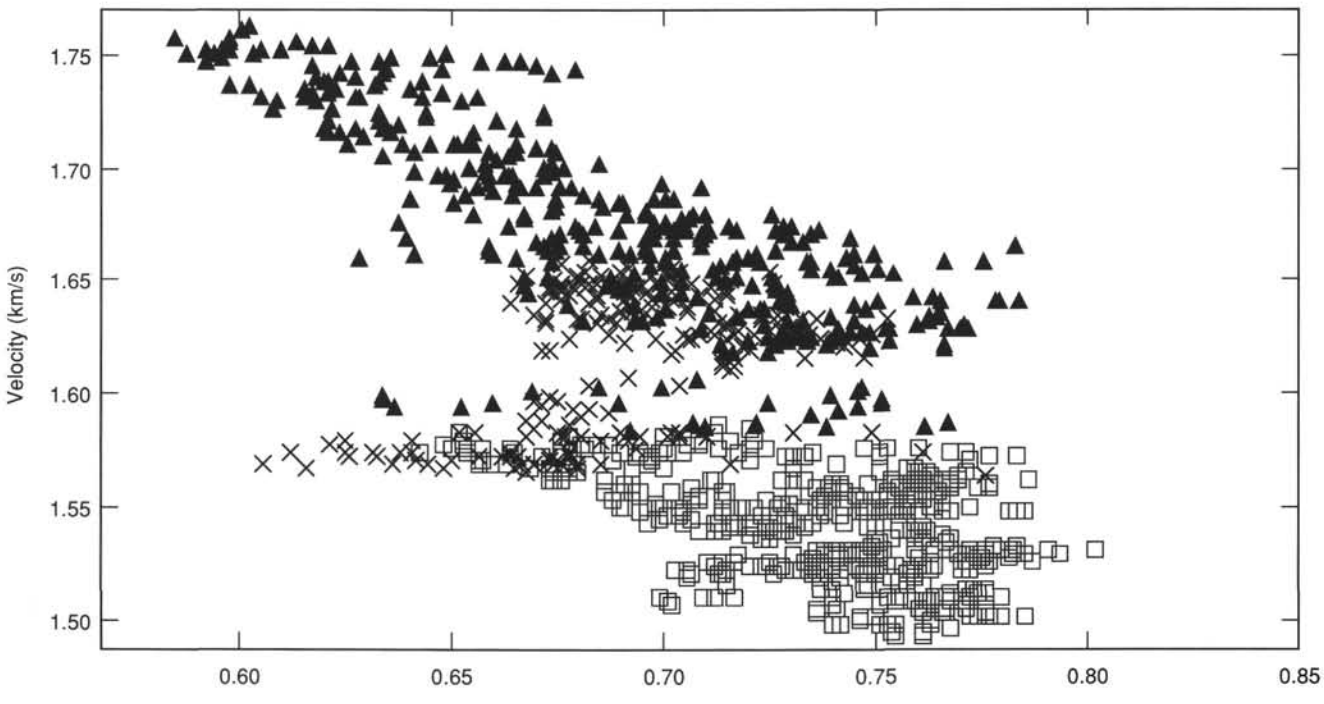

Figure 41. Velocity vs. porosity at Site 847. Log Unit 1, open squares; log Unit 2, solid triangles; transition zone, crosses. Note the presence of a distinct gap in velocity values at approximately 1.61 km/s. This gap corresponds to the abrupt increase observed in velocity measurements and marks the onset of lithification.

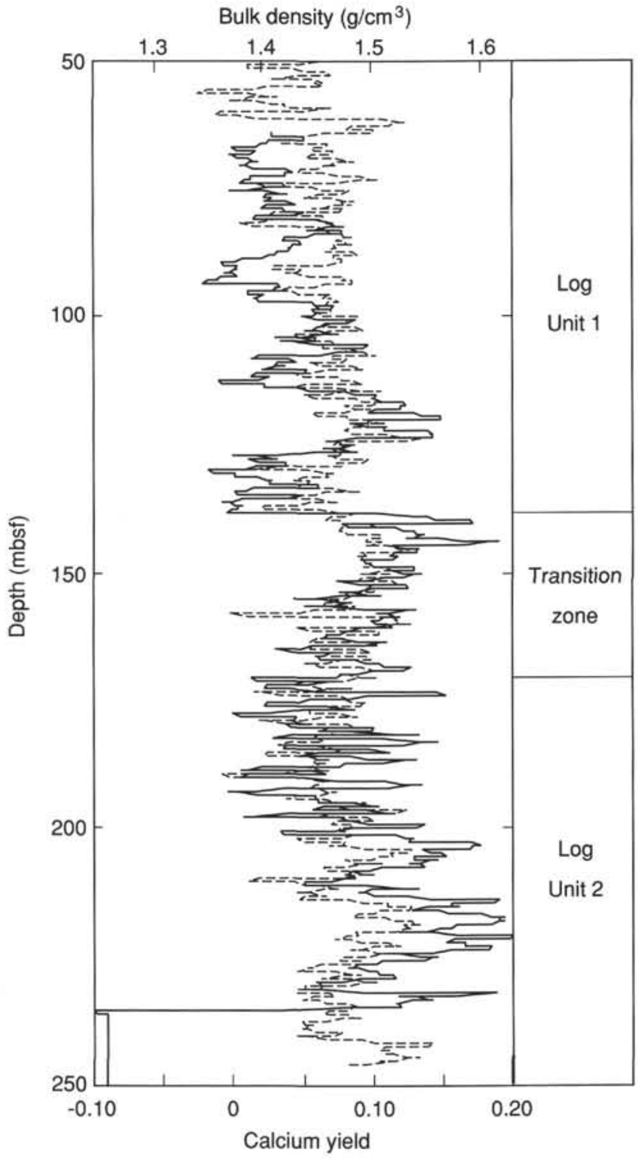

Figure 42. Log density (solid line) and calcium yield (dashed line) measurements vs. depth at Site 847. Similarities between trends in the two properties is further evidence of the influence of carbonate content on density in these deposits.

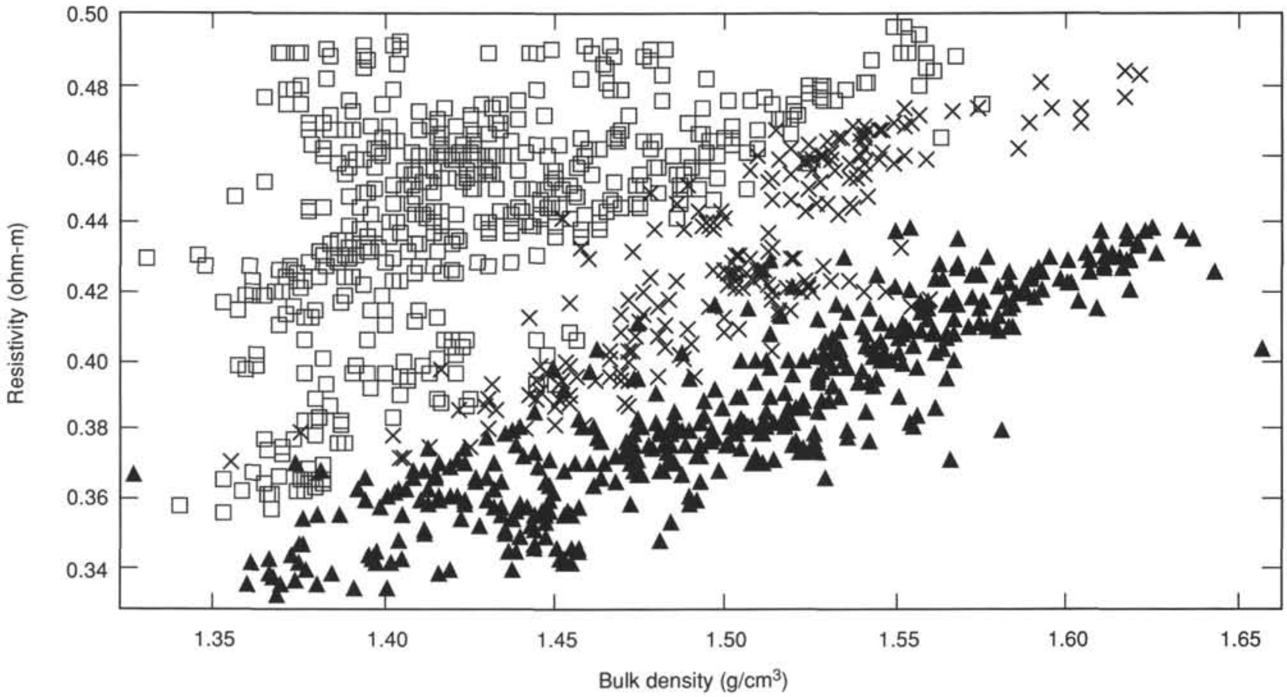

Figure 43. Resistivity vs. bulk density at Site 847. Symbols are as in Figure 41. Although the range of density values at Site 847 resembles that observed at other Leg 138 sites, resistivity values are extremely low and tend to decrease with depth.

Table 21. Summary of traveltimes, depths, and ages for Site 847 reflectors.

Reflector	Traveltime (s)	Synthetic depth (m)	Depth (mbsf)	Depth (mcd)	Age (Ma)
R1	0.015	11.20	10.50	10.60	0.33
	0.018	13.40	12.00	12.10	0.38
R2	0.032	23.90	23.00	23.35	0.70
	0.039	29.20	26.00	28.80	0.85
R3A	0.085	64.00	62.00	68.75	1.86
	0.088	66.30	84.00	94.20	2.65
R3B	0.091	68.40			
	0.097	73.00			
R3C	0.100	75.30			
	0.104	78.30			
R3D	0.106	79.90			
	0.111	83.60			
R5	0.150	113.70	112.00	126.00	3.69
	0.154	116.80	116.50	130.50	3.88
R7	0.171	130.20	130.00	145.50	4.40
	0.178	135.60	134.50	150.45	4.46
R8	0.186	141.90	141.00	157.40	4.54
	0.190	145.00	145.00	161.45	4.59
R9	0.198	150.90	150.50	169.90	4.69
	0.203	155.50	156.00	175.35	4.75
R11	0.220	169.40	168.00	187.35	4.89
	0.223	171.80	171.00	190.35	4.93
R12	0.226	174.10	173.50	192.85	4.96
	0.229	176.50	176.00	195.35	5.00
R14	0.248	192.20	192.00	211.35	5.47
	0.252	195.50	196.00	215.35	5.58
R15	0.254	197.20	197.50	216.85	5.63
	0.262	203.90	203.50	222.85	5.80
Chert	0.313	247.00	247.00	266.35	6.30
	0.318				

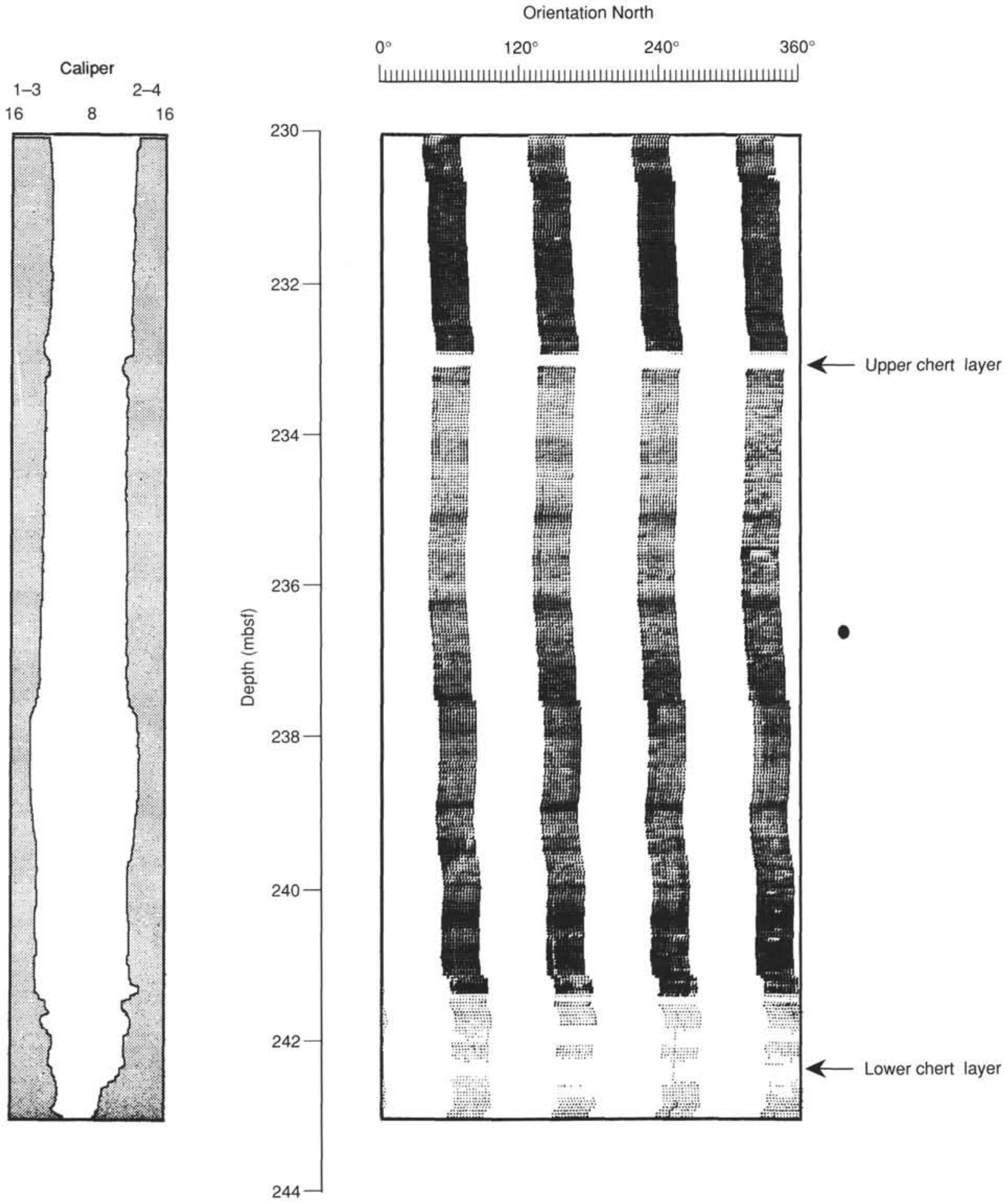

Figure 44. FMS image (right) and caliper log (left) from 230 to 243 mbsf in Hole 847B. The locations of the two chert layers are marked. On caliper log the left curve represents the distance between pads 1 and 3; the right curve is the distance between pads 2 and 4.

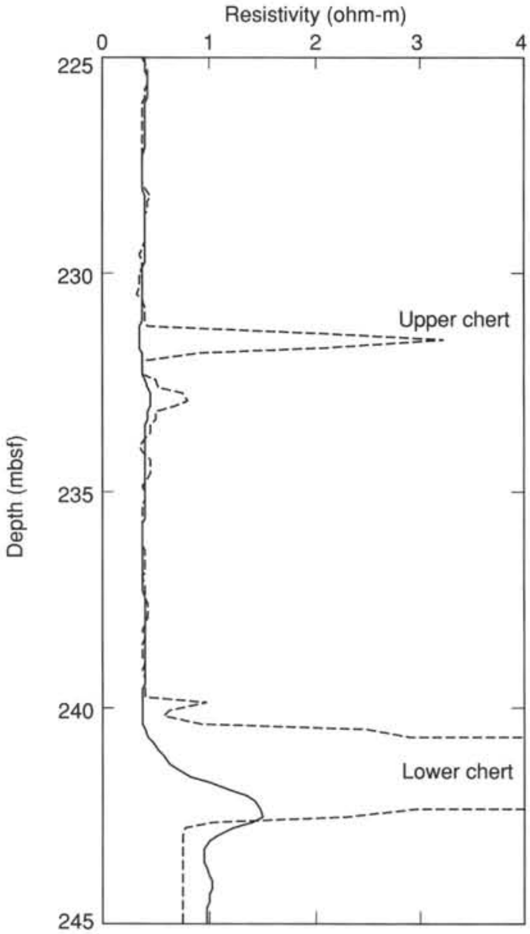

Figure 45. Intermediate (solid line) and shallow-focused (dashed line) resistivity measurements near the base of Hole 847B. The presence of both vertical and lateral heterogeneity in the two chert layers is suggested.

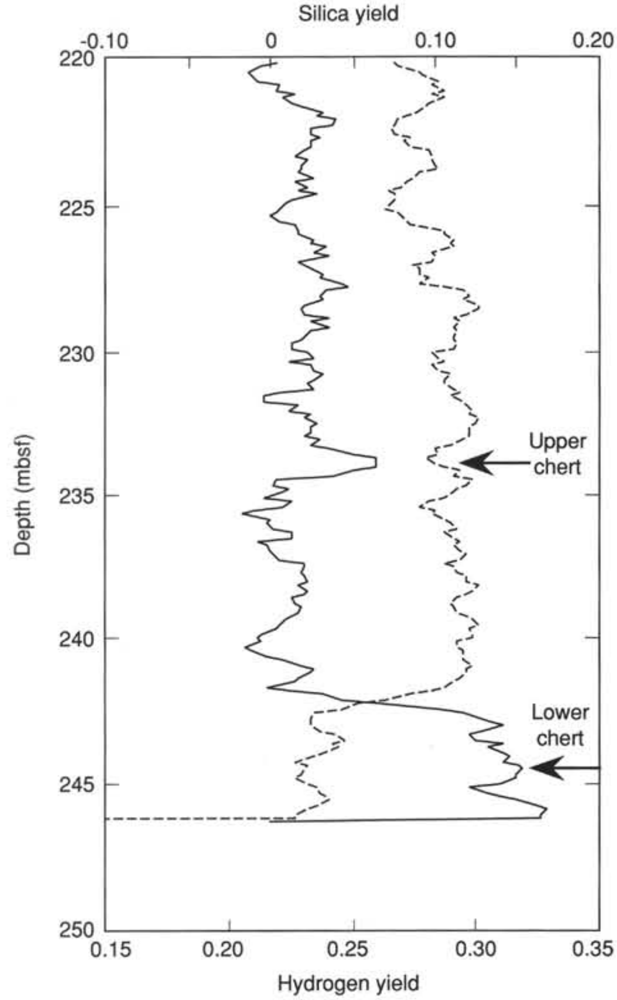

Figure 46. Silica yield (solid line) and hydrogen yield (dashed line) logs near the bottom of Hole 847B. High silica concentrations and low hydrogen/water contents characterize the chert beds.

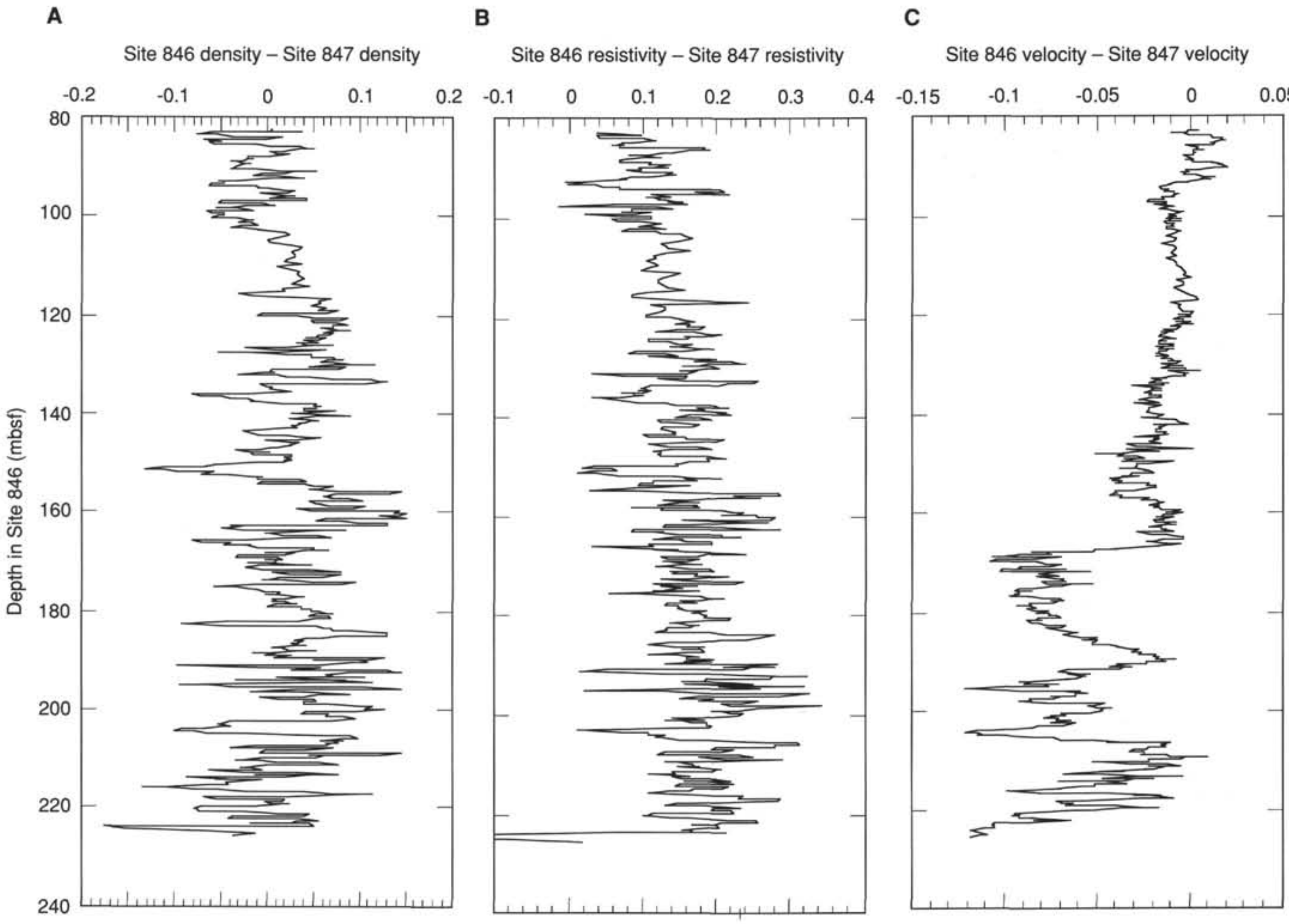

Figure 47. Plots of the differences between log measurements at Sites 846 and 847. **A.** Bulk density. **B.** Intermediate resistivity. **C.** Velocity.

Table 22. Backtracked path for Site 847.

Age (Ma)	Latitude (°S)	Longitude (°W)
1	0.24	96.01
2	0.28	96.72
3	0.32	97.43
4	0.36	98.14
5	0.41	98.85
6	0.46	99.56
7	0.52	100.27

Note: Pole of rotation = 0–12 Ma, 71.5°N, 86.8°W. Angular velocity - –0.75°/m.y.

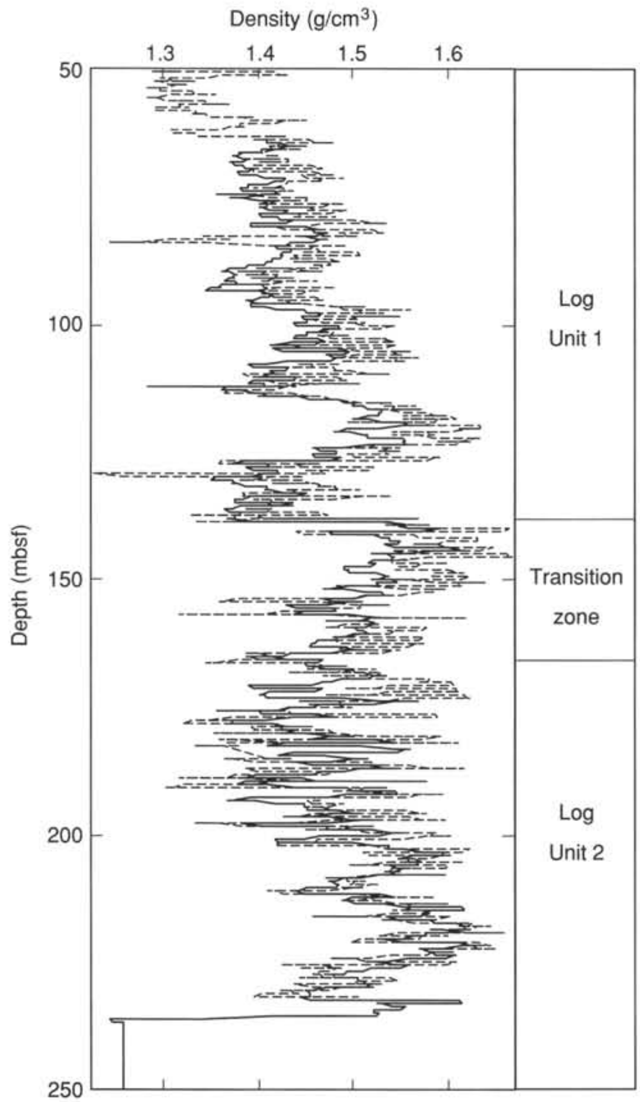

Figure 48. Comparison of density values obtained by logging (solid line) and GRAPE (dashed line) measurements; GRAPE densities were smoothed using a three-point gaussian smoothing routine.

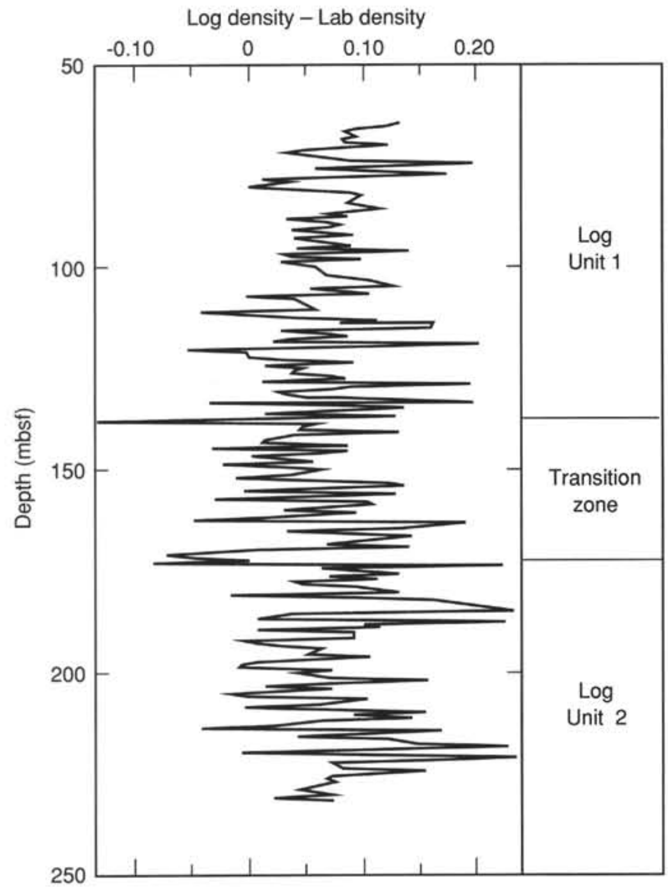

Figure 49. Plot of the difference between log bulk densities and density values determined gravimetrically on core samples.

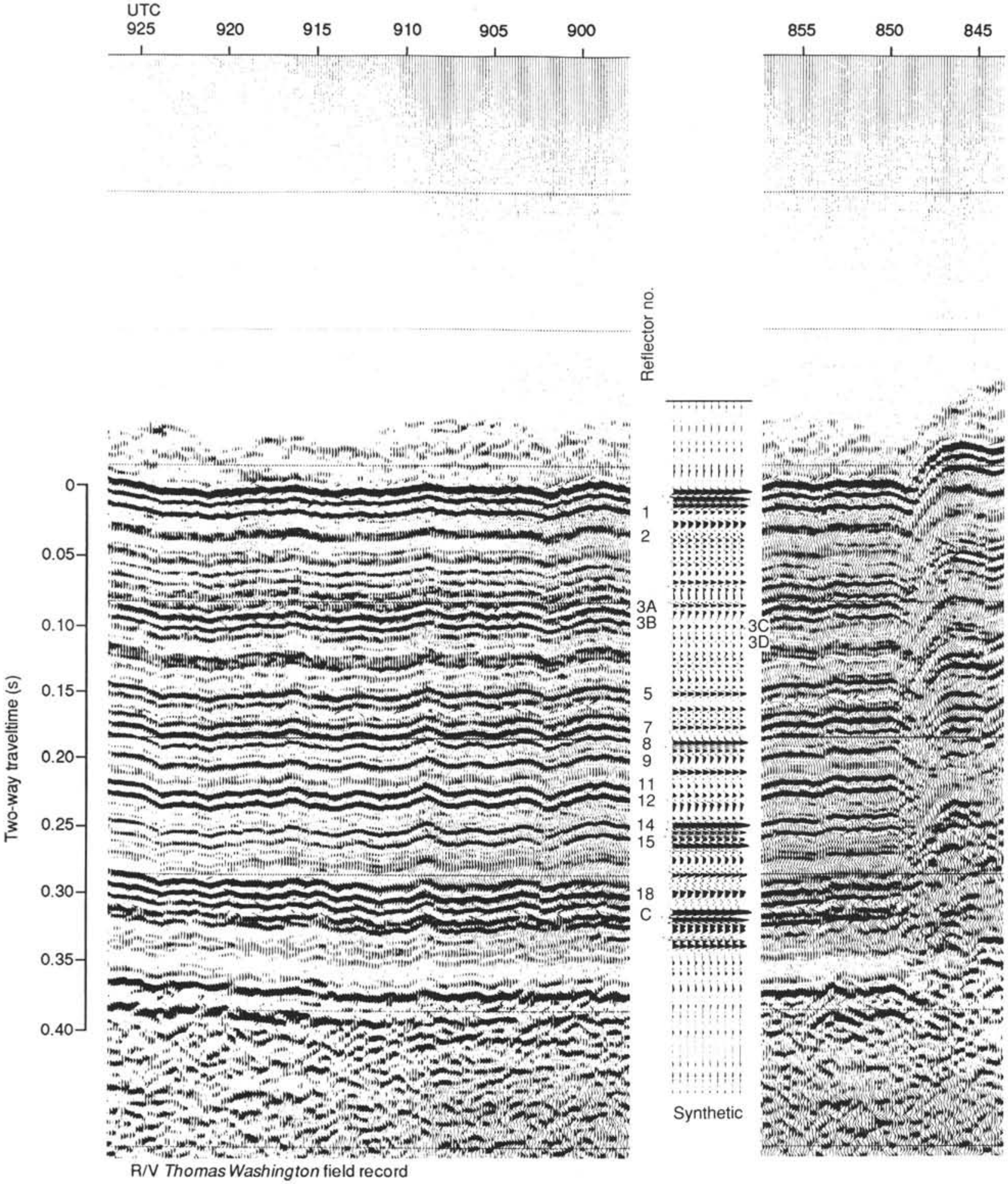

Figure 50. Comparison of synthetic seismogram and field record, Site 847.

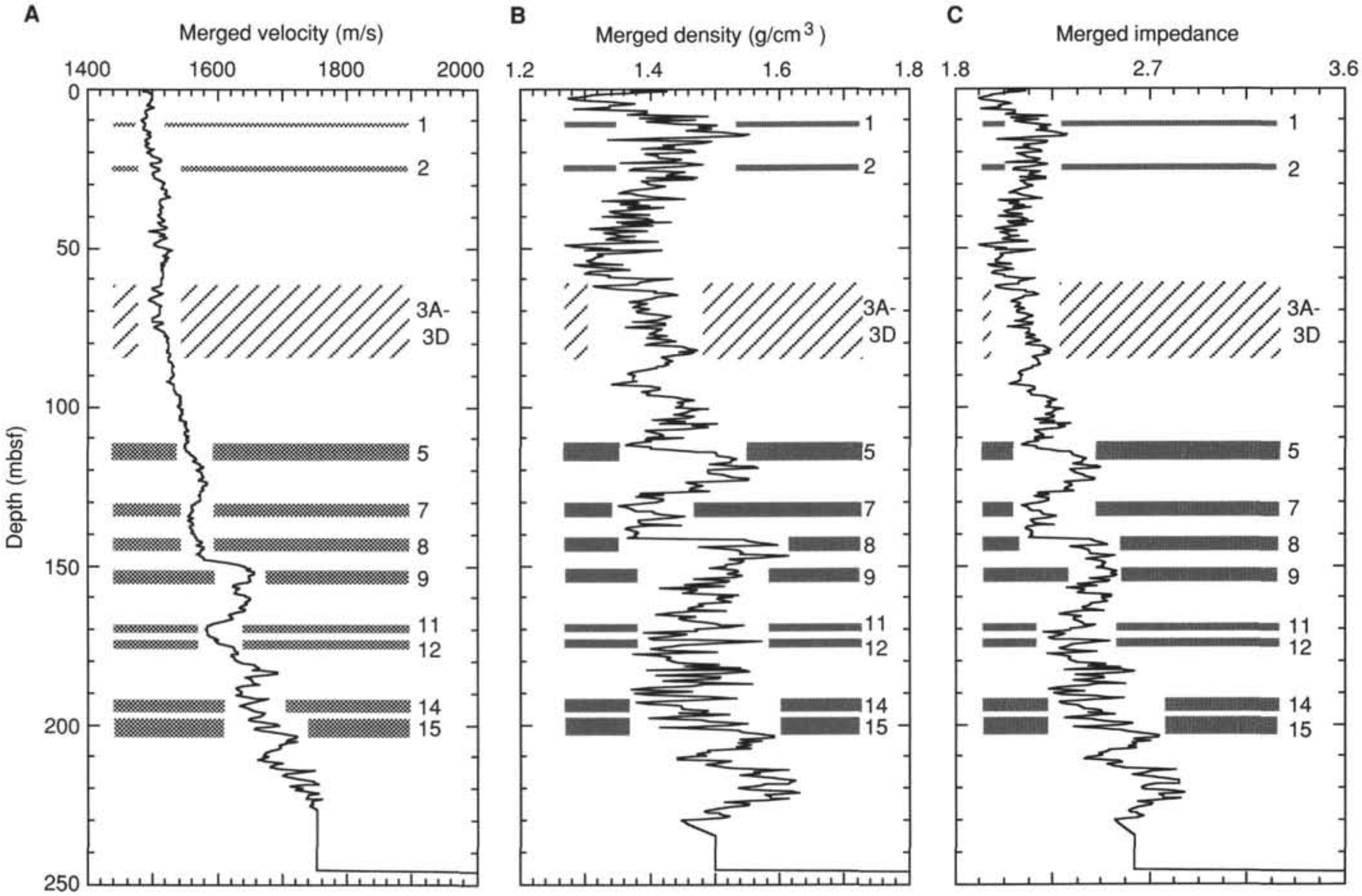

Figure 51. Data used for generating Site 847 synthetic seismograms. The 11 reflectors picked from the synthetic seismogram are shown for comparison. **A.** Velocity. **B.** Density. **C.** Acoustic impedance.

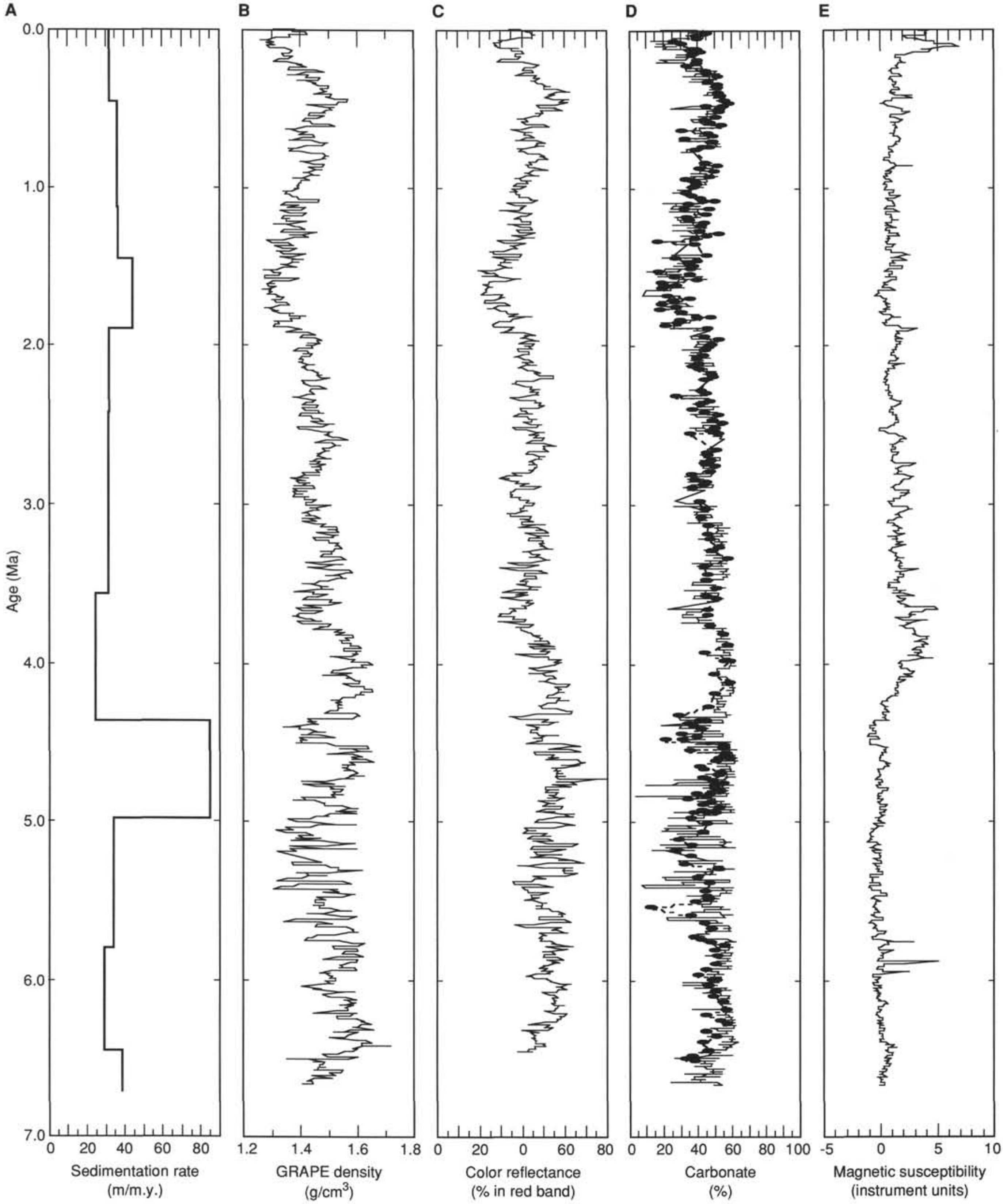

Figure 52. Sedimentation rate vs. sediment age (**A**); sediment density, based on composite of all holes vs. age (**B**); color reflectance in the red band, based on composite of all holes vs. age (**C**); predicted carbonate (based on sediment density, etc.) and measured carbonate (dots) (Hole 847B) vs. age (**D**); sediment magnetic susceptibility based on composite of all holes vs. age, (**E**).

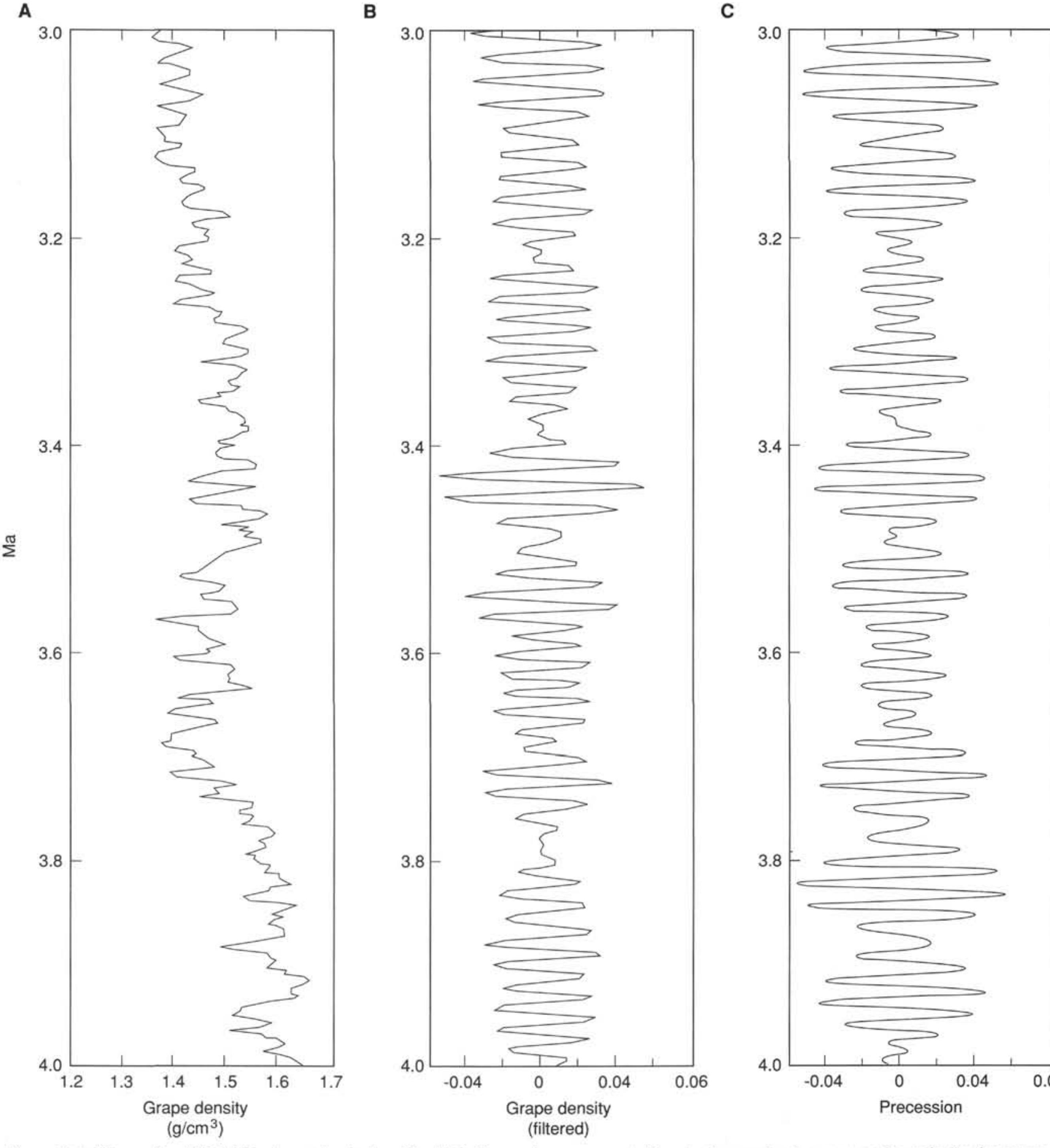

Figure 53. **A.** Time series of GRAPE sediment density from 3 to 4 Ma. Time series was generated by selecting overlapping cores used to make the site composite (see "Sedimentation Rates" section, this chapter) and then tuning time series to orbital precession. **B.** Bandpass-filtered GRAPE time series using a filter centered at the precession frequency. **C.** Orbital precession using the new astronomic calculations of Berger (pers. comm., 1991).

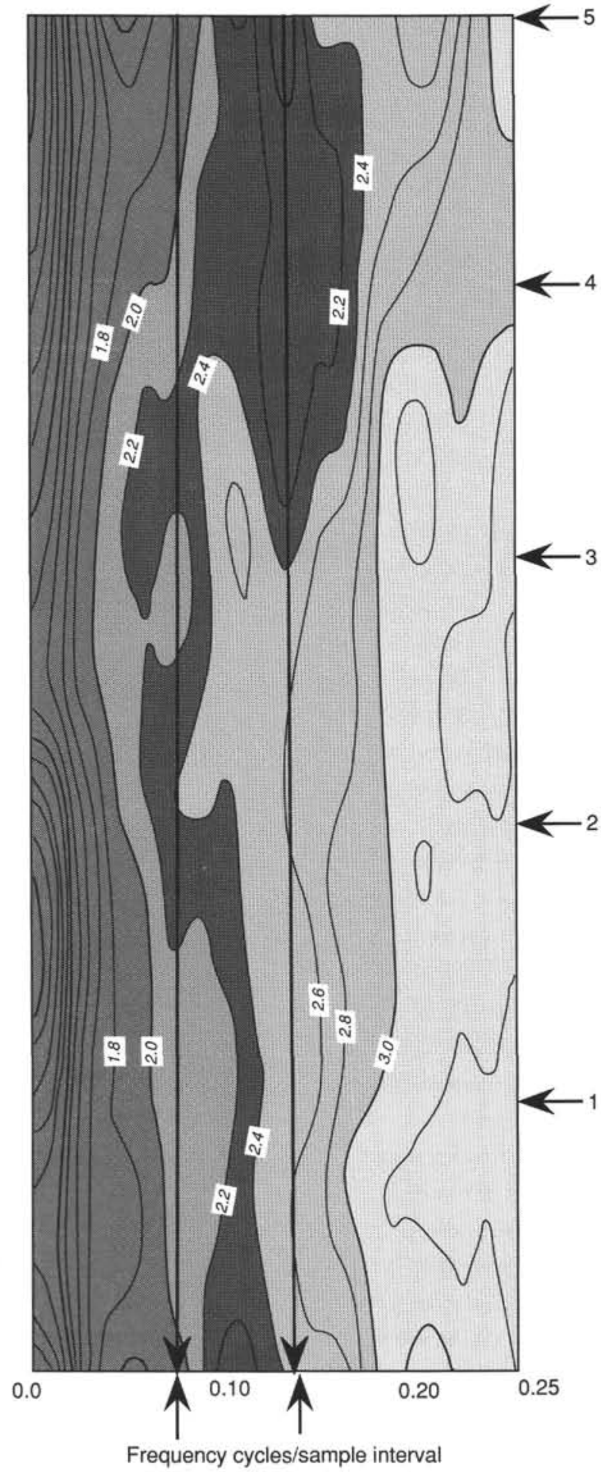

Figure 54. Evolutionary spectra for GRAPE data from 2 to 5 Ma. Spectra are calculated over a 555 k.y. interval with a sampling interval of 3 k.y. The time series for each spectra overlap the next series by 250 k.y. The contours are –1 times the log of the spectral density. Numbers on the right of the spectra mark the end of a particular spectrum in Ma. Vertical lines drawn with meeting arrows on the frequency axis mark the 41,000-yr period (0.07 cycles per sample interval) and the 23,000 year period (0.13 cycles per sample interval) of the tilt and precession cycles of the earth's orbit.

Hole 847B: Resistivity-Sonic-Natural Gamma Ray Log Summary

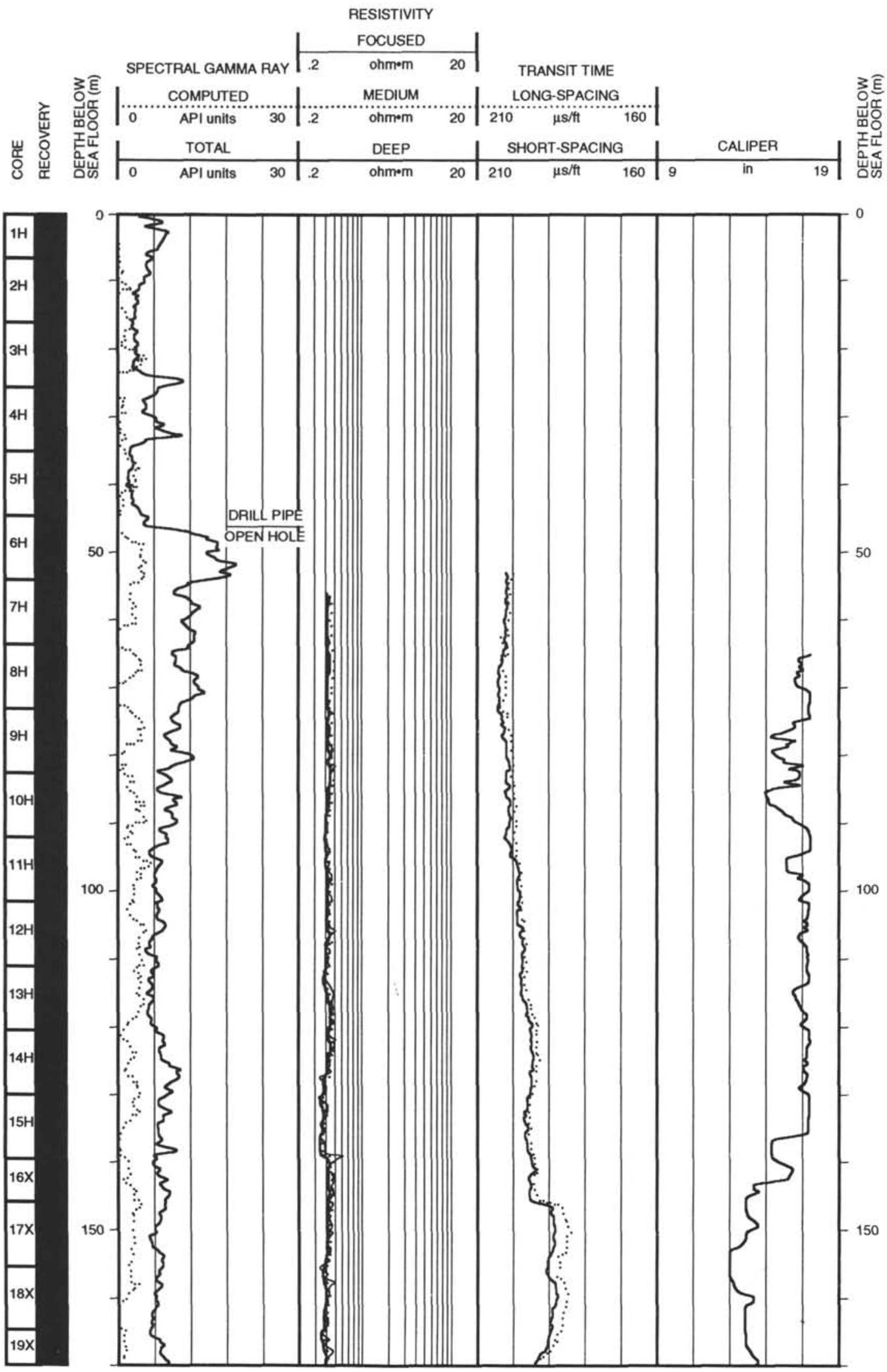

Hole 847B: Resistivity-Sonic-Natural Gamma Ray Log Summary (continued)

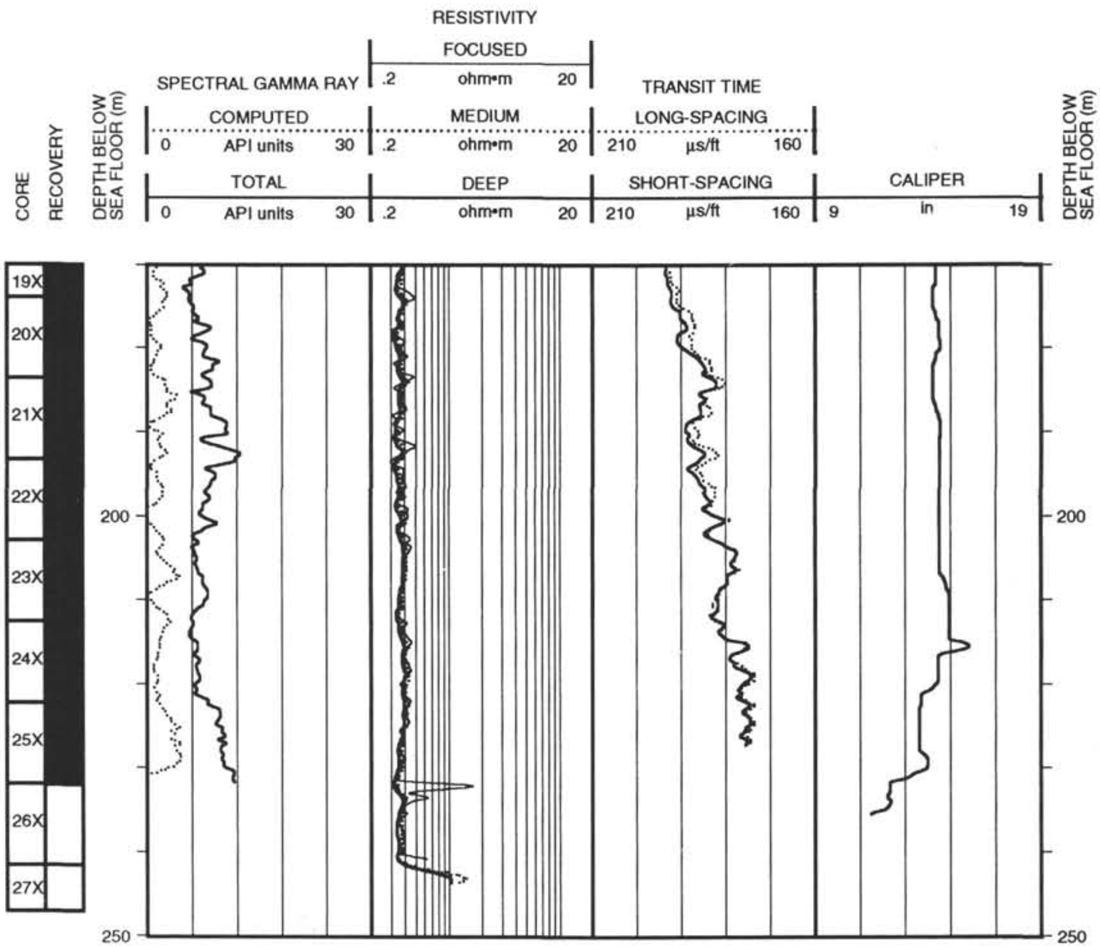

Hole 847B: Density-Natural Gamma Ray Log Summary

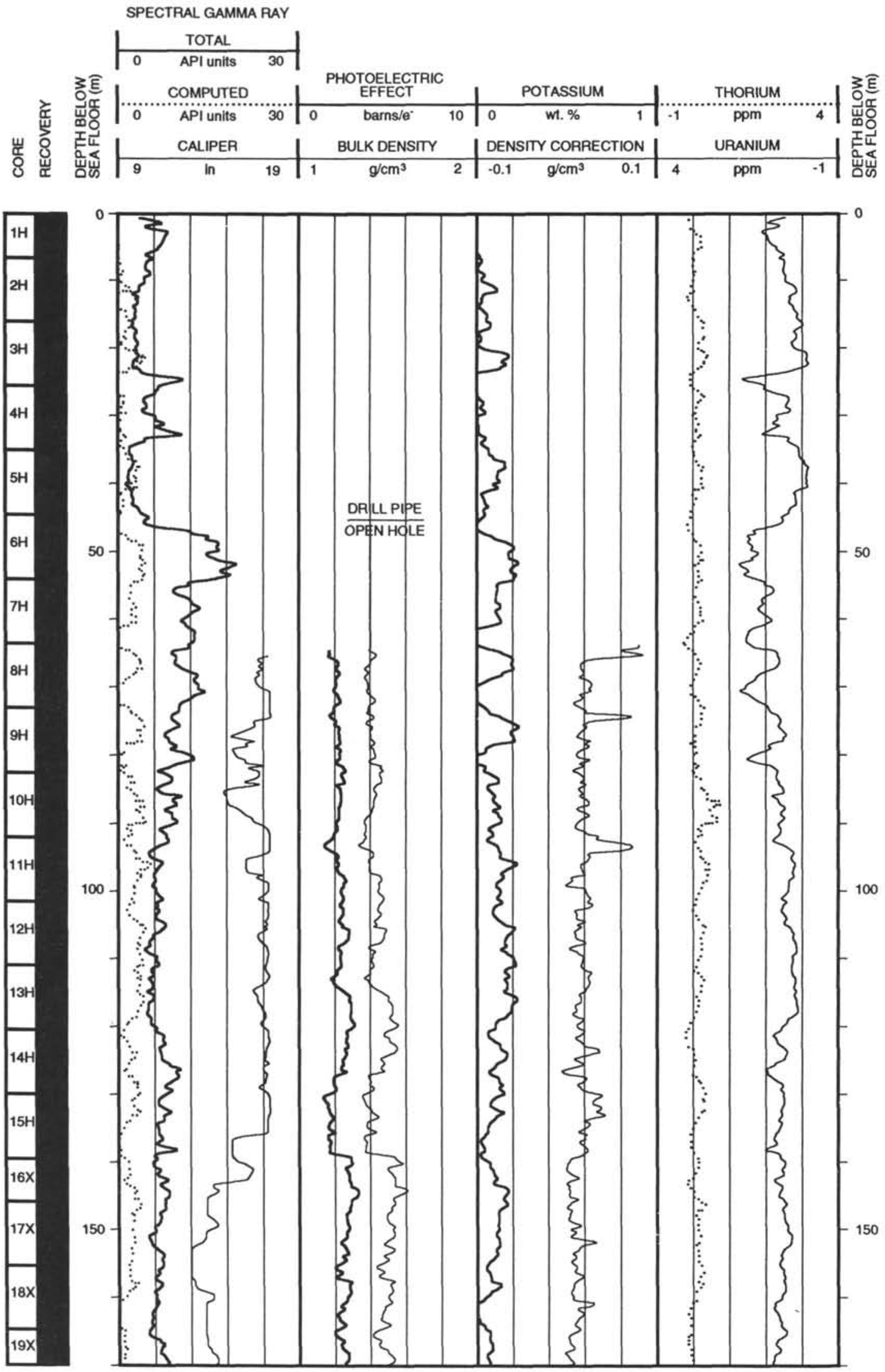

Hole 847B: Density-Natural Gamma Ray Log Summary (continued)

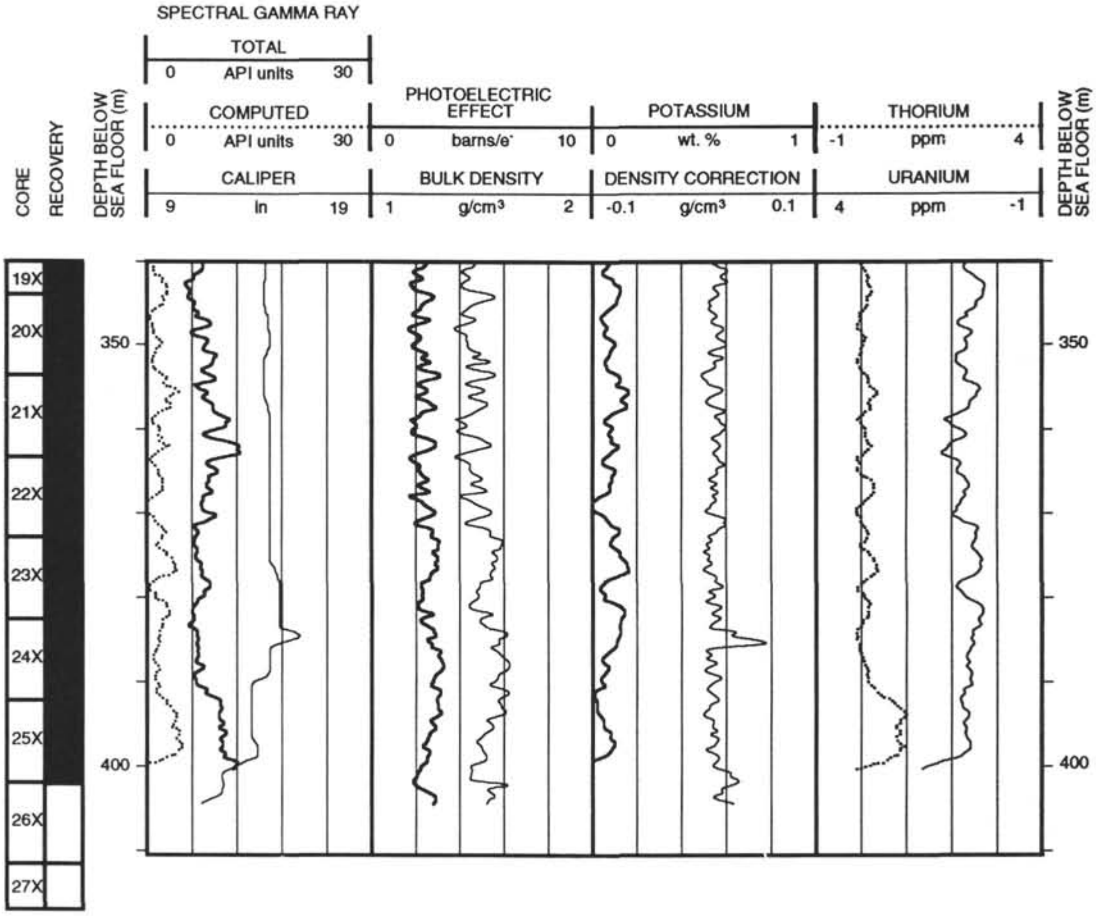

Hole 847B: Geochemical Log Summary

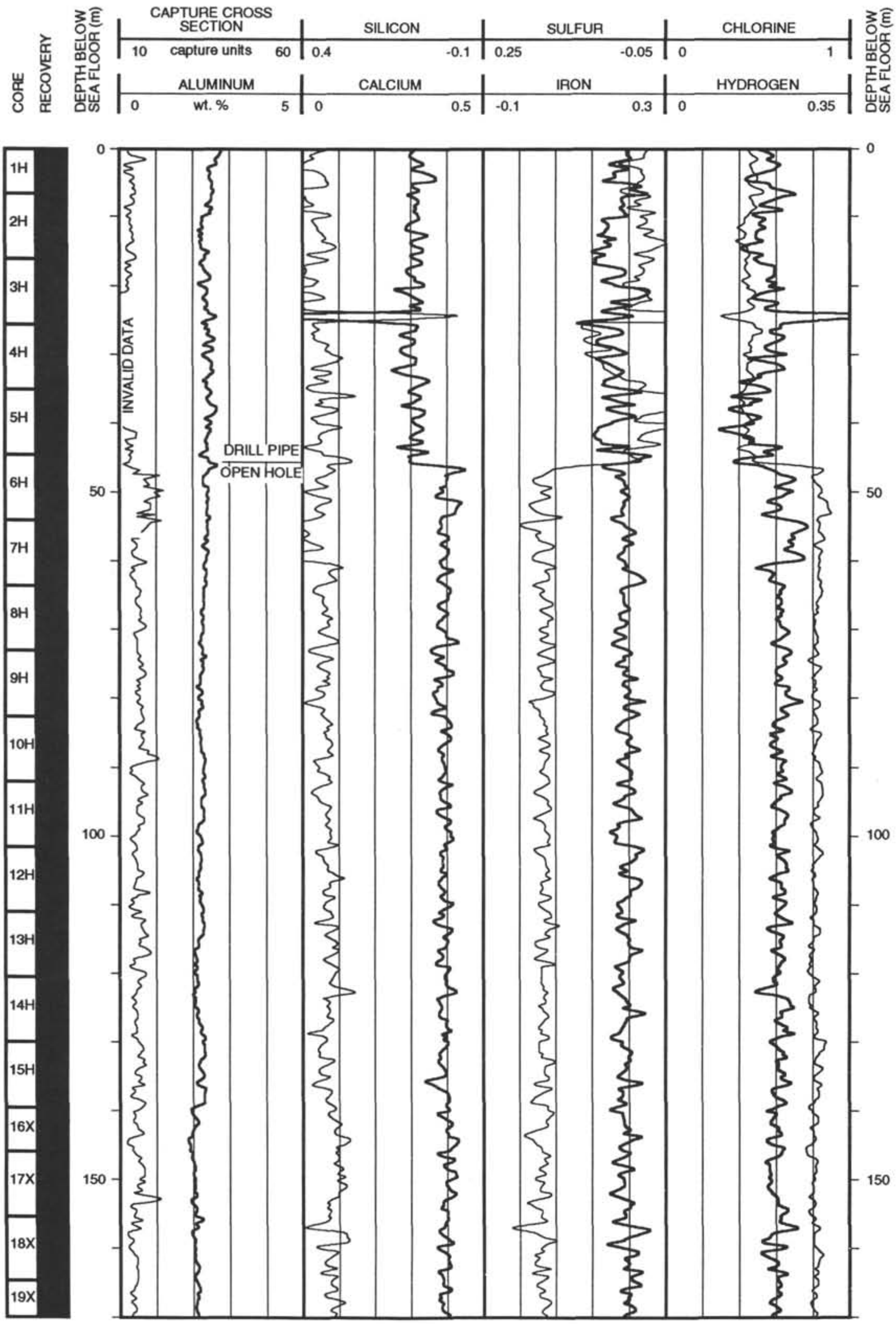

Hole 847B: Geochemical Log Summary (continued)